



Theses and Dissertations

2022-08-09

Distribution and Transportation of Sand and Potential Sand Source Materials on Titan: Implications for the Geologic History

Benjamin Dean Lake
Brigham Young University

Follow this and additional works at: <https://scholarsarchive.byu.edu/etd>



Part of the [Physical Sciences and Mathematics Commons](#)

BYU ScholarsArchive Citation

Lake, Benjamin Dean, "Distribution and Transportation of Sand and Potential Sand Source Materials on Titan: Implications for the Geologic History" (2022). *Theses and Dissertations*. 9659.
<https://scholarsarchive.byu.edu/etd/9659>

This Thesis is brought to you for free and open access by BYU ScholarsArchive. It has been accepted for inclusion in Theses and Dissertations by an authorized administrator of BYU ScholarsArchive. For more information, please contact ellen_amatangelo@byu.edu.

Distribution and Transportation of Sand and Potential Sand Source Materials on Titan:
Implications for the Geologic History

Benjamin Dean Lake

A thesis submitted to the faculty of
Brigham Young University
in partial fulfillment of the requirements for the degree of
Master of Science

Jani Radebaugh, Chair
Eric H. Christiansen
Sam Hudson

Department of Geological Sciences
Brigham Young University

Copyright © 2022 Benjamin Dean Lake
All Rights Reserved

ABSTRACT

Distribution and Transportation of Sand and Potential Sand Source Materials on Titan: Implications for the Geologic History

Benjamin Dean Lake
Department of Geological Sciences, BYU
Master of Science

Titan is an important planetary body for aeolian research because of the vast equatorial sand seas that span 20% of its surface. Previous studies have determined the general margins of sand and sand seas on Titan, and have speculated about the source of Titan's sand. Little research has been done concerning where sand collects in the sand seas. Additionally, the relationships between material distributions as observed by the Cassini Visual and Infrared Mapping Spectrometer (VIMS) and the history of erosion and transportation of sediments across equatorial latitudes is not fully understood. This work focuses on an in depth evaluation of sand distribution and abundance across the sand seas, and presents evidence for an alternative sand source. This work also addresses a potential stratigraphy for the equatorial regions based on the excavation of materials from impact craters.

We mapped the extent of relative sand abundances by comparing different Cassini image datasets, largely by mapping where the Imaging Science Subsystems (ISS) regions were darkest, indicating the presence of more sand. Our results revealed that greater abundances of sand accumulate near the eastern margins of sand seas. This is in agreement with previous studies that demonstrated general W to E transport, and fits a general model of sand transport across the sand seas to collect at the downwind margins, perhaps ahead of topographic obstacles that mark the eastern ends of the sand seas. Additionally, we found that the largest continuous expanse of abundant sand deposits lie across Belet, a large sand sea that occupies a broad equatorial lowland. Another sand sea of interest is Shangri-La, which has a recessed SE margin adjacent to the broad, albedo-bright depression Xanadu. We also found abundant sand deposits within Shangri-La across a corridor between highlands and along the SE boundary of the sand sea. Dune crest orientations across eastern Shangri-La indicate WNW to ESE transport in the region. We propose that the low topography of Xanadu, coupled with the strong gradient in albedo between Shangri-La and Xanadu would generate atmospheric disturbances similar to those responsible for transporting sand across positive changes in elevation on Mars, and may be responsible for the distinct boundary.

VIMS-blue materials are generally associated with water ice mixed with organic compounds. We found that VIMS-blue surfaces across equatorial latitudes tend to be directly adjacent to and upwind of sand seas. This, coupled with geomorphological observations of erosional characteristics and examination of material properties, suggests that sand could at least in part be derived from VIMS-blue materials. We propose 3 environments (alluvial fans, dry lakebeds, and ejecta from impact craters) for sand production using this interpretation and making comparisons with SAR, ISS, and VIMS imagery.

Modeling suggests that Titan's lithosphere significantly thickened 500 m.y. ago. We interpret an elongate exposure of VIMS-blue materials adjacent to Aztlan to be a rift caused by a

thickening of the lithosphere, similar to many of the other icy bodies of the solar system. Our interpretation is further supported by the distribution of cryovolcanic features alongside the proposed rift.

Anomalous VIMS-blue and bright regions within eastern Xanadu are distributed in a pattern that resembles a multi-ringed impact basin. Additionally, when a value threshold was applied to ISS imagery, a bright circular feature was revealed within western Xanadu. These observations suggest two large impacts may have been significantly responsible for creating Xanadu. Comparisons of impact crater models with VIMS imagery of Paxsi, Menrva, Sinlap, Selk, and other craters suggest alternating layers of VIMS-bright and VIMS-blue cover much of the equatorial latitudes of Titan.

We completed ground penetrating radar (GPR) and global positioning system (GPS) surveys across margins of the Kelso Dunes to evaluate the effects of fluvial interaction on sand depth. Our terrestrial model was compared to sand seas on Titan that appear to also have interactions with fluvial channels. Distributions of sand suggest that in both the Kelso Dunes and on Titan, fluvial obstruction is temporary and on Titan isolated across small regions.

This work leads to a better understanding of sand production, accumulation and transport on Titan and in sand seas in general, and reveals a basic stratigraphy of the equatorial regions of Titan. This region is of particular interest because it is the landing site of the Dragonfly mission, now in design.

Keywords: Titan, sand seas, VIMS, ISS, SAR, Cassini

ACKNOWLEDGEMENTS

I acknowledge the supportive efforts of my thesis committee members Jani Radebaugh, Eric H. Christiansen, and Sam Hudson, who thoroughly thought through and tested the logical arguments made in this thesis. I thank the members of the Dragonfly mission who supported my research and gave valuable feedback, including Ralph Lorenz, Elizabeth Turtle, Jason Barnes, and Shannon MacKenzie.

I thank Dylan McDougall, a fellow BYU geology graduate student, who took the time to help me strengthen my arguments made in this thesis.

I also thank my wife Cheyenne Pratt for helping me formulate my findings, and assisting Jani Radebaugh and me with field work at the Kelso Dunes.

TABLE OF CONTENTS

TITLE	i
ABSTRACT.....	ii
ACKNOWLEDGEMENTS.....	iv
TABLE OF CONTENTS.....	v
LIST OF FIGURES	vii
LIST OF TABLES.....	xii
APPENDIX.....	xii
1. Introduction.....	1
2. Methods.....	4
3. Material Properties and Lithostratigraphic Units.....	15
3.1 Material Properties.....	15
3.2 Identification of Lithostratigraphic Units	20
4. Map of Sand and Bedrock Distributions.....	23
5. Interpreted Causes for Sand Distributions	27
5.1 Influence of Topography on Sand Accumulation.....	27
5.2 Opposing Wind Currents Causing Sand Accumulation.....	29
5.3 Influences of Fluvial Margins on Sand Distribution.....	37
5.3.1 Surveying Kelso Dunes, CA as a Terrestrial Analog	37
5.3.2 Results From Surveys and Comparisons with Titan’s Dunes.....	39
6. Exposed Rift of Exposed Icy Organic Bedrock as a Regional Sand Source	45
7. Mid-Latitude Icy Organic Gravel Sheets, Dune Fields and Sand Sheets	49
8. Sand Producing Environments.....	55
8.1 Wind-swept, Reshaped Alluvial Fans.....	55
8.2 Lakebeds	62
8.3 Impact Craters	67
9. Titan’s Stratigraphy and A Proposed Geologic History	67
9.1 Stratigraphy Exposed in Impact Craters	67
9.2 Possible Multiple Impact Origin of Xanadu	72
9.3 A Proposed Geologic History of Titan	74
10. Conclusions.....	75

References.....	78
Appendix.....	85

LIST OF FIGURES

Figure 1. Global VIMS map of Titan with sand sea boundaries outlined. Margins were created from primary map of this work (see Fig. 6).	3
Figure 2. Global <i>Cassini</i> imagery of Titan from the a) Imaging Science Subsystem (ISS), b) Visual and infrared Mapping Spectrometer (VIMS), and c) Synthetic Aperture Radar (SAR) instruments (black areas have no SAR coverage).....	7
Figure 3. Images of eastern Shangri-La in a) ISS, b) VIMS, and c) SAR (underlain by ISS). d) is a stacked image of all imagery with 50% transparency of VIMS and SAR. Observe correlations of overall darker values between all three sets of imagery.	8
Figure 4. Geologic mapping process illustrated by using Sinlap crater. a), c), and e) are VIMS imagery with VIMS-purple, blue, and light blue values outlined respectively. White squares contain colors used by the color select tool in GIMP to select VIMS-values. Specific colors for selections are listed numerically in Table 1. b), d), and f) are ISS imagery with value thresholds 0 – 47, 47 – 70, and 70-117 (reduced by VIMS green channel values 132 – 255) respectively. These thresholds were used to map relative sand abundances. g) Resulting map from color selections and value thresholds when stacked (see Fig. for stacking order). *Remaining unmapped regions were interpreted as bright lithified tholins. Due to strong similarities between VIMS-bright and VIMS-green they were not explicitly mapped, but nearly all unmapped regions across equatorial latitudes appear bright in VIMS.	10
Figure 5. SAR imagery of Sinlap overlain with the outlined margins of regions selected as a) VIMS-purple, c) VIMS-blue, and e) VIMS-light blue in GIMP using color select tool. Inset boxes are locations focused on in b), d), and f) for greater detail. Notice region selected as VIMS-purple contains SAR-dark dunes with SAR-bright interdunes. VIMS-blue and VIMS-light blue have similar SAR-bright values. *VIMS-bright regions were not explicitly mapped, but interpreted based on remaining unmapped regions generally correlating with VIMS-bright values. Notice particularly SAR-bright values across VIMS-bright region. It is important to note that there is some variation in SAR values for VIMS-bright surfaces, as observed by Soderblom et al. (2007). This is due to the 2.17 cm RADAR wavelength used when creating SAR imagery penetrating VIMS-bright materials.	12
Figure 6. Correlations of various shades of gray in ISS and SAR imagery across NW Shangri-La. a) ISS imagery with value thresholds 0 – 47, 47 – 70, and 70 - 117 (reduced by VIMS green channel values 132 – 255) outlined. No VIMS-blue, light blue, or purple regions are present. b) Outlined margins from a) overlain on SAR imagery of same region. Notice correlation between increasingly dark interdunes with lower (darker) ISS values. Some localized offset is due to a lack of detailed georeferencing of imagery. 14	
Figure 7. Stacking order of VIMS color selections, and ISS and VIMS threshold ranges used to create map.....	15
Figure 8. Spectral signatures of bright, brown, blue surfaces in VIMS, and 300 micron sized grains of water ice at 90 K. Adapted from Soderblom et al. (2007).	17

- Figure 9. Region surrounding Huygens landing site in a) ISS, b) VIMS, c) SAR, d) DISR (image credit: ESA/NASA/JPL/University of Arizona/Erich Karkoschka), and e) the geologic map (Fig. 11). Notice strong correlations between DISR, which is near visible light, and ISS. According to the geologic map, the Huygens landing site is surrounded by a surface dominated by icy organic sand partially covering icy organic gravel and bedrock. 21
- Figure 10. Enhanced DISR imagery of a) region NE of Huygens landing site with blank extension to show relative position of landing site and location of b) landing site facing south. Marked distances from probe and 10 cm scale for cobble were adapted from Keller et al. (2008). Outlined location of b) in a) is not to scale. Lithologies are labelled in their various forms that are present within imagery..... 23
- Figure 11. Global equatorial map of relative abundances of icy organic sand, icy organic gravel and bedrock, bright lithified tholins, and regions of icy organic sand partially covering icy organic gravel and bedrock, and icy organic gravel and bedrock partially covering bright lithified tholins. Color scheme is roughly based on the VIMS color scheme created by Le Mouélic et al. (2019). Relative sand abundances mapped as various shades of tan. Areas with most abundant sand are mapped as dark tan and moderately sandy areas are medium tan, both as determined by dark (0 – 47) and moderate (47 – 70) gray values in ISS. Least sandy areas are light tan and were mapped by applying a value threshold of 70 – 117 to ISS, and further restricting the selected area by the extent of 132 – 255 in the green channel of VIMS. The resulting selection was then overlain by all other selections and the remaining extent visible was interpreted as icy organic sand present. Other units were created from color selections on VIMS imagery (see Table 1). *Extent of bright lithified tholins unit was interpreted as being the remaining unmapped regions of the map and were not explicitly mapped due to strong similarities with VIMS-green..... 24
- Figure 12. Global topographic map of Titan by Lorenz et al. (2013) overlain by sand sea margins (filled with fine horizontal lines) and most abundant icy organic sand deposits (filled with thick diagonal lines). Equatorial lowlands roughly correlate with abundant sand deposits, primarily in the case of Belet. 28
- Figure 13. Geologic map centered on eastern Shangri-La. Note the significant coverage of abundant sand along the SE margin of the sand sea, consistent with a dominantly W to E wind direction and some form of obstruction along the eastern margin. Note also the recessed SE boundary where the sand sea abuts Xanadu, which occupies bottom right of figure. 30
- Figure 14. a) Topographic map of Titan (Lorenz et al., 2013) cropped and centered on eastern Shangri-La (outlined) and western Xanadu. Transect A – A' is oriented parallel to linear dune crests at the center of the SE margin of Shangri-La. b) Topographic profile A – A' across Shangri-La and Xanadu. Profile was created from data provided by Titan Trek at trek.nasa.gov/titan. Notice sand sea margin ends at a regional downhill slope. 32
- Figure 15. a) Dunes at the southern margin of the Rub' al Khali Sand Sea (from Google Earth imagery) and b) the southeastern margin of Shangri-La (SAR). Notice comparable patterns in dune morphology and sand sea margins. 33

Figure 16. a) Dominant wind directions as mapped from orientations of barchan dunes (Amin and Seif, 2019). b) Topographic map of the Rub' al Khali Desert. Contour intervals are in meters. Dashed line outlines the margin of the Rub' al Khali Sand Sea, colored tan. Notice the southern sand sea margin's independence from slope gradient and the relatively steep gradients found within the center of the sand sea where the sand migrated unobstructed (2006).	34
Figure 17. Modeled wind vectors with colors representing W to E vector magnitude (Larson, 2019). Xanadu may behave as an atmospheric eddy and deflect westerly winds to the NE preventing sand-bearing winds from passing directly across its surface.....	35
Figure 18. RADAR brightness temperature map of Titan. Eastern Shangri-La outlined (completed by hand tracing around dark values in ISS imagery). Xanadu is cold (Janssen et al., 2016).	36
Figure 19. Topographic profile of Syrtis Major with primary wind directions indicated by orange arrows. (Chojnacki et al., 2019).	36
Figure 20. Google Earth imagery with approximate locations of surveyed transects T1, T2, and T3 annotated as yellow lines. a) Site 1 with T1 and T2, c) Site 2 with T3. b) Google Earth imagery of the Kelso Dunes with survey sites labelled as yellow boxes. d) Locator map showing location of Kelso Dunes within the United States.	39
Figure 21. GPR surveys of T1 (a, b) and T2 (c, d) across margins of the Kelso Dunes. T1 crosses a margin that directly contacts Cottonwood Wash. T2 crosses a margin that has no to very little fluvial interaction. a) and c) are uninterpreted GPR profiles, b) and d) have interpreted lower contacts of dune sand represented by black lines. Bold lines have greater confidence, dashed have low confidence.	41
Figure 22. Annotated topographic profiles T1, T2, and T3 across margins of the Kelso Dunes sourced from GPS surveys. See Fig. 20 for locations. Extent of alluvial fan gravel, dune sand, and water at high flow were interpreted from field observations. Profiles are vertically exaggerated.	42
Figure 23. Fluvial channels (see white brackets) within sand seas and dune fields observed in SAR. Arrows indicate SAR bright regions downwind of channel meanders that may be sand poor due to fluvial activity removing migrating sand that enters the channels. Channels are located within a) Belet, b) southern sand corridor within Fensal near Aztlan, c) eastern crater floor of Forseti, d) southern ejecta of impact crater within Santorini and eastern Shangri-La.	44
Figure 24. A closeup of Fig. 11 showing Fensal and Aztlan sand sea deposits (in tans), the VIMS-blue deposits upwind and adjacent to the sand seas, and a narrow band of VIMS-purple interpreted to be deposits of sand that partially cover underlying VIMS-blue.	46
Figure 25. a) Sapas Mons from SAR imagery captured from Magellan on Venus. b) Interpreted cryovolcanoes from Cassini SAR imagery on Titan within interpreted rift. c) VIMS imagery centered on interpreted rift with location of b) outlined by black and yellow box. Location of Doom Mons is labelled with a black and yellow circle. Axis of interpreted rift is outlined with a light blue line.	48
Figure 26. Lobate sand sheets associated with maculas. Elpis Macula (top), Omacatl Macula (middle), and Genetaska Macula (bottom) with diffuse downwind sand deposits in VIMS, ISS, and SAR (left to right). All are VIMS brown, ISS dark, and portions are SAR dark. See Fig. 28 for reference.	50

Figure 27. SAR imagery of linear, possibly stabilized dunes at or near mid-latitudes. Yellow ovals denote locations of observable linear dunes. a) Perkunas Virgae, a region south of southeastern Shangri-La at -28° , 159° , that was previously mapped as having sand dunes (Brossier et al., 2018). b) Winia Fluctus, far north of Fensal at 53° , 42° , is a SAR-bright lobate feature with features previously interpreted to be linear dunes (Rodriguez et al., 2014; Lopes et al., 2019). Narrow, SAR-bright features are consistent with radar reflections seen on dunes at equatorial latitudes (Neish et al., 2010). Dominant wind directions in both images are from the WNW (Malaska et al., 2016). See Fig. 13 for locations.	53
Figure 28. Global ISS imagery as a locator map outlining interpreted VIMS-blue gravel sheets (orange rectangles) and lobate VIMS-brown sand sheets (yellow circles). Areas of interest focused on in this work are labelled. Compare with Fig. 1.....	54
Figure 29. Illustration adapted from Hesse (2019), which was adapted from Weismann et al. (2010) showing affects of aridification on a system of alluvial fans. Over time, wind dominates the transportation of sediment, sorting out sand from the alluvial fans and burying them.	56
Figure 30. Leilah Fluctus, a SAR-bright surface immediately downwind of and possibly sourced from wind-swept alluvial fans at 51.2° N, 100.7° E, roughly 475 km north of Fensal. Dominant wind direction is ESE. White arrow is directed towards an interpreted dune field with linear dunes.....	57
Figure 31. Block diagram of sand produced from isolated wind-swept alluvial fan at a temperate latitude based on observations of Leilah Fluctus (Fig. 30). a) VIMS color scheme and b) Huygens descent imagery (near true color) color schemes.	58
Figure 32. Illustrations depicting the primary interpreted method of sand production on Titan. a) VIMS color scheme and b) Huygens descent imagery (near to true visible color) color schemes. Occasional storms fill drainages and liquid methane rivers fluvially erode VIMS-blue and overlying VIMS-white materials into sediments, which are deposited at the terminus of drainages. Wind transports gravels and sand downwind of the drainages and organizes the sediments into VIMS-blue gravel sheets and VIMS-brown sand seas. VIMS-bright materials quickly disintegrate and dissolve. During wetter climates alluvial fans prograde, while during dry climates sand deposits transgress across the basin. These cycles are preserved in patterned deposits beneath the sand sea.	60
Figure 33. a) Western Nafud desert upwind of Nafud Sand Sea showing jointing within the light tan Tabuk sandstone, and overlying dark basalt flows. b) Huygen descent imagery showing similar jointing to a) within a dark brown material correlated with VIMS-blue. c) Same as a), but with values inverted and covered with a partly transparent orange-brown layer in GIMP for further comparison with b).	62
Figures 34. SAR imagery of a) previously identified active lakes (L) and paleolakes (bright lobate patches covering much of image, outlined by distinct bright and dark margins) in polar regions (Moore and Howard, 2010). b) Eastern Shangri-La with a SAR-bright channel leading to an interpreted SAR-dark paleolake, and c) eastern Belet with several probable SAR-dark paleolakes. Notice consistent morphology, but different scattering properties of the surfaces of these interpreted paleolakes. It is likely that the bright polar paleolakes are covered with rough textured evaporite deposits, while dark equatorial paleolakes are behaving as sediment sinks and are accumulating sand.....	64

Figure 35. Omacatl Macula, a probable dried lakebed containing VIMS-brown sediment surrounded by VIMS-bright deposits acting as a sand source for an isolated sand sheet. a) ISS, b) VIMS, and c) SAR.	65
Figure 36. A model of a dried lakebed containing VIMS-brown sediment surrounded by VIMS-bright deposits acting as a sand source for an isolated sand sheet. Based on observations of macula in SAR and VIMS (Fig. 35), and mapped interpretations by Brossier et al. (2018). VIMS color scheme a), and color scheme based on Huygens descent imagery b).	66
Figure 37. Sinlap, Selk, and Paxsi impact craters ordered according to increasing level of degradation (left to right), with rim diameters of 88 km, 84 km, and 115 km respectively (diameters measured by Hedgepeth et al., 2018). Top row is VIMS, bottom row is ISS. Notice that even after significant erosion there are still both VIMS-blue and VIMS-bright materials present.	68
Figure 38. Cross sections of Upheaval Dome, a confirmed weathered impact crater with central uplift. Adapted from Kenkmann, et al., 2005. Compare with Fig. 37 and 39.	69
Figure 39. Diagram outlining proposed geologic history of Sinlap crater. a) Moment of impact. Solid ejecta is thrown into the atmosphere. b) Elastic rebound creates a central peak within impact crater. Solid ejecta falls to the surface covering eastern Fensal and is organized with an inverted stratigraphy of the subsurface. Vaporized materials, including water ice, condense as a large cloud. c) The water ice bearing cloud is transported by wind, further condenses and precipitates VIMS-blue materials onto ejecta and crater floor as a thin blanket. d) Precipitated methane erodes away much of the thin layer of VIMS-blue across the upper slopes of ejecta and central peak, and reveals the underlying VIMS-bright ejecta and bedrock respectively. Fluvial channels expose VIMS-blue ejecta. Wind removes some VIMS-bright clasts on the upwind flanks of the exposed ejecta and exposes some underlying VIMS-blue ejecta. Sand from Fensal migrates over some upwind margins of ejecta and landslides occur within the crater.	71
Figure 40. a) A close up of Fig. 11 showing eastern Xanadu. b) Fig. a) with annotated multi-ringed impact basin. c) Tethys with 450 km wide Odysseus Crater occupying the upper left of image. NASA/JPL/Space Science Institute.	73
Figure 41. a) Original VIMS imagery. Box outlines location of b), western Xanadu in VIMS with value inversion applied in GIMP to exaggerate fluvial channels obscured in SAR. c) VIMS imagery with a value threshold of 181 – 255 applied in GIMP, revealing a large circular feature within western Xanadu. d) A cropped image of b) with interpreted fluvial channels.	74
Figure 42. Sand production from VIMS-blue impact crater ejecta. VIMS color scheme A), and color scheme based on Huygens descent imagery B). Diagrams are based on observations of Sinlap crater in VIMS, ISS and SAR imagery, and a topographic profile. We suggest that large impactors struck the surface of Titan after some VIMS-bright had been deposited, created interpreted impact basins within Xanadu (see Section 8.2), and spread VIMS-blue materials across much of the surface. More VIMS-bright then was deposited and created alternating layers of VIMS-bright and blue at depth. See Section 8 for more on interpreted stratigraphy.	86

LIST OF TABLES

Table 1. Colors in VIMS imagery used by color select tool in GIMP to select VIMS-blue, light blue, and purple regions. Colors are listed as values within the RGB color scheme. Each color selection was centered on these colors, and included all other colors within the listed thresholds (+/-). All values and thresholds are listed as standardized values between 0 – 255 according to the RGB color scheme.	9
Table 2. Units from map (Fig. 11) with descriptions, interpreted origins and colors as seen in ISS, VIMS, and SAR. Probable visible light colors are also listed as interpreted from Huygens descent imagery.	25

APPENDIX

Appendix.....	85
---------------	----

1. Introduction

Equatorial regions of Saturn's moon Titan are dominated by vast sand seas arranged primarily in linear dunes (Lorenz et al., 2006; Barnes et al. 2008; Radebaugh et al., 2010; Radebaugh, 2013; Lucas et al. 2014). These sand seas are large, covering up to 18% of the surface (Rodriguez et al. 2014; Arnold 2014), which is more than the Saharan and Arabian sand seas of Earth combined. Titan's dunes have many morphological similarities to terrestrial dunes, such as those found in the Namib Sand Sea and the Sahara Desert (Lorenz et al., 2006; Radebaugh et al., 2010). Dunes from both bodies have patterns that indicate topographic obstacles cause diversion of flow around them, or obstruct migration (Radebaugh et al., 2010). This apparent flow is down the dune long axis, so consequentially crests appear to be oriented along the average direction of sand migration (Courrech du Pont et al., 2014; Lucas et al., 2014).

Sands as seen with the Cassini Visual and Infrared Mapping Spectrometer (VIMS) are most consistent with organic compounds and possibly some water ice (Soderblom et al., 2007; Jaumann et al. 2009; Mouelic, 2019). Organic compounds within the sands likely originated from tholins, which are complex organic molecules formed from interactions between solar ultraviolet radiation and atmospheric methane and nitrogen (Soderblom et al., 2007). Over time these complex organic molecules clump together, "snow" down, and accumulate on the surface (Radebaugh et al., 2013; Barnes et al., 2015). Basic questions for aeolian environments on Titan still remain, such as what are the sand sources, how is sediment produced, where does sand tend to accumulate within sand seas, and how far has the sand migrated (Barnes et al., 2015; Charnay et al., 2015; Malaska et al., 2016). Barnes et al. (2015) presented three methods for sediment production: sintering and accretion of organic tholins (also discussed in Lapotre et al. 2022), flocculation of organic compounds within methane lakes, and aeolian erosion of evaporite deposits. Radebaugh et al. (2013) also

proposed that dune sand may originate through fluvial erosion of lithified tholin deposits. In regards to previous conclusions about how far dunes have migrated, Barnes et al. (2015) claimed dunes have migrated entirely around Titan's equator and effectively formed one large sand sea, while Charnay et al. (2015) argued that dunes may have migrated only 45 km.

A sand sea of particular interest on Titan is Shangri-La, centered on 15° E, 5° S. It spans approximately 3,700 km E-W and 2,300 km N to S, and is over 7 times larger than the largest sand sea on Earth, the Rub' al Khali (Abdallah and Kumar, 2011). Shangri-La resides just west of the lowland region Xanadu (Fig. 1), which contains rugged, mountainous terrain and well-developed river channels (Burr et al., 2009; Radebaugh et al., 2011; Matteoni et al., 2020). The SE boundary of Shangri-La is recessed along its margin adjacent to Xanadu. Available topographic data and imagery (Figs. 14, 15) indicate there is no substantial topographic obstacle, which means this boundary is unusual as terrestrial dune field margins are typically controlled by highland topography (Lancaster, 1995). Barnes et al. (2015) compared the SE boundary of Shangri-La to the similarly distinct northern boundary of the Namib Sand Sea, which is largely defined by an ephemeral drainage. Based on the topographic data for the area surrounding the SE margin of Shangri-La, this would require the region-bounding drainage to be perpendicular to regional slope for hundreds of kilometers and no such drainage is visible to the Cassini image resolutions (~ 0.5 km/pixel). Knowing where sand is sourced and collects in Shangri-La is of great importance because it is the site of the Dragonfly lander, a NASA rotorcraft lander mission to be sent to Shangri-La to study the sand dunes and complex organic compounds there (Turtle et al., 2020). Studies of these processes may also reveal the nature of the transition between the sand sea and the Xanadu region.

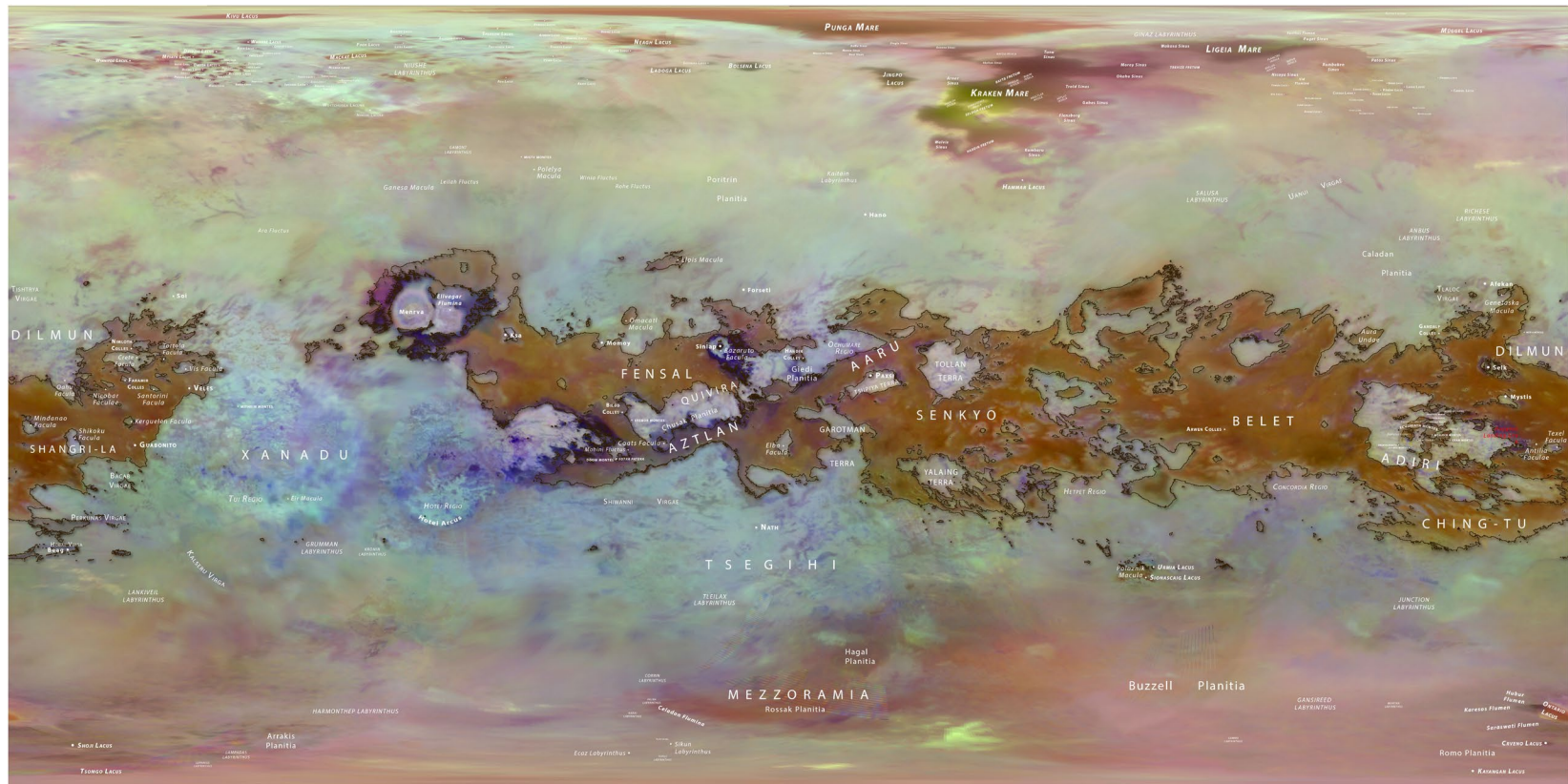


Figure 1. Global VIMS map of Titan with sand sea boundaries outlined. Margins were created from primary map of this work (see Fig. 6).

The purpose of this study is to map the relative abundances of sand within sand seas and potential sand source materials across the equatorial latitudes of Titan, and make interpretations to better understand Titan's aeolian environments and geologic history. Previous studies have mapped sand sea margins (Rodriguez et al., 2014; Arnold, 2014; Malaska et al., 2016), but have not focused on mapping sand abundances, which we define in Section 2. Mapping sand distributions and abundances reveals patterns in sediment transport and accumulation, and also reveals regions affected by obstruction of sand movement. It may also provide insights into the geologic history of Titan and erosional and depositional processes. We examined the distributions of VIMS-bright, VIMS-brown, and VIMS-blue materials in order to determine potential sand sources. We also studied the presence of alternating VIMS-bright and VIMS-blue surfaces within impact craters, and examined what they indicate about a possible stratigraphy for Titan. Our interpretations concerning interactions between fluvial and aeolian processes was supplemented by calculated sand depths of the Kelso Dunes in the Mojave desert from GPR and GPS surveys. This field study helped constrain some aspects of the obstruction of sand migration on Titan.

This work helps extend our understanding of the surface of Titan and provides context for the future data that will be provided from Dragonfly.

2. Methods

We sought to create a map of the equatorial region of Titan by making correlations concerning presence and abundance of sand across Cassini VIMS, Imaging Science Subsystem (ISS), and Synthetic Aperture Radar (SAR) imagery (Figs. 2, 3). ISS relies on visible to near-infrared wavelengths within windows that allow imaging of the surface (Fig. 2a). The instrument utilized wavelengths of 200 - 1050 nm and has generally greater resolutions of 2 - 3 km/pixel across the

equatorial latitudes (Porco et al., 2005), which are focused on in this study. ISS is most similar to visible light imagery and reveals compositional differences of the surface.

VIMS imagery was developed using spectra obtained at wavelengths of 300 - 5100 nm. Like ISS, wavelengths used for VIMS imagery were also within spectral windows which are able to pass through the atmosphere and reveal compositional differences of the surface (Le Mouélic et al., 2019). VIMS resolutions range widely from 10 - 1.5 km, however much of the imagery has a resolution of 1.4 km/pixel. The color scheme for the VIMS mosaic used is red: 1.59/1.27 μm ; green: 2.03/1.27 μm ; blue: 1.27/1.08 μm (Le Mouélic et al., 2019). VIMS-bright regions correlate with ISS-bright, and both VIMS-brown and VIMS-blue correlate with ISS dark to light gray. Both ISS and VIMS images contain significant contamination from atmospheric absorptions, and the severity of this contamination varies across the global image map. Radiative transfer models have sought to diminish this contamination with some success, but caution should be exercised in applying interpretations of spectra and compositions. This was done for this study through examining broad regional trends rather than small-scale interpretations.

SAR imagery was obtained as active imagery utilizing the wavelength of 2.17 cm and illustrates textural characteristics of near surface materials (Fig. 2c). Dark surfaces are smooth enough to reflect the RADAR signal and are thought to be in general covered with sand sized grains (0.1 – 0.3 mm in diameter [Lorenz et al., 2006]). Bright surfaces are rough and scatter the RADAR signal, causing more of the original signal to be reflected towards the SAR instrument. These images were obtained in long “swaths” as Cassini flew past Titan, such that the centers of each swath were narrowest (~150 km) and had the highest image resolutions. Nearly 50% of the surface was imaged in SAR, compared to nearly global coverage with the other two instruments

(Fig. 2). Notwithstanding its limited coverage, SAR imagery provides the highest resolution of up to 0.5 km/pixel (Elachi et al., 2005).

Although the Huygens probe Descent Imager and Spectral Radiometer (DISR) imagery was not used directly in mapping, it was used to further support our mapped interpretations and to assist with identifying lithostratigraphic units (see Section 3.2). DISR captured imagery during the descent and soon after the landing of Huygens probe. DISR utilized wavelengths of 660 to 1000 nm, and had a spatial range of 8.3° to 96° from nadir (Keller et al., 2008) and the imagery is most similar to what an observer would see in visible light.

Significant correlations of boundaries, colors, and brightnesses can be seen between all three image datasets (Fig. 3).

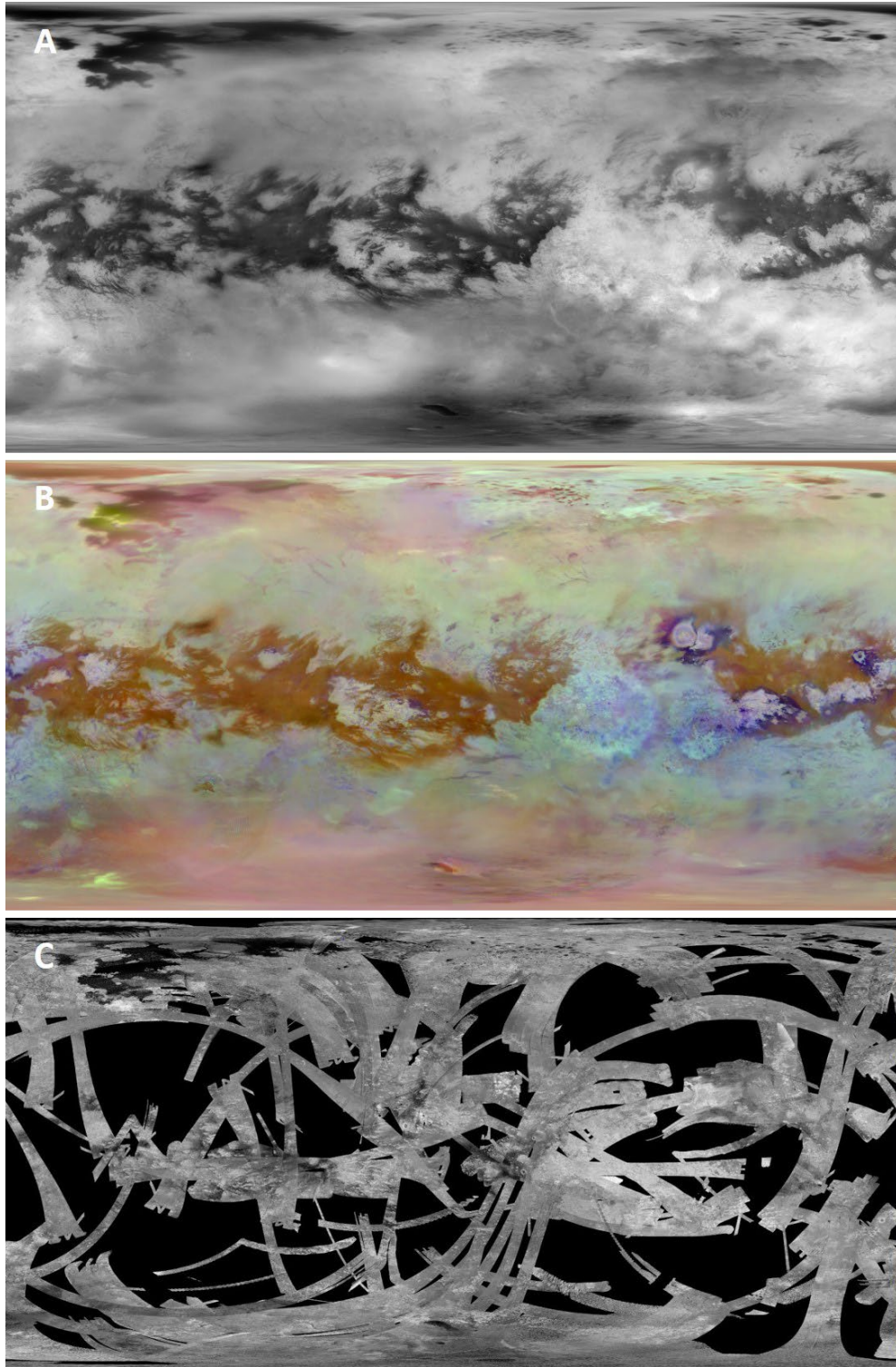


Figure 2. Global *Cassini* imagery of Titan from the a) Imaging Science Subsystem (ISS), b) Visual and infrared Mapping Spectrometer (VIMS), and c) Synthetic Aperture Radar (SAR) instruments (black areas have no SAR coverage).

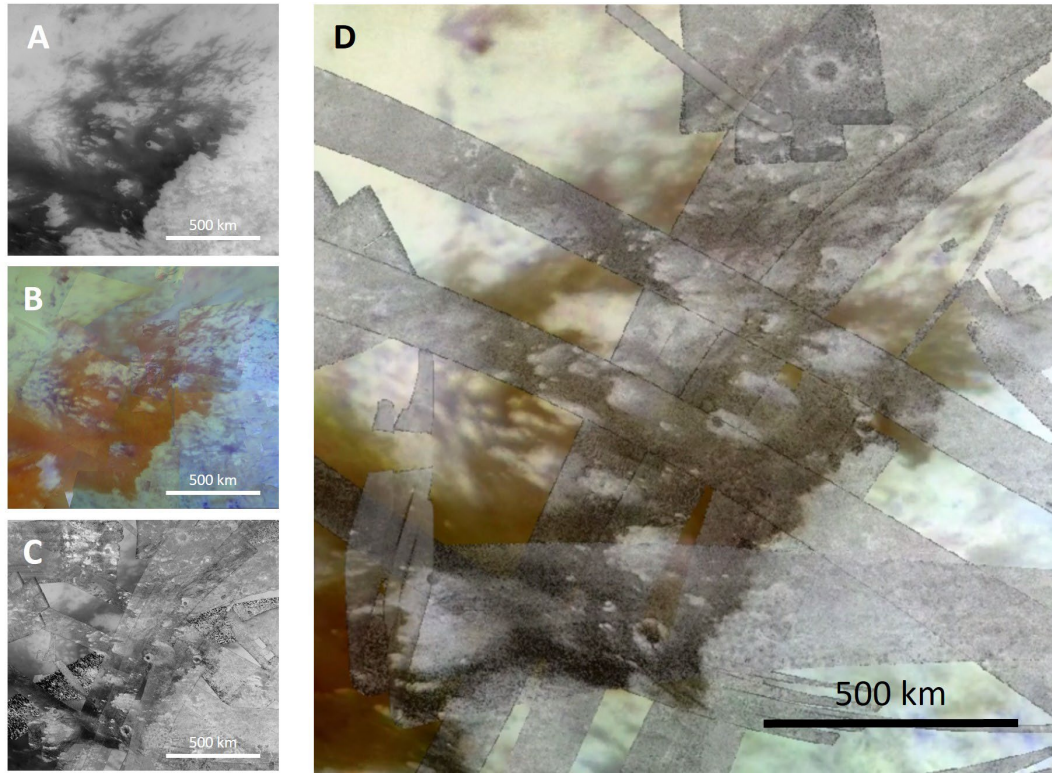


Figure 3. Images of eastern Shangri-La in a) ISS, b) VIMS, and c) SAR (underlain by ISS). d) is a stacked image of all imagery with 50% transparency of VIMS and SAR. Observe correlations of overall darker values between all three sets of imagery.

Mapping was done using color and value threshold tools in GNU Image Manipulation Program (GIMP) on VIMS and ISS published global imagery respectively. Due to a range of colors existing across sand seas and VIMS-blue surfaces, the color select tool was applied on various color ranges of blue and purple. An illustrated example of this mapping method is shown in Figure 4. RGB channels for colors are also measured from 0 to 255 within each channel. The following chart includes all colors and color thresholds used to create the map.

VIMS Surface	Channel	Value									
VIMS Blue	R	45	86	61	81	53	48	54	15	15	20
	G	25	78	55	47	27	19	55	20	4	1
	B	69	121	145	100	94	147	103	84	108	153
	Threshold	25.8	25.8	25.8	25.8	25.8	25.8	25.8	25.8	25.8	25.8
VIMS Light Blue	R	102									
	G	98									
	B	140									
	Threshold	26.8									
VIMS Purple	R	99	97	119	90	75	84	115	113		
	G	65	87	59	51	45	82	90	94		
	B	86	98	114	61	61	95	94	98		
		19.8	12.8	17.8	13.8	19.8	12.8	13.8	15.8		

Table 1. Colors in VIMS imagery used by color select tool in GIMP to select VIMS-blue, light blue, and purple regions. Colors are listed as values within the RGB color scheme. Each color selection was centered on these colors, and included all other colors within the listed thresholds (+/-). All values and thresholds are listed as standardized values between 0 – 255 according to the RGB color scheme.

We mapped VIMS-purple, blue, and light blue regions using the color select tool on the colors and thresholds listed in Table 1. Due to VIMS-bright being strongly similar in color with VIMS-green, we did not explicitly map VIMS-bright surfaces. We acknowledge that these surfaces have been differentiated in other studies (Lopes et al., 2016; Solomonidou et al., 2018). Because much of the equatorial latitudes lack significant VIMS-green values, we interpreted the remaining unmapped regions as being covered with VIMS-bright. This method is similar to Brossier et al., (2018).

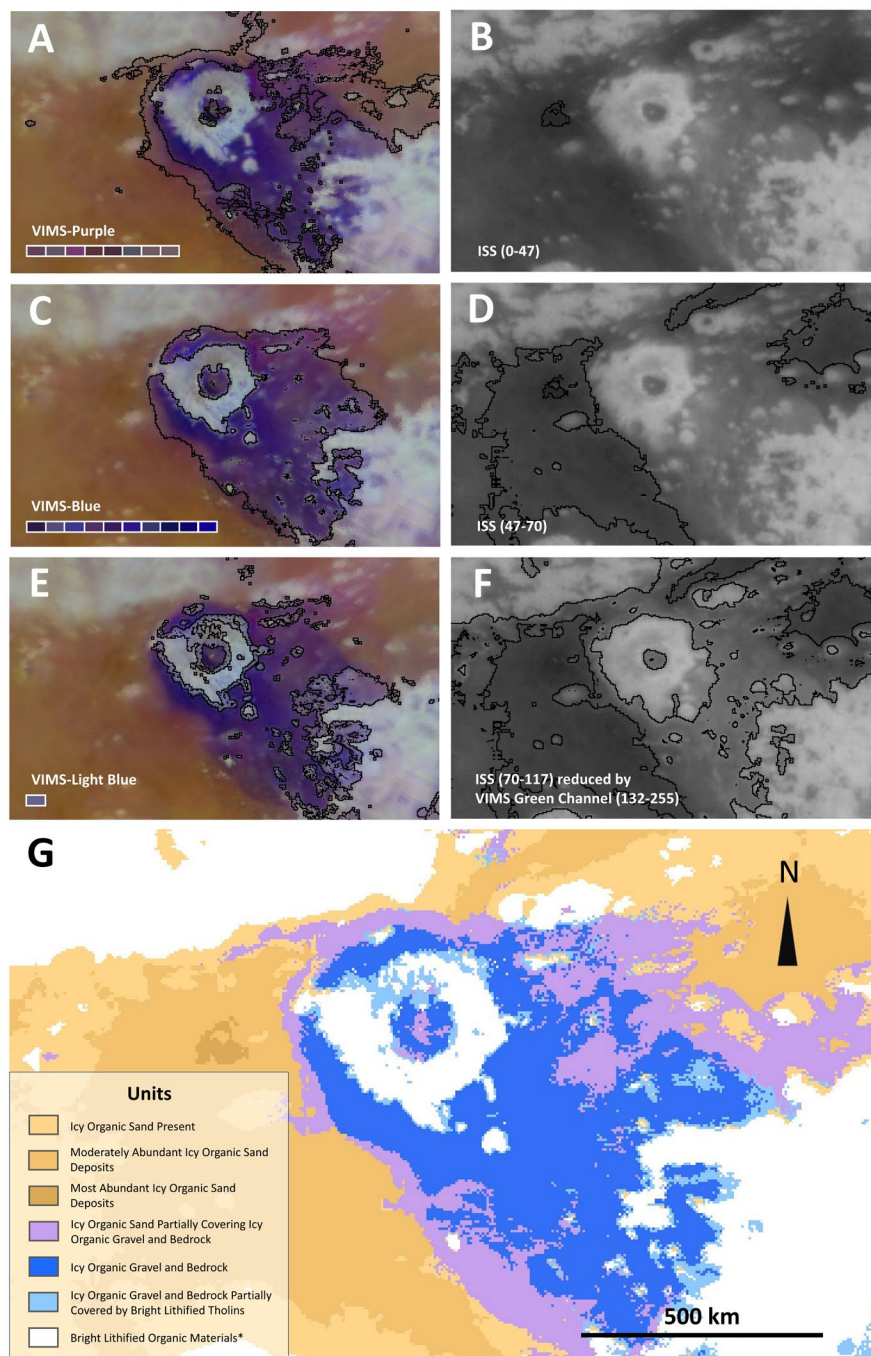


Figure 4. Geologic mapping process illustrated by using Sinlap crater. a), c), and e) are VIMS imagery with VIMS-purple, blue, and light blue values outlined respectively. White squares contain colors used by the color select tool in GIMP to select VIMS-values. Specific colors for selections are listed numerically in Table 1. b), d), and f) are ISS imagery with value thresholds 0 – 47, 47 – 70, and 70-117 (reduced by VIMS green channel values 132 – 255) respectively. These thresholds were used to map relative sand abundances. g) Resulting map from color selections and value thresholds when stacked (see Fig. for stacking order). *Remaining unmapped regions were interpreted as bright lithified tholins. Due to strong similarities between VIMS-bright and VIMS-green they were not explicitly mapped, but nearly all unmapped regions across equatorial latitudes appear bright in VIMS.

VIMS color selections were correlated with SAR imagery (Fig. 5) to assist with the creation of unit descriptions. VIMS-purple surfaces have previously been interpreted as regions where VIMS-brown sand dunes exist with VIMS-blue interdunes (Rodriguez et al., 2014). Correlations with SAR and VIMS imagery support this interpretation, as SAR-dark dunes are present within VIMS-purple regions (Fig. 5). It is likely that VIMS-purple surfaces are the result of the low resolution imagery blurring together VIMS-brown dunes and VIMS-blue interdunes.

We also found that VIMS-blue and light blue surfaces tend to be SAR-bright. Regions interpreted to be VIMS-bright are also SAR-bright, however as Soderblom et al. (2007) observed there is some variability.

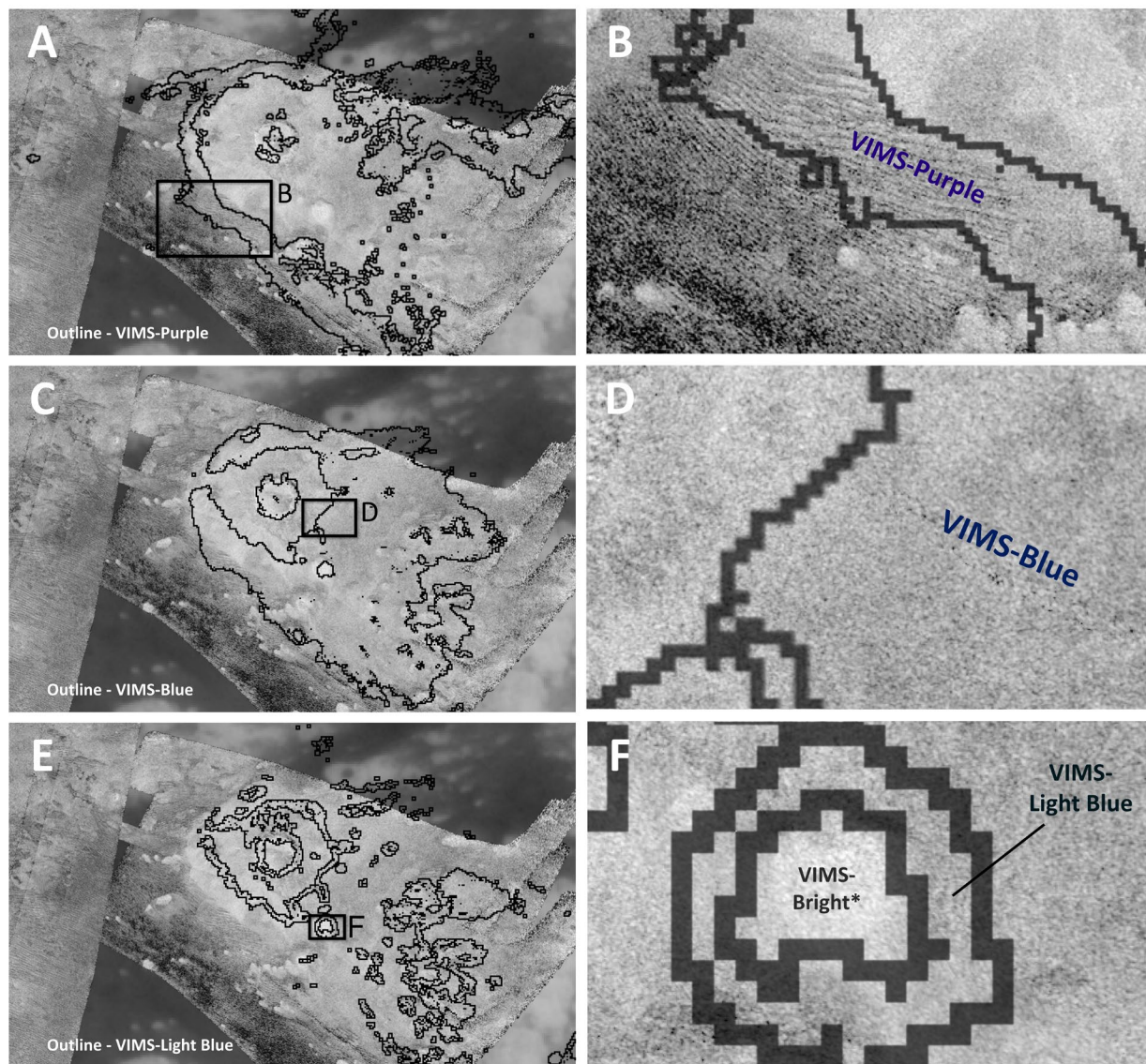


Figure 5. SAR imagery of Sinlap overlain with the outlined margins of regions selected as a) VIMS-purple, c) VIMS-blue, and e) VIMS-light blue in GIMP using color select tool. Inset boxes are locations focused on in b), d), and f) for greater detail. Notice region selected as VIMS-purple contains SAR-dark dunes with SAR-bright interdunes. VIMS-blue and VIMS-light blue have similar SAR-bright values. *VIMS-bright regions were not explicitly mapped, but interpreted based on remaining unmapped regions generally correlating with VIMS-bright values. Notice particularly SAR-bright values across VIMS-bright region. It is important to note that there is some variation in SAR values for VIMS-bright surfaces, as observed by Soderblom et al. (2007). This is due to the 2.17 cm RADAR wavelength used when creating SAR imagery penetrating VIMS-bright materials.

Values in ISS images are measured from 0 (black) to 255 (white). Relative abundances of sand were mapped by applying value thresholds in GIMP and correlating black to dark gray values of 0 - 47 in ISS imagery with the most abundant sand, less dark values of 47 - 70 with moderately abundant sand, and moderate gray values of 70 – 117 (with a reduction by the extent of 132 – 255 in the VIMS green channel and color selections of VIMS-blue, light blue, and purple) with sand being present. While ISS values of surface materials can be contaminated by atmospheric absorptions as previously discussed, the chosen ISS values are broadly consistent with particular SAR terrains. For example, there is a correlation between ISS-dark regions and dunes with varying shades of gray (assumedly due to varying coverage of sand) across interdunes in SAR (Fig. 6). Particularly dark regions in ISS correlate with dark regions in SAR and therefore have sand-rich interdunes, which can occur within sand seas on Earth (Liang et al., 2020). Dunes are generally more tightly spaced within these regions, which may also contribute to darker ISS values and leads to our interpretation of greater sand abundance (Fig. 6).

Attempts were made to map the outer “sand present” regions of sand seas by making color selections on shades of brown in VIMS imagery, however we found that the results were restricted by the poorer image quality of VIMS. After thoroughly comparing generated maps to SAR, ISS, and VIMS imagery, we found that our method that relied most heavily on ISS imagery was most capable of mapping these outer regions of the sand seas. This method builds upon that used by Arnold, (2014), who mapped the extent of sand seas by applying a threshold of 0 – 155 on ISS imagery.

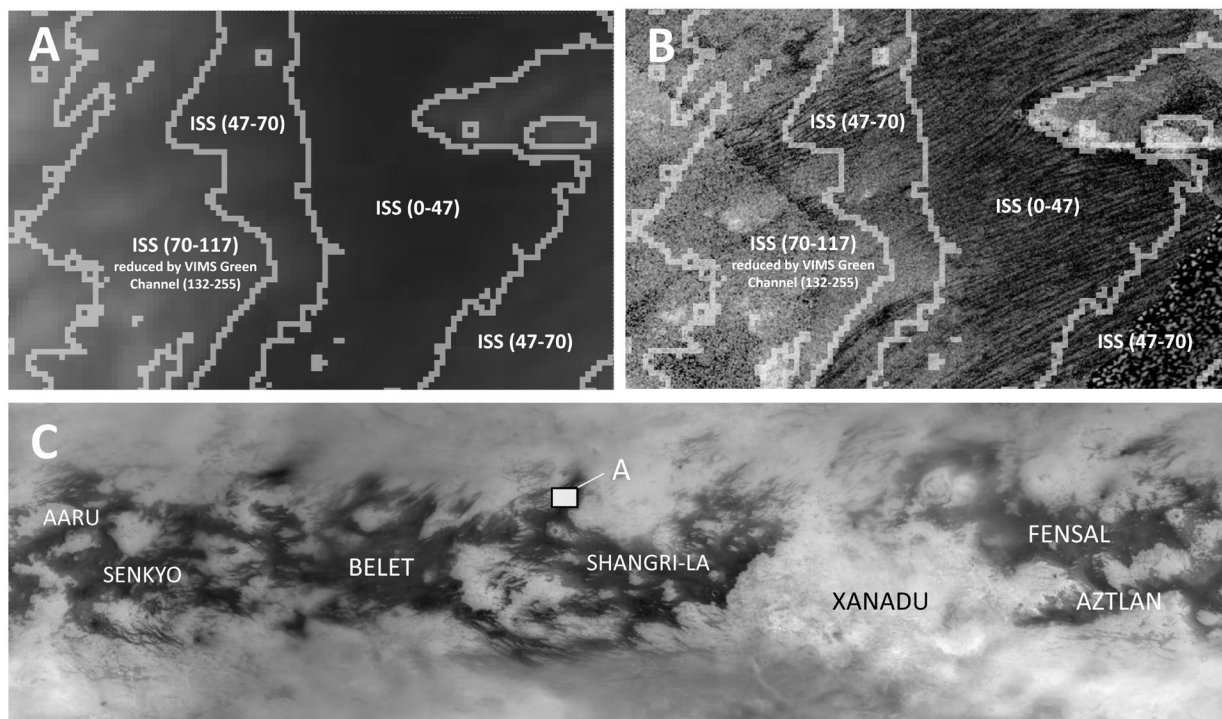


Figure 6. Correlations of various shades of gray in ISS and SAR imagery across NW Shangri-La. a) ISS imagery with value thresholds 0 – 47, 47 – 70, and 70 - 117 (reduced by VIMS green channel values 132 – 255) outlined. No VIMS-blue, light blue, or purple regions are present. b) Outlined margins from a) overlain on SAR imagery of same region. Notice correlation between increasingly dark interdunes with lower (darker) ISS values. Some localized offset is due to a lack of detailed georeferencing of imagery.

Sand sea boundaries (Fig. 1) were determined from the most distal extents of VIMS-brown and VIMS-purple surfaces, which is a similar method to that of Rodriguez et al. (2014).

Once all surfaces were selected, they were stacked in the order that resulted with the most accurate map (Fig. 7).

ISS (0 – 47)

ISS (47 – 70)

VIMS-Purple

VIMS-Blue

VIMS-Light Blue

ISS (70 - 117)

Reduced By Extent of 132-
255 in VIMS Green Channel

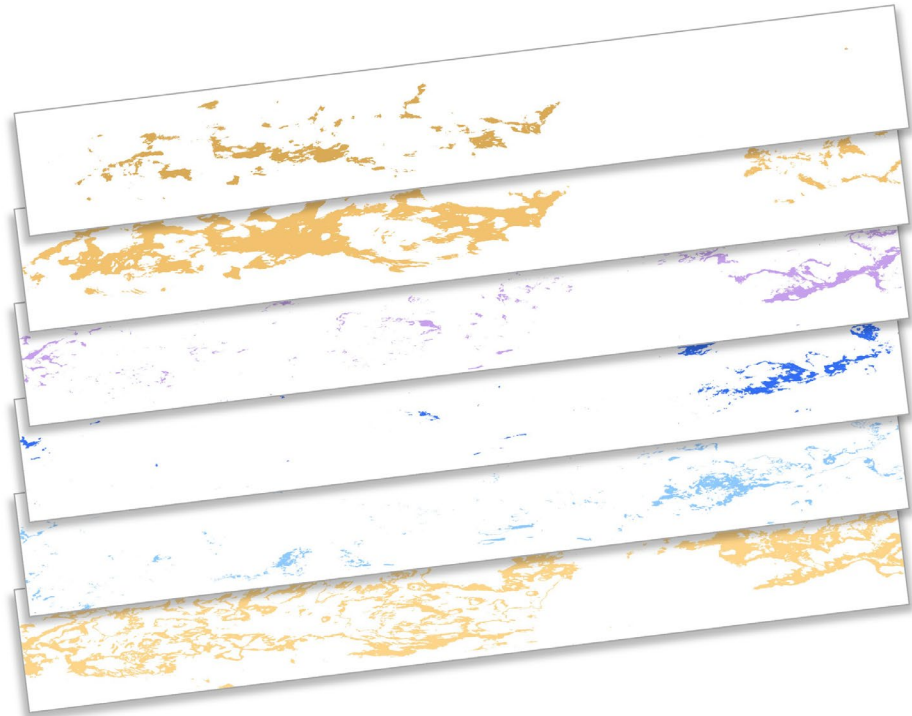


Figure 7. Stacking order of VIMS color selections, and ISS and VIMS threshold ranges used to create map.

3. Material Properties and Lithostratigraphic Units

With material units mapped, we seek to understand what the various units may mean for the surface geology of Titan.

3.1 Material Properties

Previous work (Jaumann et al., 2008; Radebaugh 2013; Barnes et al., 2015; Malaska et al., 2016; Brossier et al., 2018) sought to determine sand sources on Titan. Sand sources for sand seas on Earth are often found within, or near sand seas (Lancaster, 1995). Thus, an examination of the surface of Titan suggests that VIMS-bright, VIMS-blue, and even VIMS-brown materials (if there are lithified VIMS-brown materials not visible as distinct from mobile sand) are all sand source candidates.

VIMS-blue and VIMS-brown spectral signatures suggest both materials are made of water ice and organic compounds, while there is likely little to no water ice in VIMS-bright materials (Fig. 8; Jaumann et al., 2009; McCord et al., 2006; Soderblom et al., 2007). It is assumed that because of troughs in the spectral signature of water ice at roughly 1.57 and 2.01 μm , some presence of water ice within VIMS-brown and VIMS-blue materials suppressed the peaks of their spectral signatures at those same wavelengths relative to the much higher peaks of VIMS-bright surfaces. Minor differences between spectral signatures of VIMS-blue and VIMS-brown surfaces are attributed to VIMS-blue having greater concentrations of water ice, or differences in grain size (Jaumann et al., 2009; Mouelic, 2019). Jaumann et al. (2009) normalized the spectral signatures of these surfaces and concluded that VIMS-blue and VIMS-brown materials are likely the same compositionally, but are comprised of different sizes of sediment. Supporting evidence for this interpretation can be found from correlations with SAR imagery, which consistently show that VIMS-blue surfaces tend to be more SAR-bright, and are therefore likely made of larger clasts (~ 2 cm being the optimal size for SAR brightness/roughness; Le Gall et al. 2010) than VIMS-brown, SAR-dark sand.

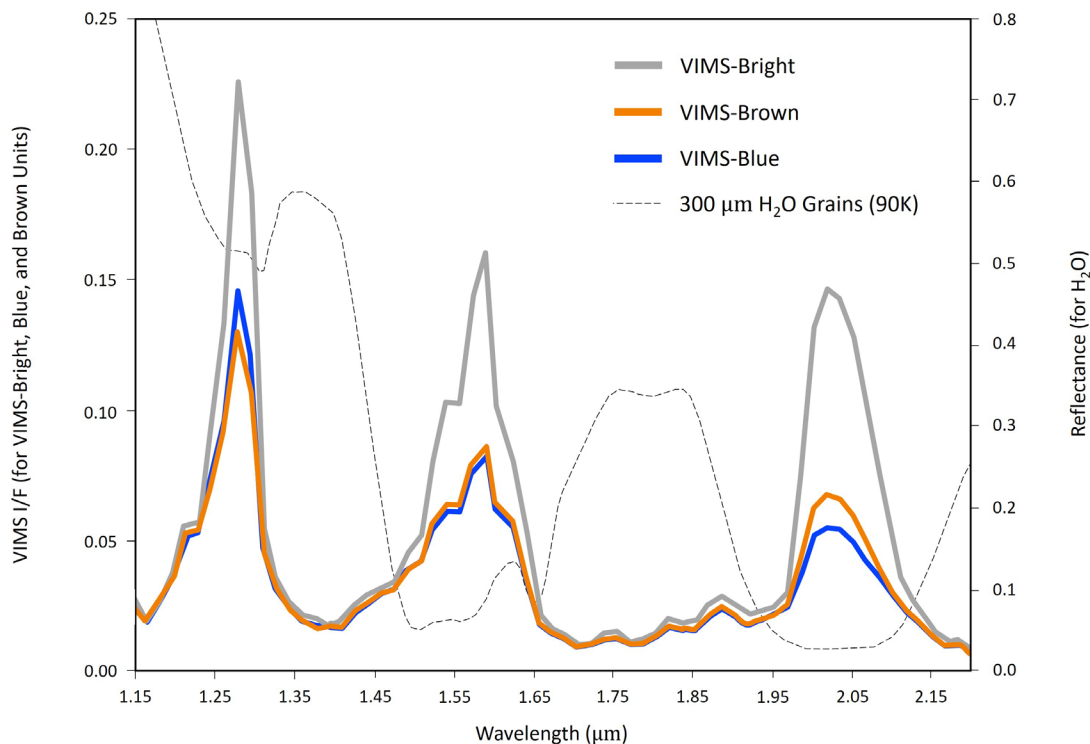


Figure 8. Spectral signatures of bright, brown, blue surfaces in VIMS, and 300 micron sized grains of water ice at 90 K. Adapted from Soderblom et al. (2007).

Thus, larger VIMS-blue clasts may fluentially erode and then comminute from further erosion to sand and consequentially appear VIMS-brown. Brown features imaged by the Huygens Descent Imager/Spectral Radiometer (DISR) are correlated with both VIMS-blue and VIMS-brown surfaces. Contrastingly, bright regions in DISR appear bright in VIMS (Le Mouélic et al., 2019, Soderblom et al., 2007). Although sediments on Earth can darken from exposure to the sun, or erosion into smaller clast sizes, the VIMS-bright and VIMS-brown surfaces are significantly different spectrally and thus not likely made of the same materials.

In addition to spectral data, there is geomorphological reasoning to suggest that sand is sourced from VIMS-blue materials. The shapes of upwind sand sea margins often reflect shapes of adjacent upwind VIMS-blue margins. Outside of the rugged Xanadu region, a few impact

craters, and northern and southern limits to sand seas, wherever there is VIMS-blue sand is found immediately downwind (Fig. 6).

The sand of Titan is likely to be relatively durable, because the dunes are assumed to be millions of years old (Barnes et al., 2015) and may have migrated many kilometers. Assuming the sand and its source are both durable materials, we suggest that sand is not generally sourced from VIMS-bright materials as they appear to be weaker, more porous, and methane-soluble than VIMS-blue materials. There are several lines of evidence for this:

1) Mechanical Strength

Typically, deeper-sourced rocks on Earth tend to be more durable, and the VIMS-blue surfaces on Titan are assumed to be from a layer beneath much of the visible VIMS-bright, organic-rich surfaces (Brossier et al., 2018, Soderblom et al., 2007). Laboratory experiments with water ice and lab-created tholins found tholins (which may form the VIMS-bright materials) to be more brittle than water ice (Yu et al., 2018).

2) Porosity

Deeper-sourced rocks on Earth also tend to be less porous, suggesting the stratigraphically lower VIMS-blue materials on Titan are also less porous. Additionally, VIMS-bright materials have been interpreted to be more transparent in SAR than VIMS-brown or VIMS-blue materials (Soderblom et al., 2007), which suggests that they may be relatively porous and weakly compacted. Furthermore, observations of headward erosion and rounded valleys in VIMS-bright deposits similar to spring-fed drainages in the south-western U.S. imply subsurface flow (Malaska et al., 2020). Some of these morphologies are even seen in the Huygens landing site drainages. This suggests VIMS-bright materials are more permeable than VIMS-blue materials.

3) Solubility

Lakebeds covered with evaporites have been interpreted within southern Xanadu (Moore and Howard, 2010) and are spectrally similar to VIMS-bright surfaces (MacKenzie et al., 2014). Several lacustrine features surrounded by VIMS-bright regions have been interpreted to have karst morphologies (Cornet et al., 2015). Altogether, this suggests that VIMS-bright materials may be soluble in methane. This interpretation is further supported by solubility experiments with lab-created tholins in methane and ethane (Carrasco et al., 2009; Coll et al., 1999; McKay et al., 1996). Evaporites can form local sand sources as in White Sands, NM, but the sands must be continually re-supplied and do not often travel far because of their ability to dissolve in precipitation. As there is little correlation between the distribution of VIMS-bright surfaces and adjacent downwind sand seas, we argue that even if Titan's sands are partially methane-soluble it would be more logical to assume that VIMS-blue sediments are the primary sand source.

Observations by Jaumann et al. (2008) found that VIMS-bright materials quickly disintegrate across floodplains compared to VIMS-blue sediments. Bright clasts in DISR (correlated as VIMS-bright and ISS-bright) tend to be pebble to cobble sized, while dark deposits (correlated with VIMS-blue, VIMS-brown, and ISS-dark) tend to be made of smaller pebble to sand sized clasts. Further comparisons between SAR and VIMS imagery across drainages and floodplains suggest that VIMS-bright materials may in general exist as pebble to cobble sized clasts before quickly disintegrating. Partially soluble rocks on Earth also tend to exist as larger clasts due to the larger surface area of smaller sediments, which more quickly dissolve and disintegrate (Tamrakar and Shrestha, 2008). This reflects

the steep gradient of values across VIMS-bright/VIMS-blue boundaries (Jaumann et al., 2008).

3.2 Identification of Lithostratigraphic Units

Mapped surfaces were identified as lithostratigraphic units by correlating previous interpretations of surfaces with ISS, VIMS, SAR, and DISR imagery (Fig. 7). Surfaces that appear bright in DISR also appear bright in ISS, VIMS, and SAR (with some variability in SAR). Dark values in DISR appear dark in ISS, but can appear brown, purple, or blue in VIMS, and bright or dark in SAR. VIMS-light blue surfaces appear to be generally moderate gray in DISR (likely due to greater detail), light gray to bright in ISS, and bright in SAR.

Based on material appearance in imagery, the relative locations of materials, and the spectral similarity of VIMS-blue and brown materials compared with VIMS-bright materials (Fig. 8), we conclude there are 2 primary substances compositionally, with VIMS-blue materials existing as VIMS-brown sand only because of clast size differences making slight differences in spectral signatures. These slight differences were exaggerated in VIMS imagery due to the assigned color scheme (Le Mouélic et al., 2019).

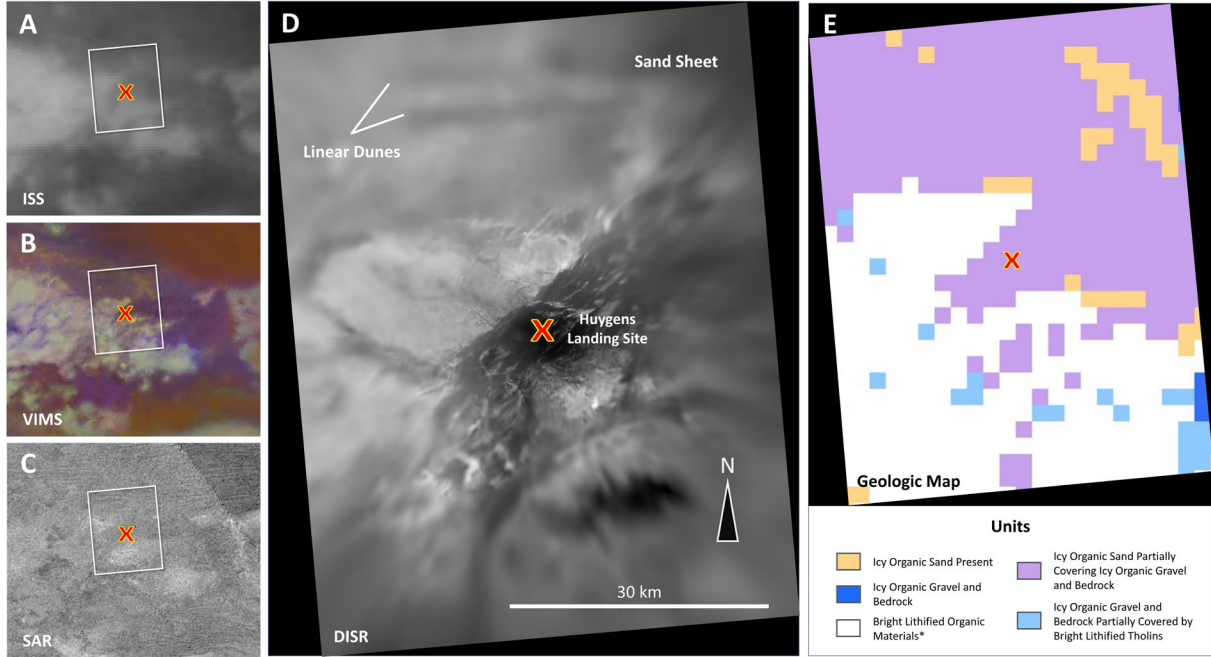


Figure 9. Region surrounding Huygens landing site in a) ISS, b) VIMS, c) SAR, d) DISR (image credit: ESA/NASA/JPL/University of Arizona/Erich Karkoschka), and e) the geologic map (Fig. 11). Notice strong correlations between DISR, which is near visible light, and ISS. According to the geologic map, the Huygens landing site is surrounded by a surface dominated by icy organic sand partially covering icy organic gravel and bedrock.

VIMS-blue and VIMS-brown materials (and consequently VIMS-purple surfaces), are made mostly of complex organic compounds with some lesser concentration of water ice (Jaumann et al., 2009; Mouelic, 2019; Soderblom et al., 2007). Relying on these spectral compositions and textural characteristics observed in SAR (Figs. 5, 6, 9), we identified VIMS-blue materials to be “icy organic gravel and bedrock,” where “icy” refers to water ice. Based on the spectral similarity between VIMS-blue and VIMS-brown, we found that VIMS-brown materials (which were mapped using 0 – 117 values in ISS and reducing the selection by the extent of 132 – 255 in VIMS green channel and VIMS-blue, light blue, and purple surfaces) are “icy organic sand.” Varying abundances of sand were given separate units as described in Section 2. Based on our interpretation that VIMS-purple is VIMS-brown dunes with VIMS-blue interdunes, we determined VIMS-purple surfaces to be “icy organic sand partially covering icy organic gravel and bedrock.” It is possible

that the greater region surrounding the Huygens landing site, which was largely mapped as icy organic sand partially covering icy organic gravel and bedrock, is generally covered with sand sheets and streaks partially concealing icy organic gravel based on observations of descent imagery (Fig. 11).

Due to Jaumann et al. (2009) and Mouelic (2019) concluding that VIMS-bright materials have greater concentrations of organic compounds, and Soderblom et al. (2007) further suggesting that VIMS-bright materials are largely lithified bright tholins, we interpreted VIMS-bright as “bright lithified organic materials.”

VIMS-light blue surfaces appear to generally be distributed as small isolated surfaces across dominantly VIMS-bright regions, or as margins surrounding VIMS-blue surfaces. It has also been interpreted that VIMS-blue materials underlie a VIMS-bright mantle (Soderblom et al., 2007; Brossier et al., 2018). Based on these observations, and VIMS-light blue regions appearing bright in SAR, we concluded that VIMS-light blue surfaces are “icy organic gravel and bedrock partially covered by bright lithified tholins.”

Due to the Huygens probe landing near a thin exposure of bright lithified organic materials that overlies exposed icy organic bedrock, it is likely that the landing imagery (Fig. 10b) represents a light purple value in VIMS if resolutions would allow. Icy organic sand, gravel, and bright lithified organic materials all appear to be present.

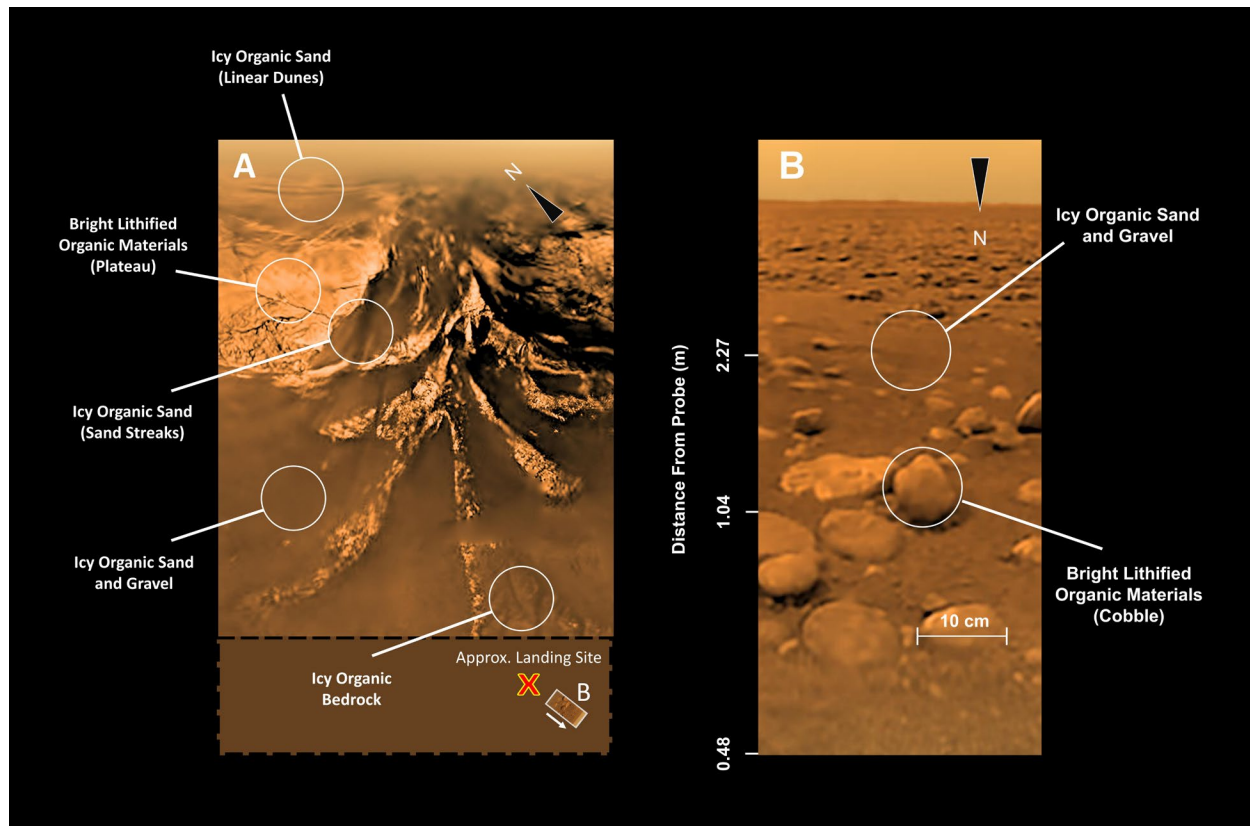


Figure 10. Enhanced DISR imagery of a) region NE of Huygens landing site with blank extension to show relative position of landing site and location of b) landing site facing south. Marked distances from probe and 10 cm scale for cobble were adapted from Keller et al. (2008). Outlined location of b) in a) is not to scale. Lithologies are labelled in their various forms that are present within imagery. Image credit: ESA/NASA/JPL/University of Arizona.

4. Map of Sand and Bedrock Distributions

We created a partial map of the equatorial regions of Titan (from roughly 40° N to 40° S) that illustrates the distributions of sand and VIMS-blue materials (Fig. 11). While there are equally detailed maps with a wider variety of units (see Lopes et al. [2020] global geologic map), this map is the first to display interpreted relative sand abundances and regions where sand is partially covering VIMS-blue materials (seen as VIMS-purple).

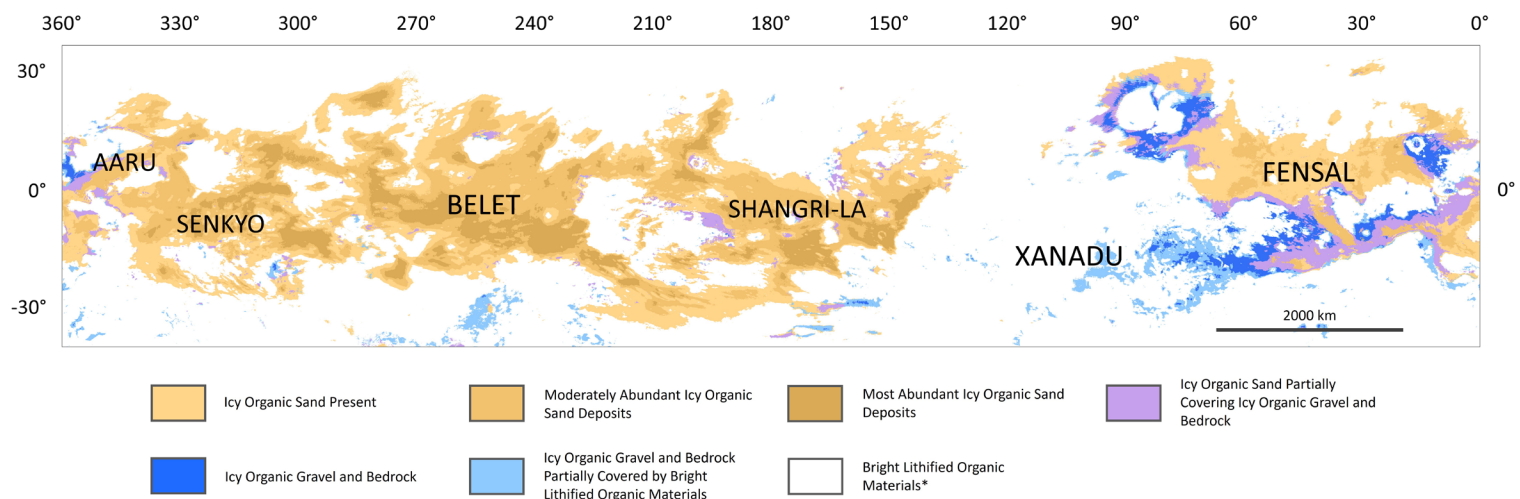


Figure 11. Global equatorial map of relative abundances of icy organic sand, icy organic gravel and bedrock, bright lithified tholins, and regions of icy organic sand partially covering icy organic gravel and bedrock, and icy organic gravel and bedrock partially covering bright lithified tholins. Color scheme is roughly based on the VIMS color scheme created by Le Mouelic et al. (2019). Relative sand abundances mapped as various shades of tan. Areas with most abundant sand are mapped as dark tan and moderately sandy areas are medium tan, both as determined by dark (0 – 47) and moderate (47 – 70) gray values in ISS. Least sandy areas are light tan and were mapped by applying a value threshold of 70 – 117 to ISS, and further restricting the selected area by the extent of 132 – 255 in the green channel of VIMS. The resulting selection was then overlain by all other selections and the remaining extent visible was interpreted as icy organic sand present. Other units were created from color selections on VIMS imagery (see Table 1). *Extent of bright lithified tholins unit was interpreted as being the remaining unmapped regions of the map and were not explicitly mapped due to strong similarities with VIMS-green.









Unit	Description	Origin of Materials	Color	
 Icy Organic Sand	Estimated to have an average grain size of 300 μm. Made mostly of complex organic compounds. Some water ice is likely present. Thin layers of tholins may accumulate onto the surface of grains over time.	Wind-swept alluvial fans, dried lakebeds, and impact ejecta containing icy organic sediments.	ISS	Light to dark gray.
			VIMS	Orange to reddish brown.
			SAR	Dark gray where visible
			Visible Light [†]	Brown
 Icy Organic Sand Present	Generally outer-most extent of sand seas where sand exists only as sand sheets. Where dunes are present, their interdunes are particularly exposed with bedrock or gravel visible.	-	ISS	Light to moderate gray
			VIMS	Orange to reddish brown.
			SAR	Often transparent. Where visible, sand appears moderate gray. Some dark gray dunes are visible with interdunes exhibiting underlying deposits
			Visible Light [†]	Brown
 Moderately Abundant Icy Organic Sand Deposits	Most common surface within the sand seas. Dunes are present with partially sand covered interdunes.	-	ISS	Moderate gray
			VIMS	Orange to reddish brown.
			SAR	Dark gray dunes with moderate to dark gray interdunes.
			Visible Light [†]	Brown
 Most Abundant Icy Organic Sand Deposits	Typically within regions upwind of large topographic obstacles or where clusters of paleolakes have created sediment sinks. Dunes tend to be closer spaced and interdunes tend to be covered with sand.	-	ISS	Dark gray
			VIMS	Orange to reddish brown.
			SAR	Dark gray
			Visible Light [†]	Brown
 Icy Organic Sand Partially Covering Icy Organic Gravel and Bedrock	Icy organic sand with exposed interdunes of icy organic pebbles.	-	ISS	Light to moderate gray
			VIMS	Dark to moderate bluish to reddish purple.
			SAR	Moderate gray, dark gray dunes visible
			Visible Light [†]	Brown
 Icy Organic Gravel and Bedrock	Mostly complex organic compounds mixed with some water ice. Interbedded with bright lithified tholin deposits. Also present as gravel within fluvial channels, alluvial fans, and gravel sheets.	Possibly sourced from a frozen upper layer of an ancient ocean. Brought to surface by large impacts and/or cryovolcanism. Interbedded with bright lithified tholins.	ISS	Light gray
			VIMS	Dark blue
			SAR	Moderate gray to bright.
			Visible Light [†]	Brown
 Icy Organic Gravel and Bedrock Partially Covered by Bright Lithified Organic Materials	Icy organic pebbles and isolated exposures of icy organic bedrock partially covered by bright lithified organic materials.	-	ISS	Bright to light gray
			VIMS	Light blue.
			SAR	Bright
			Visible Light [†]	Light Brown
 Bright Lithified Organic Materials*	Often exists as bedrock or pebble to cobble-sized clasts. Likely to have high porosity, low density, partial methane solubility, and low mechanical strength.	Deposited by airfall as tholins. Deposits may have lithified from repeated methane precipitation percolating, partially dissolving, and subsequently precipitating evaporite material as a cement.	ISS	Bright to light gray
			VIMS	Bright
			SAR	Bright where visible, somewhat transparent.
			Visible Light [†]	Nearly white, hint of brown.
*Bright lithified organic materials unit was not explicitly mapped, but interpreted based on remaining unmapped regions generally correlating VIMS-bright values.				
[†] Visible light colors are based on Huygens descent imagery, which is not entirely visible light. These colors are estimates.				

Table 2. Units from map (Fig. 11) with descriptions, interpreted origins and colors as seen in ISS, VIMS, and SAR. Probable visible light colors are also listed as interpreted from Huygens descent imagery.

The map (Fig. 11) has various limitations and errors. Low resolution imagery, particularly in an area west of Menrva Crater and north of Xanadu, was used while mapping. Accuracy is no better than 50 km in such areas. Additionally VIMS and ISS imagery have not yet been thoroughly georeferenced and consequently isolated regions appear to be shifted relative to one another. We found these discrepancies to generally be less than 20 km. Mapped boundaries have various artifacts that originated from artifacts created during the development of the VIMS mosaic. Causes for VIMS artifacts include the stitching of low resolution images, localized differences in the

atmosphere that were insufficiently compensated for, and calibration errors (Le Mouélic et al., 2019). Similar errors exist with the ISS mosaic (Porco et al., 2005). Some features (see Section 7) were unable to be mapped at this large of a scale due to their small sizes and/or subtle differences in VIMS values, but are referenced in this work due to their significance in revealing geologic processes.

The equatorial map (Fig. 11) reveals that sands are globally distributed across the equatorial regions, with the exception of Xanadu, a rugged, dissected and sand-free region (Radebaugh et al., 2009; Rodriguez et al., 2014; Monteleone et al., 2020). We measured the total sand coverage of the map region (which covers equatorial latitudes only) to be 30.5%. Out of sand covered regions the total coverage of most abundant sand, moderately abundant sand, sand present, and icy organic sand partially covering icy organic gravel and bedrock are 11.3%, 33.8%, 46.0%, and 8.9% respectively. Sand is locally interrupted by other regions that are SAR bright, rugged, and in some cases with clear peaks or mountain chains assumed to be highlands between various sand seas (Radebaugh et al., 2007; Radebaugh et al., 2010; Liu et al., 2014). Dune long axes tend to have a flow-like morphology around these landforms, further confirming their elevated nature (Lorenz and Radebaugh, 2009; Malaska et al., 2016).

Our equatorial map (Fig. 11) reveals that VIMS-blue surfaces tend to be located upwind of and adjacent to sand seas, with Xanadu as the most prominent exception. Although small and isolated, some VIMS-blue surfaces are distributed just upwind (west) of Shangri-La and Senkyo. Significant VIMS-blue surfaces are immediately upwind (west) of Fensal and Aztlan (Fig. 11). Some upwind margins of VIMS-blue surfaces are also similar in shape to downwind and adjacent margins of sand seas. This is particularly visible on the western margins of Fensal and Aztlan (Fig. 11).

1.3% of the mapped surface is covered with icy organic gravel and bedrock. If coverage of the units icy organic sand partially covering icy organic gravel and bedrock (2.7% of surface) and icy organic gravel and bedrock partially covered by bright lithified materials (2.5% of surface) are included they altogether make up 6.5%. 43.7% of the icy organic gravel and bedrock unit is within a 6,300 km long, E to W trending, linear feature that extends across southern Xanadu up to SW Aaru. Much of this ice-rich corridor is upwind (west) and adjacent to Aztlan (Griffith et al., 2019). 42.4% of the icy organic gravel and bedrock unit is associated with the Menrva and Sinlap impact craters, and 16.9% is within Xanadu. VIMS-light blue surfaces within eastern Xanadu are arranged in 2 concentric circles.

VIMS-purple surfaces tend to be distributed as narrow bands directly between VIMS-blue and VIMS-brown surfaces and along upwind margins of sand seas (Figs. 2, 11).

5. Interpreted Causes for Sand Distributions

Mapped distributions of sand obtained in this study, coupled with previous research, observations in SAR imagery, global topography, and atmospheric modeling (Larson, 2019; Tokano, 2008) suggest 5 primary causes for sand accumulation on the surface of Titan. 3 of these are related to topography: topographic obstacles, basin entrapment, and channeling within corridors. 2 involve other factors: opposing wind currents and fluvial margins.

5.1 Influence of Topography on Sand Accumulation

Topography can cause obstruction of sand movement, as observed in sand seas on Earth (Lancaster, 1995; Wilson, 1971). Eastern Fensal appears to be obstructed by the outer slopes of ejecta from the Sinlap impact crater. Some of the most abundant sand deposits of Fensal are located along the upwind margin of Sinlap's ejecta rim.

There is some variability in sand abundance between sand seas. Coverage of most abundant icy organic sand deposits across Belet is relatively high (20.3%), and is low across Fensal (0.1%) and Aztlan (0%). There are large sandy SAR-dark and ISS-dark regions across Belet, and it appears very little bedrock protrudes through the interior of the sand sea. This may be due to Belet occupying a relative lowland (Fig. 12). Within Fensal and Aztlan there is a greater abundance of underlying SAR-bright terrain and bedrock, indicating larger sand-poor regions at the surface. These sand seas have relatively higher elevations (Fig. 12). Furthermore, Fensal and Aztlan are downwind of Xanadu, which may preclude the movement of sand from the west and cause lower sand abundances in those sand seas (Barnes et al., 2015).

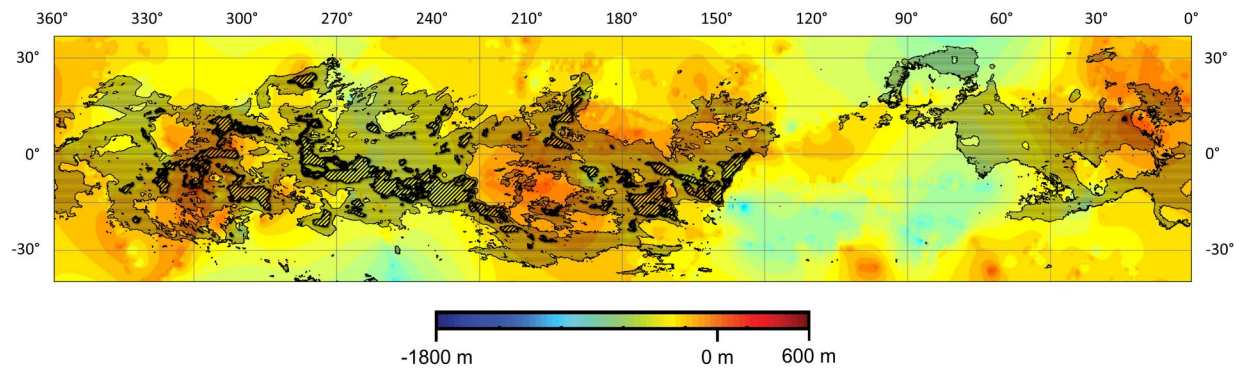


Figure 12. Global topographic map of Titan by Lorenz et al. (2013) overlain by sand sea margins (filled with fine horizontal lines) and most abundant icy organic sand deposits (filled with thick diagonal lines). Equatorial lowlands roughly correlate with abundant sand deposits, primarily in the case of Belet.

The most abundant sand deposits tend to be in the eastern areas of sand seas (Fig. 12). Although most of the abundant sand deposits within Belet are in the sand sea's southern region, there is apparent displacement to the east relative to the sand sea's boundaries. Abundant sand deposits extend across the center of a narrow corridor running from western to eastern Shangri-La and merge with a broad deposit of abundant sand along the eastern boundary of the sand sea (Fig. 12). Sand deposits become gradually less abundant toward the NE of Shangri-La.

Lakebeds, riverbeds, and land adjacent to oceans are places that trap sand within sand seas on Earth (Lancaster, 1995; Bubenzer et al., 2020). Given there is methane rainfall on Titan, even at equatorial latitudes, there may be the possibility of similar sand entrapment on Titan. SAR-dark lobate features similar to other identified lakebeds (Moore and Howard, 2010) were observed across southern regions of Belet. Dunes within them were more closely spaced and interdunes were generally darker in SAR than those across surrounding regions of the sand sea. These interpreted lakebeds were also within a broad region mapped as having abundant sand de-posits.

Notable isolated regions mapped as having most abundant icy organic sand deposits that are correlated with isolated depressions are at $(-4^{\circ}, 190^{\circ})$ within central Shangri-La roughly 750 m lower in elevation than surrounding topography, and at $(-15^{\circ}, 300^{\circ})$ within Senkyo roughly 375 m below surrounding elevations (Fig. 12).

Sand is often transported across sand seas along pathways between highlands, as can be seen across the Sahara Desert described by Lancaster (1995). On Titan in Shangri-La, a narrow W to E trending part of the sand sea at $(-7^{\circ}, 165^{\circ})$ is covered by thick sand deposits and is bounded to the north and south by what appear to be highlands in SAR. Supporting evidence for this is found in the topographic map Fig. 12. As the dominant wind direction is also W to E, we interpreted this narrow part of Shangri-La to be a sand corridor similar to those on Earth.

5.2 Opposing Wind Currents Causing Sand Accumulation

Opposing wind currents are known to affect sand accumulation on Earth. There is some evidence that opposing wind currents affect the southern margin of the Rub' al Khali (Amin and Seif, 2019). Similar processes may control sand sea boundaries on Titan.

Atmospheric modeling suggests that opposing wind currents collide over the recessed SE margin of Shangri-La (Larson, 2019; Tokano, 2008). Abundant sand deposits along this margin

(Fig. 13) may have accumulated because of this possible opposing wind current. The SE margin of Shangri-La is also recessed towards the west compared to the more northern sand sea margins. The region is adjacent to the SAR, VIMS, and ISS-bright Xanadu terrain (Fig. 2), which is dominantly low in elevation (Fig. 12). Previous research concluded that an ephemeral river must flow along the SE margin because of a similar appearance with the Namib Sand Sea and its northern margin, which is strongly influenced by the Tsondab River (Barnes et al., 2015).

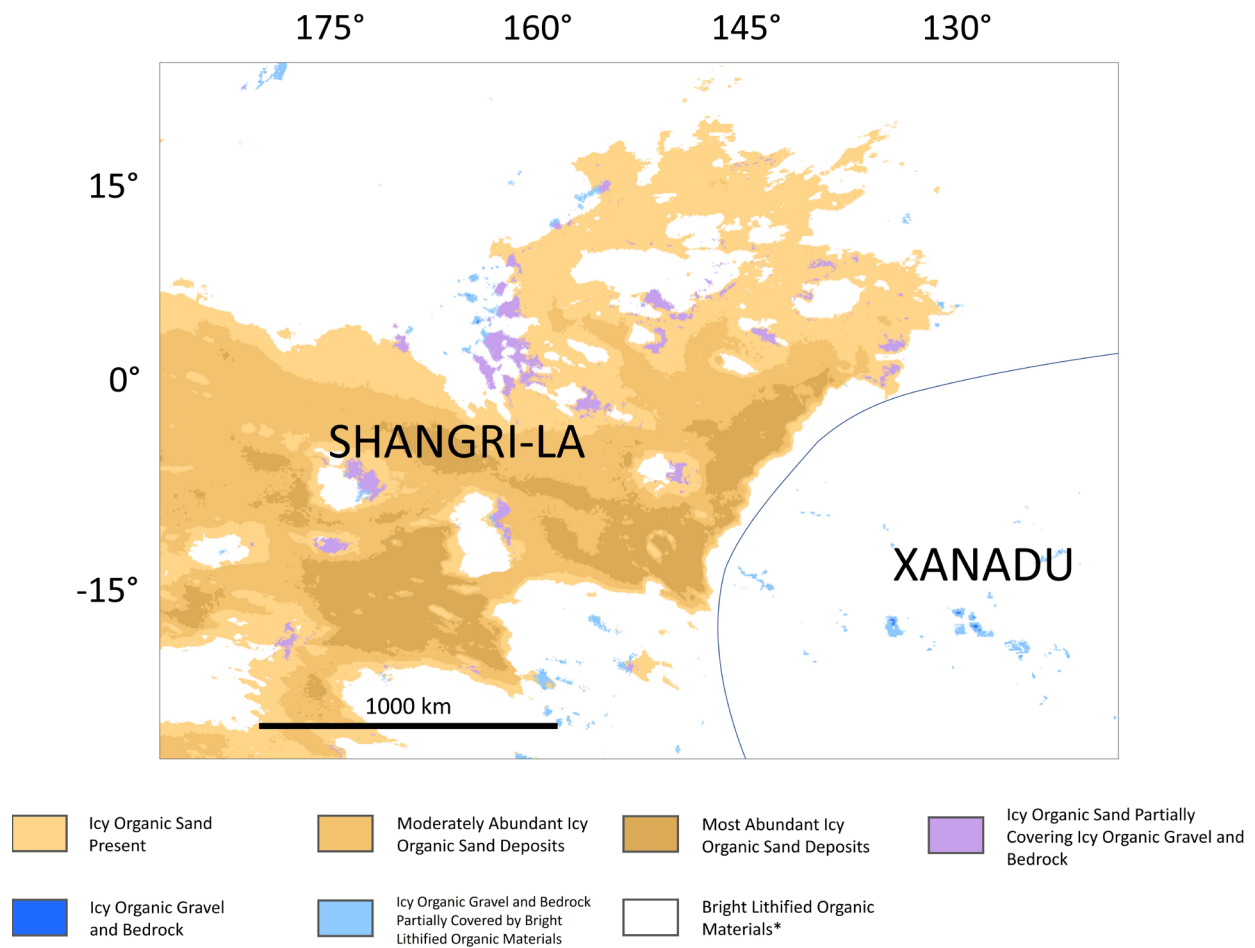


Figure 13. Geologic map centered on eastern Shangri-La. Note the significant coverage of abundant sand along the SE margin of the sand sea, consistent with a dominantly W to E wind direction and some form of obstruction along the eastern margin. Note also the recessed SE boundary where the sand sea abuts Xanadu, which occupies bottom right of figure.

We note that the regional slope of the SE margin of Shangri-La is oriented SE (Fig. 14), which would cause the proposed channel to be flowing perpendicular to regional slope for more than 600 km. Although smaller examples of this are observed on Earth, they are caused by deep canyons that prevent the channels from avulsing, or re-routing toward the regional slope. While SAR resolutions are low (0.5 km/pixel), a prominent canyon would likely be visible in SAR if it were present because nearby channels are easily seen. Additionally, if a methane river was flowing along the downwind margin of Shangri-La, sand would likely be blown into and transported by the river to a distal alluvial fan (Barnes et al., 2015). Available VIMS imagery does not show evidence of dune-like organic sediment, or a fan near the terminus of a possible drainage.

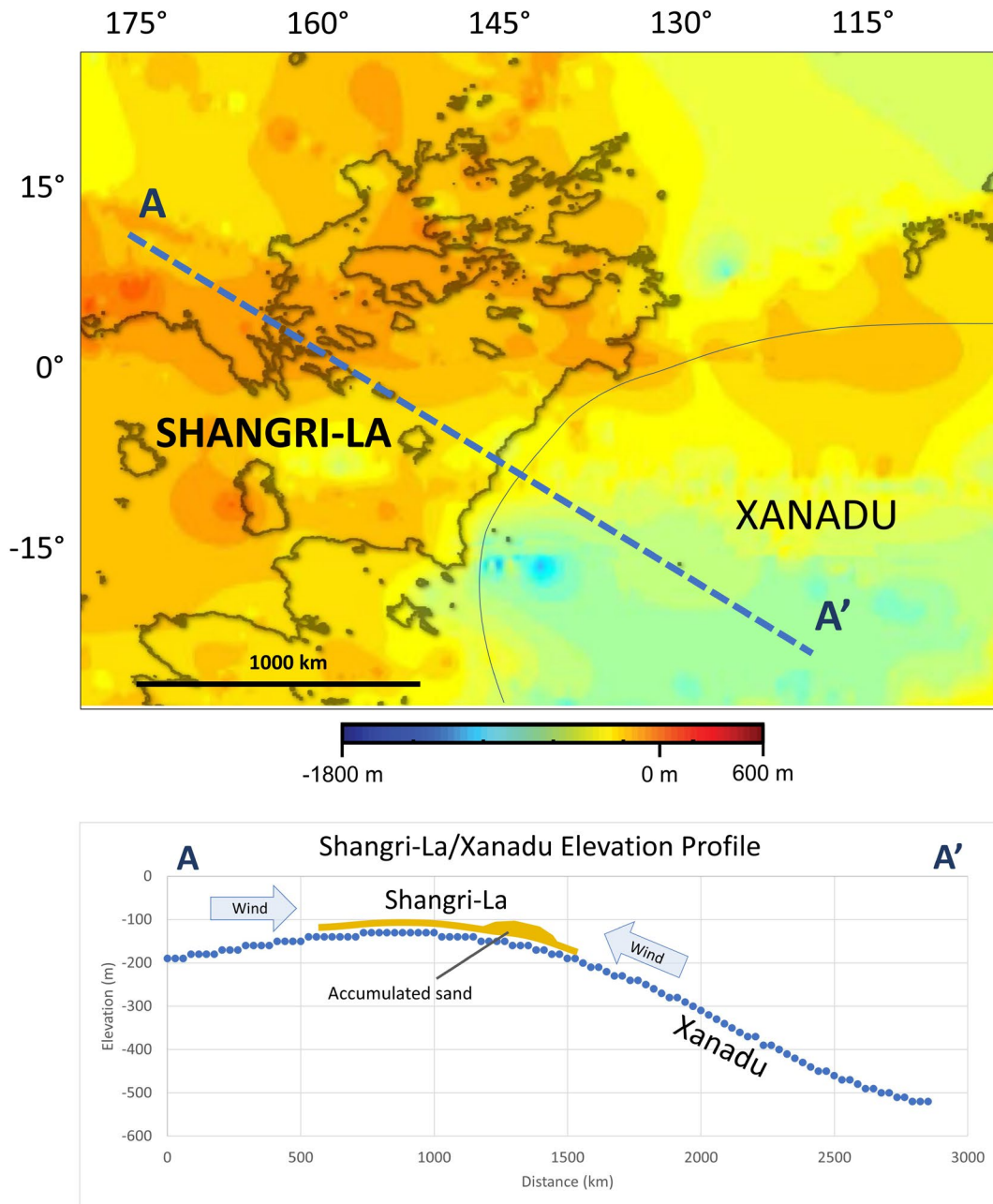


Figure 14. a) Topographic map of Titan (Lorenz et al., 2013) cropped and centered on eastern Shangri-La (outlined) and western Xanadu. Transect A – A' is oriented parallel to linear dune crests at the center of the SE margin of Shangri-La. b) Topographic profile A – A' across Shangri-La and Xanadu. Profile was created from data provided by Titan Trek at trek.nasa.gov/titan. Notice sand sea margin ends at a regional downhill slope.

Dune crests splay outwards towards the northeast at the northern extent of the recessed boundary, and towards the southeast at the southern end of the recessed boundary. These dune

long axis orientations are consistent with shaping by an opposing (westward) wind current emanating from Xanadu. Similarly, dune crests appear deflected along the southern margin of the Arabian Rub' al Khali sand sea (Fig. 15a). This region is largely influenced by seasonal, northeasterly winds that oppose the dominant sand-bearing, southwestern winds that cover much of the interior of the sand sea (Fig. 16a). Linear dune crests angle southward across the eastern extent of the southern margin. Dune crests are oriented towards the west along the central and western parts of the southern margin.

Dune morphologies along the southern margin of the Rub' al Khali sand sea provide further evidence for obstruction from opposing winds. Progressing from the interior of the sand sea towards the margins, there are linear dunes, then complex linear dunes overprinted by other dune types, sinuous “wiggly” dunes with an overall shape like linear dunes, but appear to be connected star dunes, then fully disjointed star dunes at the edge where the winds nearly equally converge (Fig. 15a).

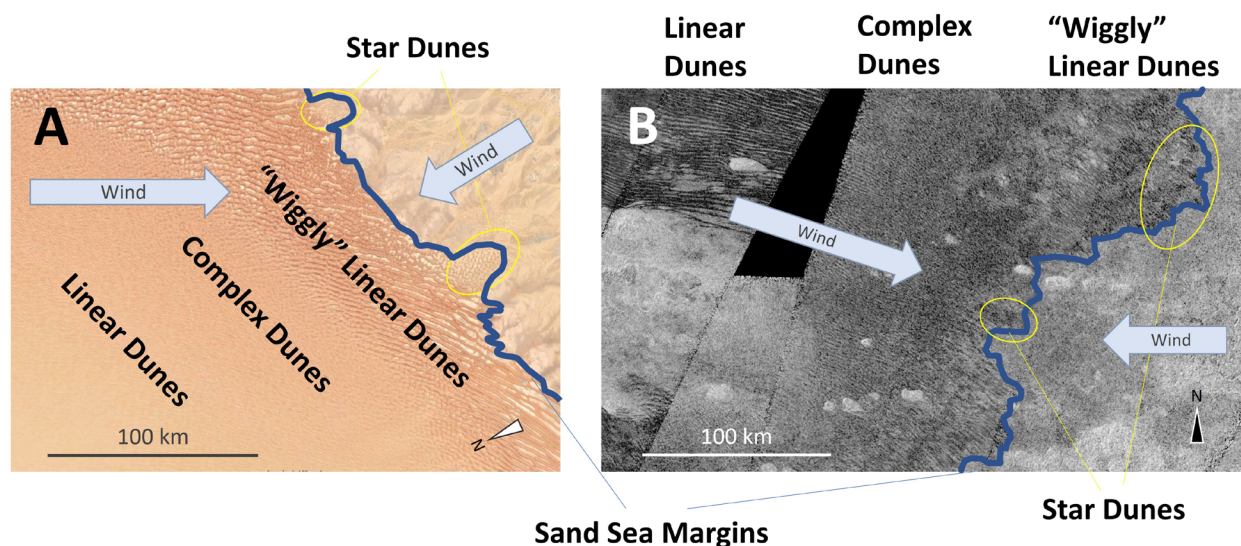


Figure 15. a) Dunes at the southern margin of the Rub' al Khali Sand Sea (from Google Earth imagery) and b) the southeastern margin of Shangri-La (SAR). Notice comparable patterns in dune morphology and sand sea margins.

Minor isolated topographic obstacles are observed near the SE margin of Shangri-La (observed as isolated SAR-bright features (Fig. 15b)), and across topographic profiles (Fig. 14b). Similarly, an isolated section along the southern margin of the Rub' al Khali interacts with inclined topography (Fig. 16b); however, the gradient in slope is comparable to un-obstructing slopes within the center of the sand sea. Both sets of topographic obstacles appear to be minor compared to other topographic anomalies within the sand seas and are minor compared to the scale of the margins themselves.

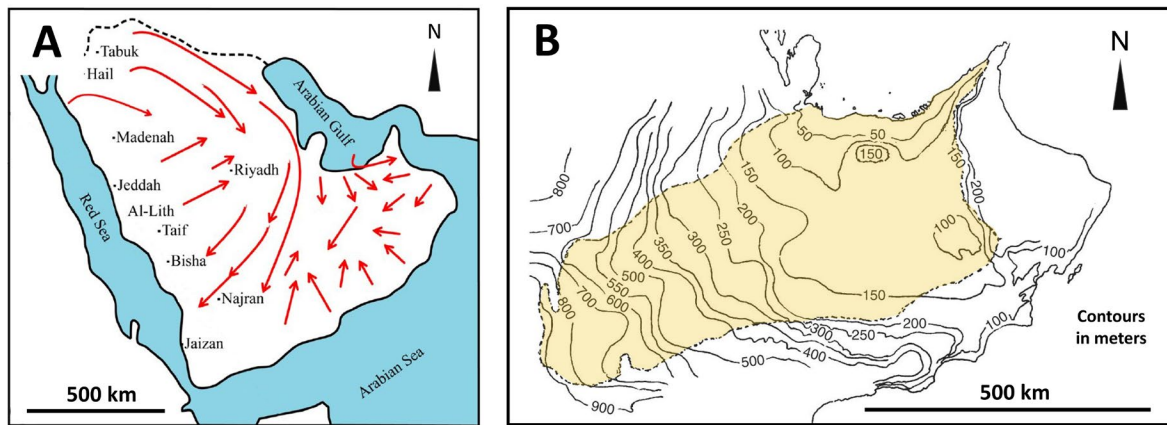


Figure 16. a) Dominant wind directions as mapped from orientations of barchan dunes (Amin and Seif, 2019). b) Topographic map of the Rub' al Khali Desert. Contour intervals are in meters. Dashed line outlines the margin of the Rub' al Khali Sand Sea, colored tan. Notice the southern sand sea margin's independence from slope gradient and the relatively steep gradients found within the center of the sand sea where the sand migrated unobstructed (2006).

Computer modelling of atmospheric currents above Xanadu conducted by Larson (2019) modeled Xanadu as a large depression and revealed that W to E, sand-bearing wind currents may be deflected along the western margin of Xanadu by eddy currents across Xanadu and are forced to flow towards the NE (Fig. 17). Although there is a striking resemblance between these model results and the overall orientations of observed dune crests in the NE of Shangri La, we propose that there may be additional forces that generate more directly opposing wind currents across the SE margin of Shangri-La. Dune crests there are oriented perpendicular to the modeled wind

directions. RADAR brightness temperatures (a combination of real temperature and emissivity, which are related to material properties), are 20° C colder across much of central Xanadu than SE Shangri-La (Janssen et al., 2016; Fig. 18). This is likely partially due to the relatively high albedo of Xanadu (Solomonidou et al., 2014). Such a temperature gradient may generate katabatic, or cold density-driven, winds across Xanadu (Radebaugh et al., 2011). These katabatic winds may flow for a distance up the gradual slope at the SE boundary of Shangri-La, where they would collide with westerly, sand-bearing winds. These opposing winds would likely promote the accumulation of abundant sand deposits near the SE boundary of Shangri-La because of the reduction in velocity of the sand-bearing current. The influence of a strong gradient in surface temperatures may also be responsible for the deflected SE oriented dune crests at the southern end of the recessed sand sea margin.

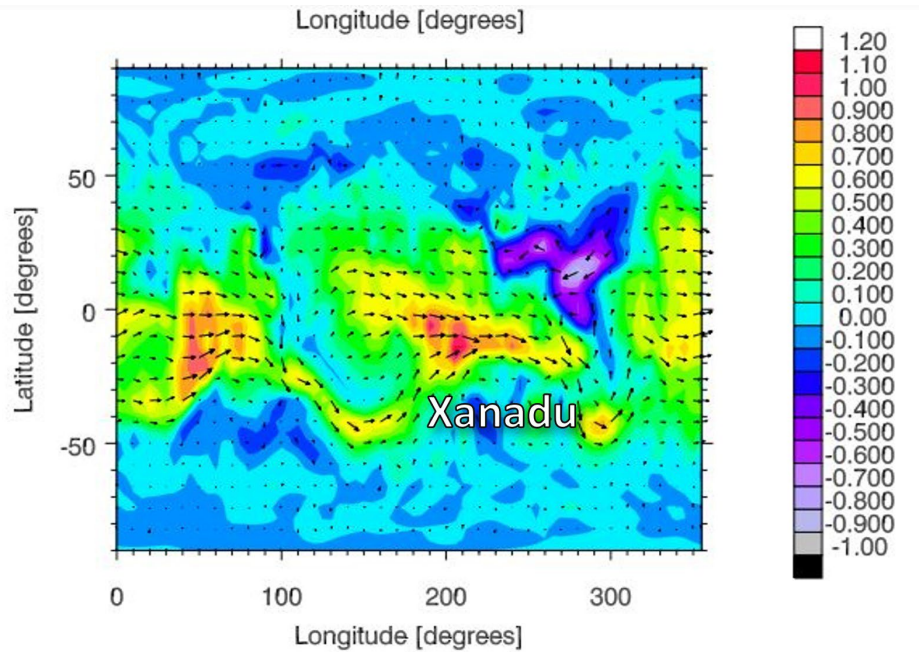


Figure 17. Modeled wind vectors with colors representing W to E vector magnitude (Larson, 2019). Xanadu may behave as an atmospheric eddy and deflect westerly winds to the NE preventing sand-bearing winds from passing directly across its surface.

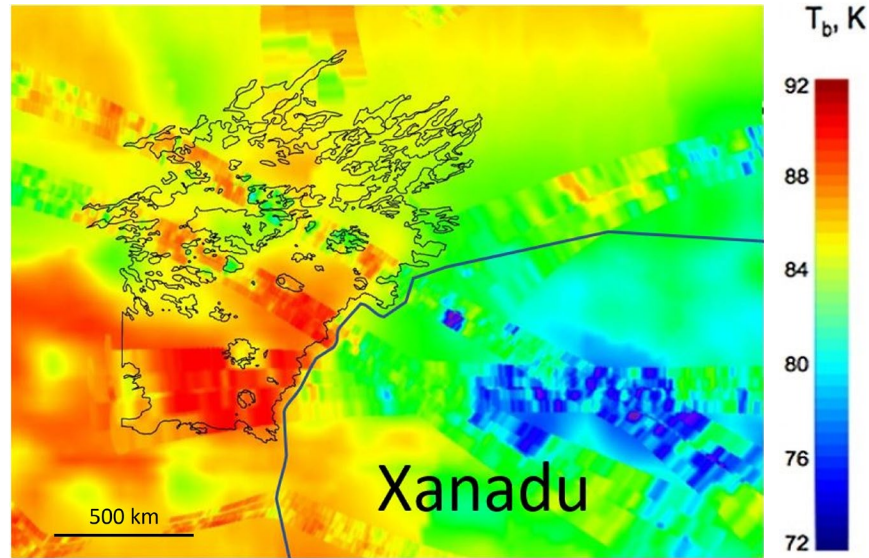


Figure 18. RADAR brightness temperature map of Titan. Eastern Shangri-La outlined (completed by hand tracing around dark values in ISS imagery). Xanadu is cold (Janssen et al., 2016).

Studies of topography and winds on Mars (Chojnacki et al., 2019) revealed that wind currents generated by differences in albedo can have a strong influence on sand migration. A difference in normal albedo of 0.1 between two Martian landmasses is associated with winds that transported sand 2 km upwards in elevation over a horizontal distance of 200 km on Mars (Chojnacki et al. 2019; Fig. 19). In Titan's thicker atmosphere with greater heat capacity, the roughly 0.2 difference in normal albedo between Shangri-La and central Xanadu (Solomonidou et al., 2014) may create similar influences on sand flux.

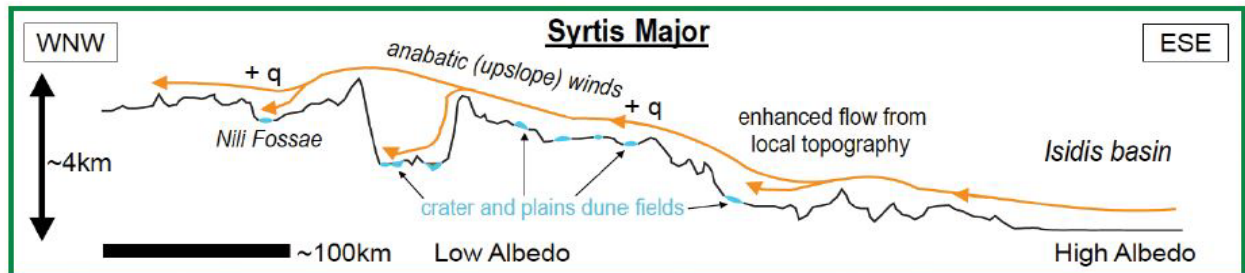


Figure 19. Topographic profile of Syrtis Major with primary wind directions indicated by orange arrows. (Chojnacki et al., 2019).

In summary, we propose an alternative explanation for the recessed SE boundary of Shangri-La in which a combination of gyroscopic and katabatic winds are generated by the surface of Xanadu due to its high albedo, relatively cooler temperature, and being a broad depression. These generated winds across western Xanadu flow toward the west and oppose sand-bearing winds at the boundary between Shangri La and Xanadu, leading to obstruction of sand movement and dune progression into Xanadu. We also acknowledge that localized topographic obstacles are partially responsible for sand obstruction.

5.3 Influences of Fluvial Margins on Sand Distribution

River channels can obstruct sand migration on Earth, causing downwind margins to be abrupt. For example, the Namib Sand Sea is bordered by the Tsondab River, which precludes movement of sand to the north (Lancaster, 1995). In order to better understand the effects fluvial activity can have on sand sea margins, we compared observations of Titan SAR imagery with GPR and GPS surveys of the Kelso Dunes in California, USA.

5.3.1 Surveying Kelso Dunes, CA as a Terrestrial Analog

5.3.1.1 Geologic History

The Kelso Dunes were chosen as a terrestrial analog for this study because of the presence of linear dunes similar to those observed on Titan, a high abundance of sand, and interactions with topographic and fluvial landforms at the dune field margins. SAR imagery suggests that river channels may also interact with sand seas on Titan.

The Kelso Dunes originated from wind-blown sediment from the Mojave River. Additional sediment has also been introduced from adjacent alluvial fans to the south and east of the dune field (from the Granite and Providence Mountains respectively), and Budweiser Wash to the west. The dune field likely formed 25,000 years ago. Linear dunes developed and were later overprinted

by transverse dunes. Outer regions, particularly across the eastern extent of the dune field, have become stabilized and are currently inactive (Muhs et al., 2017).

Cottonwood Wash, an ephemeral river, flows through the dune field roughly S to N in a perpendicular orientation to the crests of the linear dunes. This channel separates an active region of the dune field from a largely inactive region to the east (Muhs et al., 2017). Under current conditions, sand is unable to be transported by saltation across the steep channel walls. It can be assumed that previously when either there was a greater sediment supply or the climate was drier, the sand migrated across the dune field without obstruction.

5.3.1.2 Research Design

We surveyed across the Kelso Dunes' eastern and southern margins (Fig. 20) to determine how fluvial activity influences sand thickness along the dune field's margins, and ultimately how fluvial activity affects the migration of sand within the dune field. Participants of the survey were Benjamin Dean Lake (primary author), Jani Radebaugh (thesis committee chairperson), and Cheyenne Pratt (fellow BYU geology graduate student). We chose to make 2 transects across the eastern margin; one across a margin that directly contacts the Cottonwood Wash (which is roughly oriented perpendicular to the dominant wind direction) and another to the south that crosses a margin not in contact with Cottonwood Wash. A third transect was conducted across the southern margin where another river channel directly contacts the dune field. This third location was chosen as the channel there is oriented roughly parallel with the dominant wind direction.

We used a 200 MHz GPR antenna attached to a bistatic GSSI SIR 4000 controller. A dielectric constant of 5 was used due to the significant amount of quartz present in the sand (Martinez and Byrnes, 2002). We set the controller to 1024 samples per scan, 19.7 scans/meter, and a recording time of 150 ns. A GPS unit was used to compensate for topography.

GPR data was processed by applying exponential gain correction, automatic gain control, surface correction to ground surface, and a “background removal” filter to remove the direct arrival.

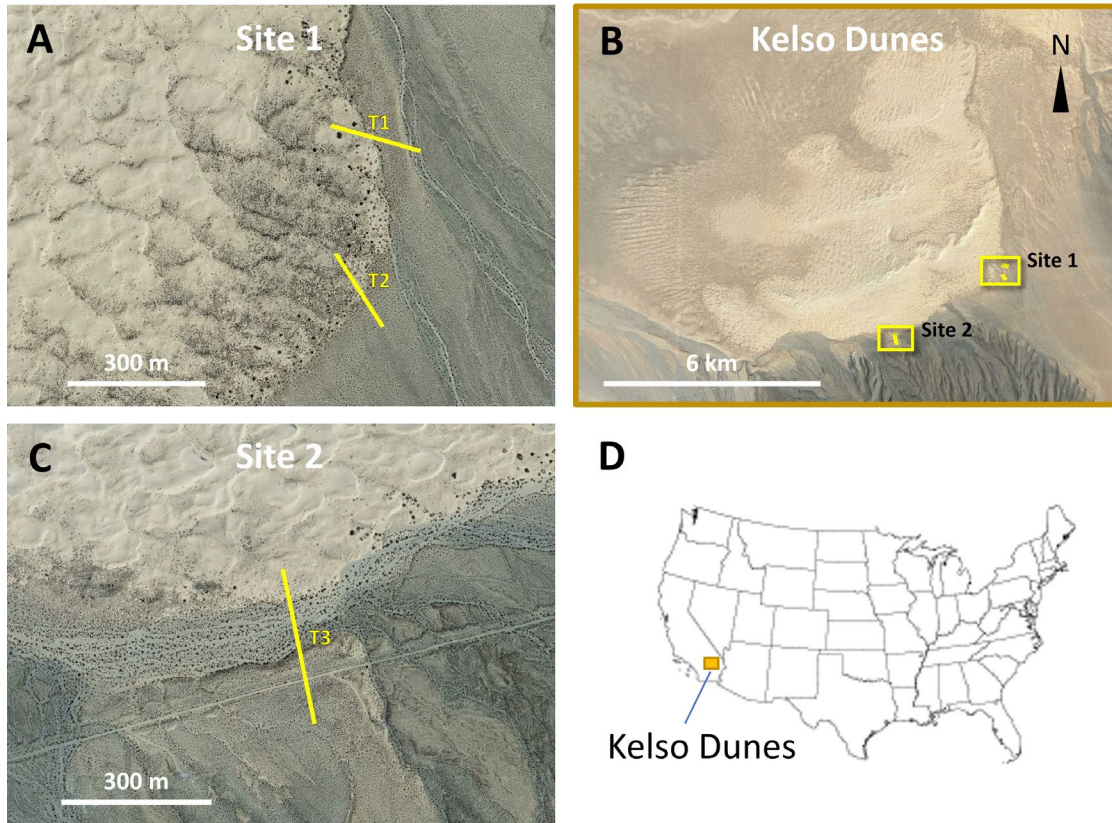


Figure 20. Google Earth imagery with approximate locations of surveyed transects T1, T2, and T3 annotated as yellow lines. a) Site 1 with T1 and T2, c) Site 2 with T3. b) Google Earth imagery of the Kelso Dunes with survey sites labelled as yellow boxes. d) Locator map showing location of Kelso Dunes within the United States.

5.3.2 Results From Surveys and Comparisons with Titan’s Dunes

Processed GPR profiles (Fig. 21) from our surveys at the Kelso Dunes show some cross-bedding within dunes and gradually dipping reflections we interpreted as the lower contact of the dune sand. Because the GPR controller had a malfunction after surveying the eastern margin of the Kelso Dunes, we were only able to conduct a GPS survey across T3 at the southern margin. It

is likely that the depth range of interpretable reflections was reduced due to the presence of ground-water from a rainstorm that covered the area before we arrived to conduct the survey.

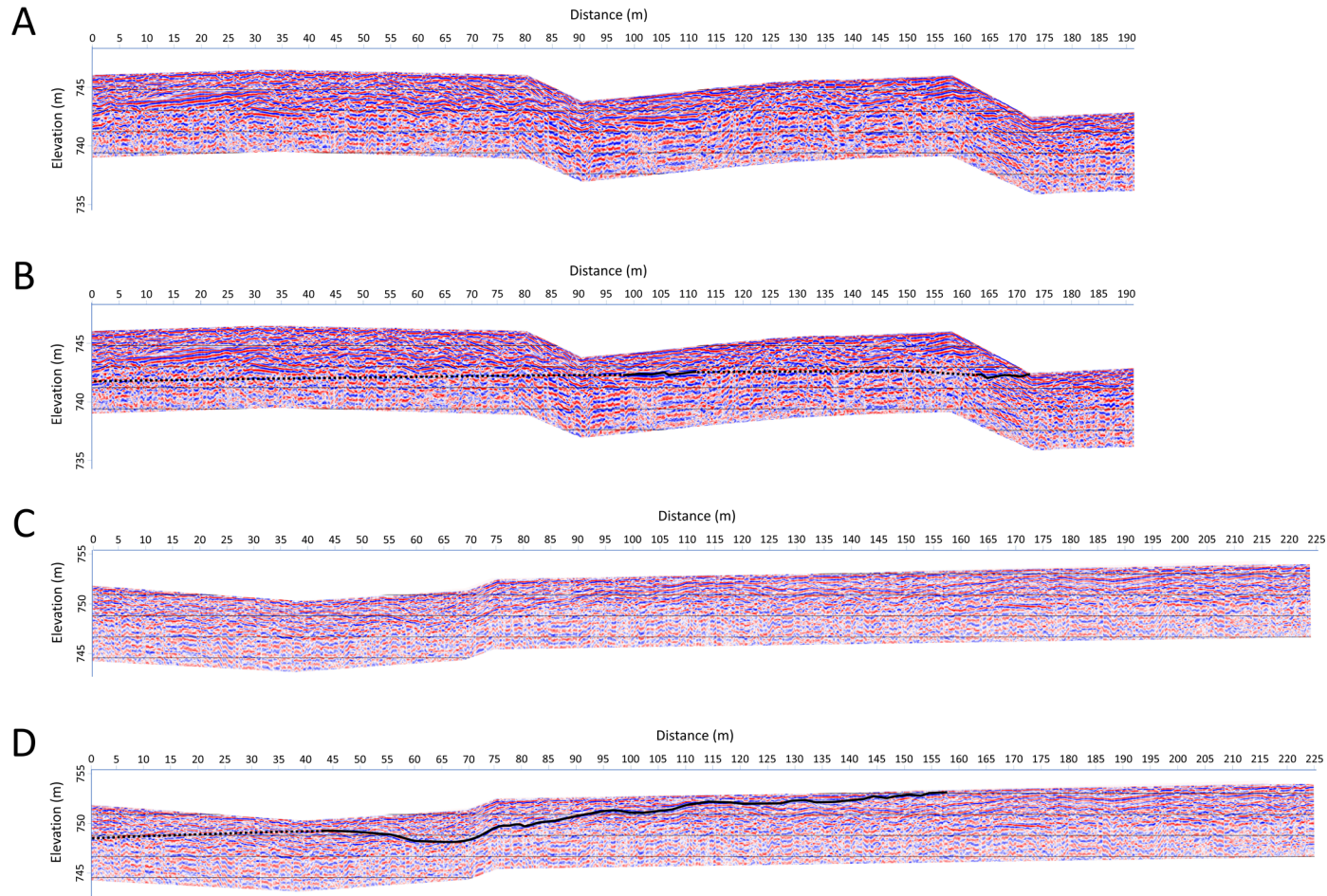


Figure 21. GPR surveys of T1 (a, b) and T2 (c, d) across margins of the Kelso Dunes. T1 crosses a margin that directly contacts Cottonwood Wash. T2 crosses a margin that has no to very little fluvial interaction. a) and c) are uninterpreted GPR profiles, b) and d) have interpreted lower contacts of dune sand represented by black lines. Bold lines have greater confidence, dashed have low confidence.

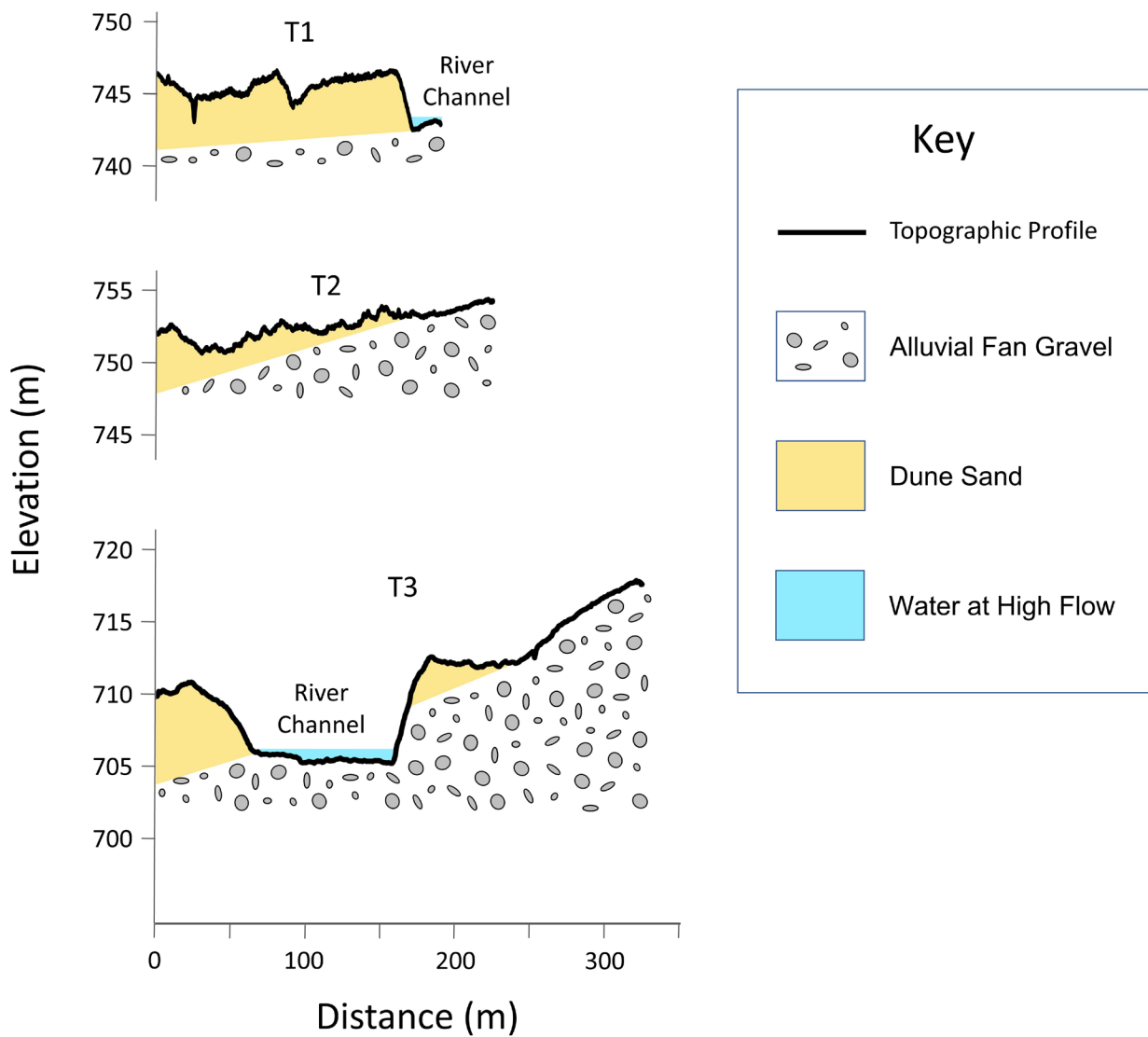


Figure 22. Annotated topographic profiles T1, T2, and T3 across margins of the Kelso Dunes sourced from GPS surveys. See Fig. 20 for locations. Extent of alluvial fan gravel, dune sand, and water at high flow were interpreted from field observations. Profiles are vertically exaggerated.

Based on the elevation profiles (Fig. 22), interpreted lower contacts of the dune field from GPR profiles (Fig. 21), and field observations, the dune field likely has depths of several meters within its interior and quickly thins out to 0 m at Cottonwood Wash. Consequently, we support previous findings (Barnes et al., 2015; Lancaster, 1995) that ephemeral rivers can obstruct migrating sand. The elevation profile of T3 appears similar to T1 and indicate similar influences of fluvial activity on the dunefield margins. Although T1 did not cross the entire Cottonwood Wash, we did observe a similar steep slope of sand on its opposite side towards the eastern half of the dune field. Due to sand existing on both sides of the Cottonwood Wash and the channel that crossed T3, we further conclude that although ephemeral rivers obstruct migrating sand, the channels must be sufficiently active for the sand flux in a given region.

We observed in SAR imagery of Titan small, isolated, and relatively SAR-bright regions that lack dunes downwind of fluvial channels within Fensal, Forseti Crater, and Belet (Figs. 23a, b, c). We interpret these channels to be where sand migration is obstructed by ephemeral fluvial activity. A fluvial channel within Shangri-La was also observed (Fig. 23d), however no downwind SAR-bright region was found.

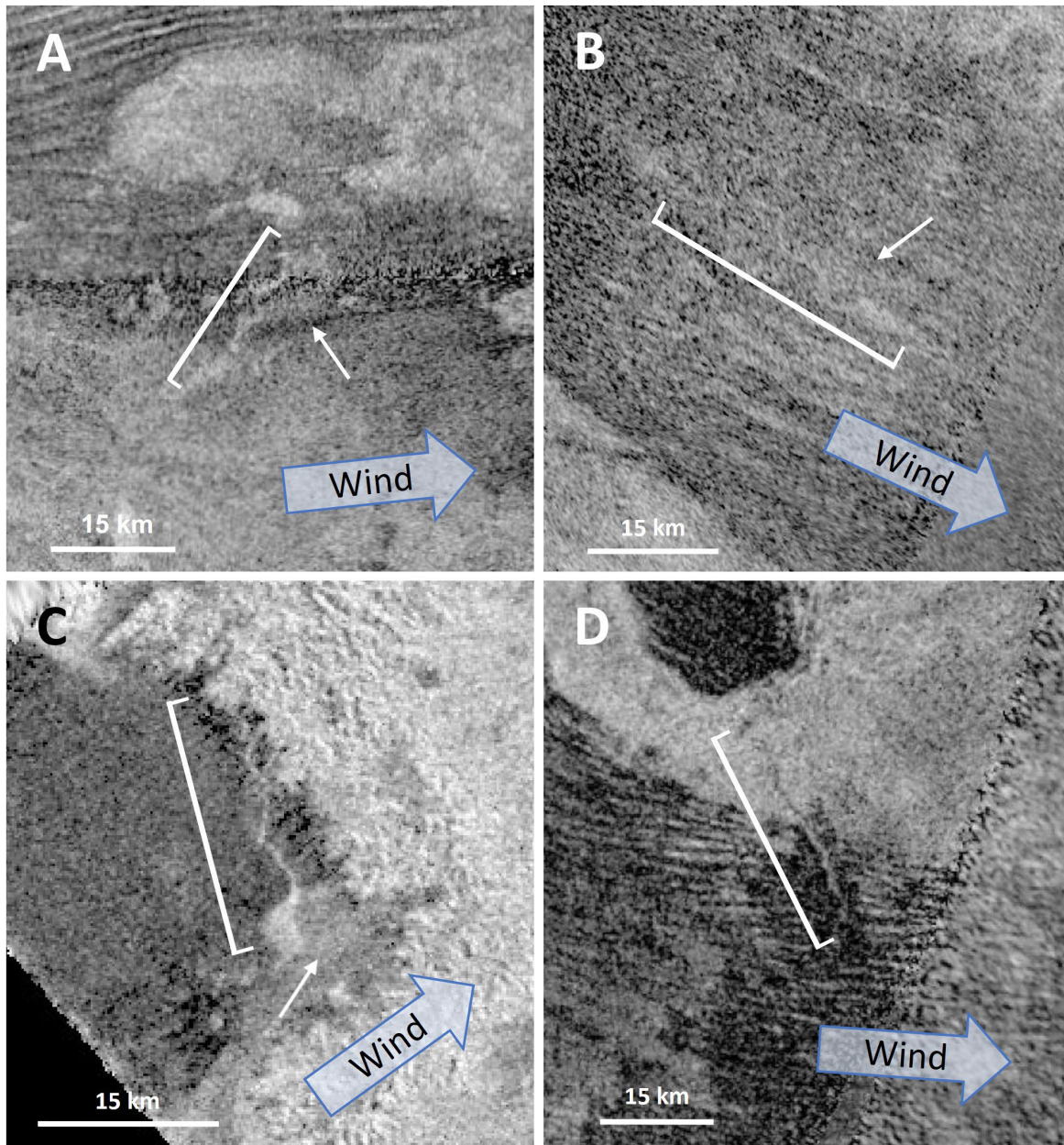


Figure 23. Fluvial channels (see white brackets) within sand seas and dune fields observed in SAR. Arrows indicate SAR bright regions downwind of channel meanders that may be sand poor due to fluvial activity removing migrating sand that enters the channels. Channels are located within a) Belet, b) southern sand corridor within Fensal near Aztlán, c) eastern crater floor of Forseti, d) southern ejecta of impact crater within Santorini and eastern Shangri-La.

Further comparisons with the Namib Sand Sea indicates a balance between fluvial and aeolian processes. Along the northern most downwind extent of the Namib Sand Sea, sand is able to cross the Kuiseb River near the coast where winds are stronger than further inland (Lancaster,

1985). The rate of sand migration near the coast is great enough to transport sand across the channel before it becomes active. Further inland where wind speeds are generally slower, sand enters the Kuiseb River channel and is transported by the river when it is active.

In the case of Kelso Dunes, it is most likely that the sediment supply has been reduced (the dune sand is mostly sourced from the Mojave River, which is no longer perennially active). The reduction of sediment supply has allowed for the ephemeral Cottonwood Wash to obstruct the migration of sand from the largely active western half of the dune field from the mostly inactive eastern half.

Overall, channels observed on Titan in SAR (Fig. 23) appear to generally cause little to no obstruction to sand migration, as linear dunes appear along upwind channel margins and at most 10 km downwind of all channels (with a possible exception of the site near the crater wall of Forseti). As SAR imagery is of the near surface, and the equatorial latitudes of Titan are thought to be drier than they were previously (Lorenz et al., 2013, Birch et al., 2016), it is possible that the interpreted channels are currently inactive and buried. We conclude that fluvial activity appears to have only temporarily obstructed sand migration on Titan, and that the current dry climate across equatorial latitudes is promoting aeolian forces to dominate the transportation of sand.

6. Exposed Rift of Exposed Icy Organic Bedrock as a Regional Sand Source

Several icy moons in the outer solar system have large rifts that have been attributed to thickening lithospheres due to a greater volume the ices occupy when frozen (Collins et al., 2009; Rudolph, M. L., et al., 2022; Steinbrügge, G., et al., 2020). Computer modeling revealed that Titan's lithosphere likely thickened significantly 500 m.y. ago from 15 km to 100 km thick (Tobie et al., 2006). Lopes et al. (2010) similarly found from crater surveys that the lithosphere

significantly thickened somewhere between 1.0 - 0.5 billion years ago. Such a substantial thickening of the lithosphere would likely exert extensional forces on the upper lithosphere and cause rifting on Titan's surface. We interpret the linear VIMS-blue feature adjacent to Aztlan to be a rift similar to those observed on many other icy moons in the solar system.

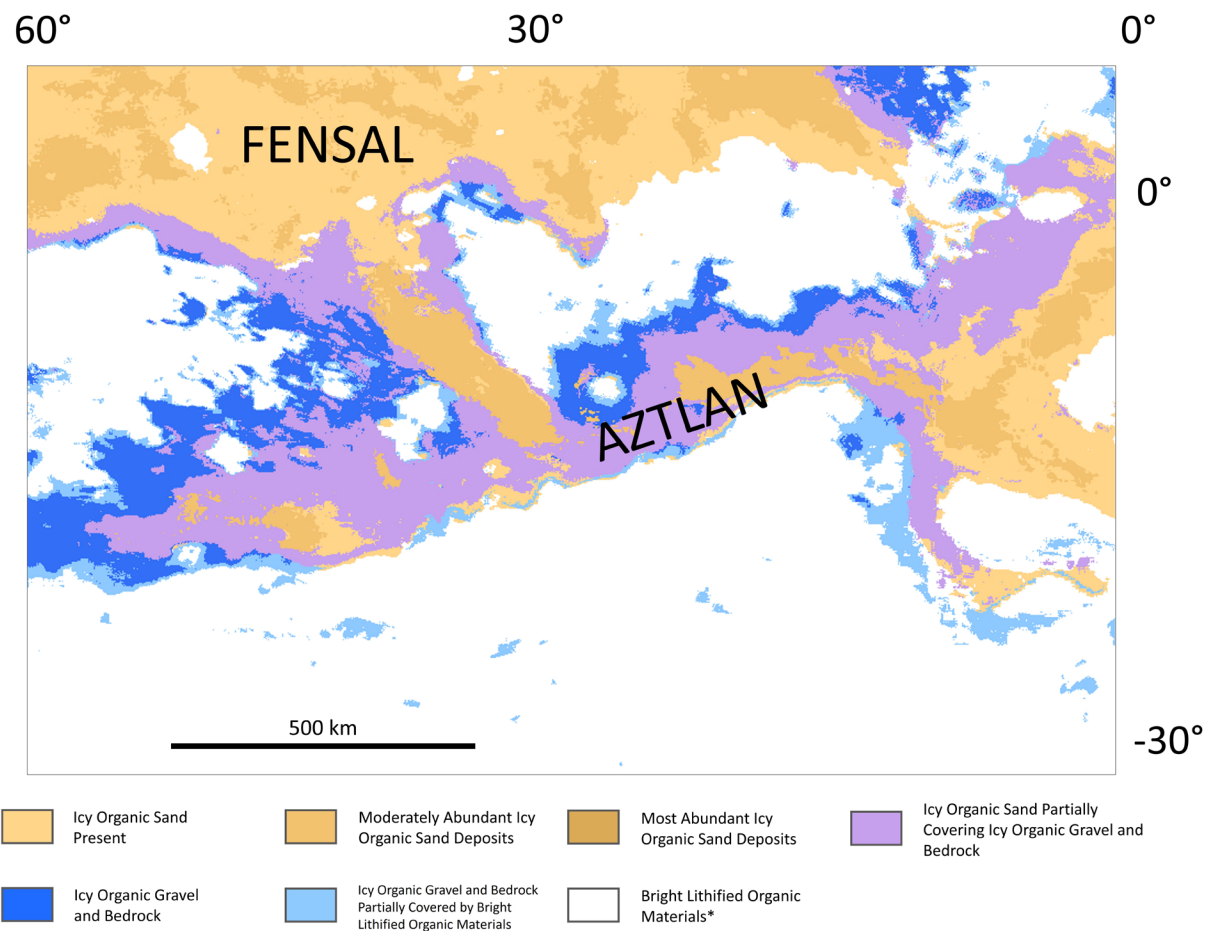


Figure 24. A closeup of Fig. 11 showing Fensal and Aztlan sand sea deposits (in tans), the VIMS-blue deposits upwind and adjacent to the sand seas, and a narrow band of VIMS-purple interpreted to be deposits of sand that partially cover underlying VIMS-blue.

Doom Mons (a probable cryovolcano) and its associated features Sotra Patera (a large deep depression thought to be a caldera), and Mohini Fluctus (a lobate SAR-bright feature interpreted to be a cryovolcanic flow from Doom Mons) are the among the most convincing cryovolcanic landforms identified on Titan's surface (Lopes et al., 2013). All of these features are all located

along the interpreted rift (Fig. 25c). Volcanism and cryovolcanism near linear features across the solar system are often associated with tectonic rifting (Collins et al., 2009; Ruggieri, 2018). Cryovolcanism from rifting induced by thickening of an icy lithosphere has previously been modeled by Manga and Wang (2007). We also interpreted from SAR imagery within the proposed rift a cluster of three, 5 – 10 km. wide, gradually sloped inselbergs (assumed by the relatively subtle amounts of dune obstruction) with vent-like features at their summits (Fig. 25b). We found these features to be similar in overall appearance to Sapas Mons (a large shield volcano on Venus) in SAR (Fig. 25a). Although the scale of these features are different they are all roughly circular and SAR-bright, and most appear to have 2 vents at their summits.

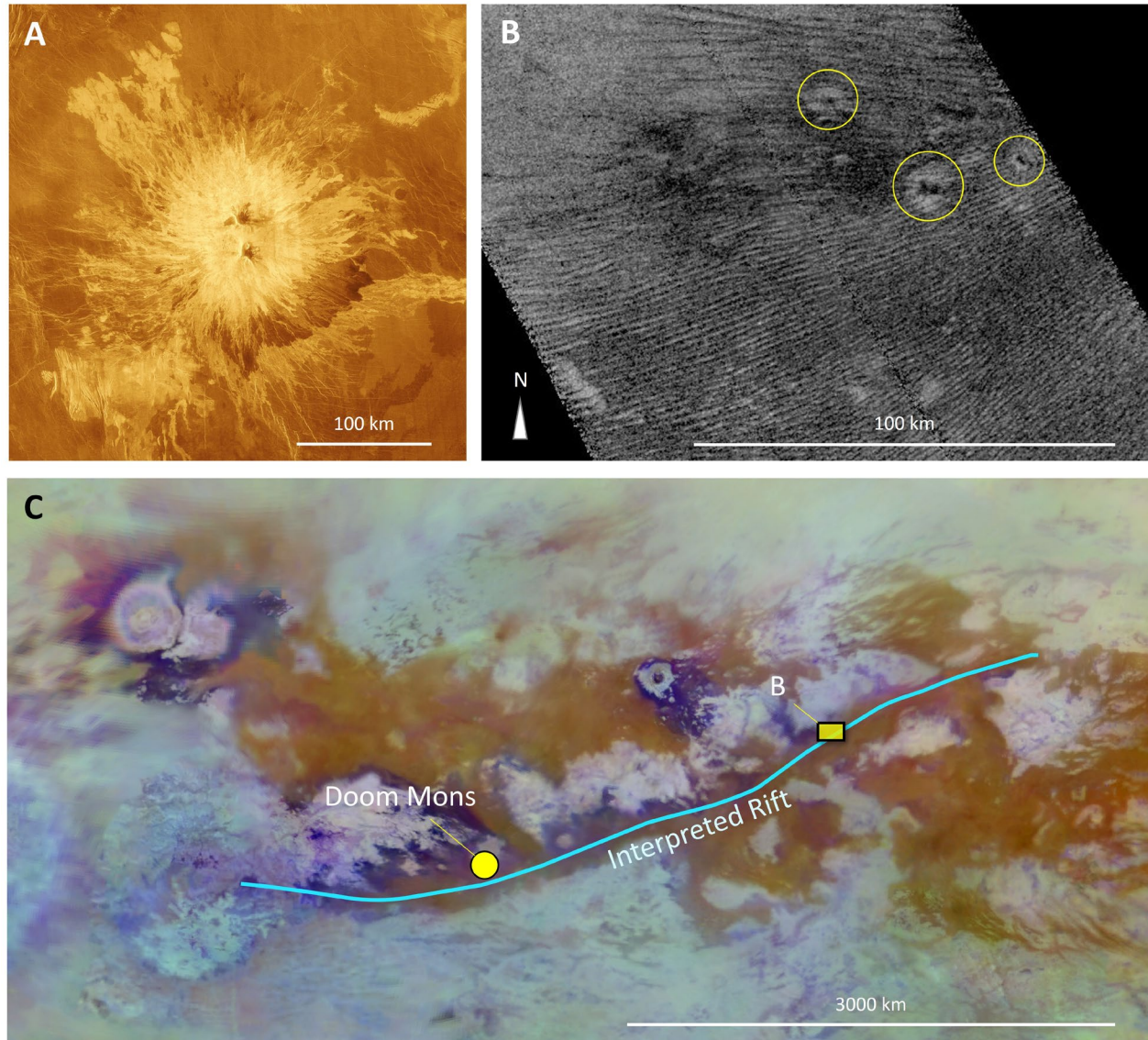


Figure 25. a) Sapas Mons from SAR imagery captured from Magellan on Venus. b) Interpreted cryovolcanoes from Cassini SAR imagery on Titan within interpreted rift. c) VIMS imagery centered on interpreted rift with location of b) outlined by black and yellow box. Location of Doom Mons is labelled with a black and yellow circle. Axis of interpreted rift is outlined with a light blue line.

Previous models have concluded that sand on Titan has migrated anywhere from only 45 km (Charnay et al., 2015) to around the entire equator (Barnes et al., 2015). Fig. 24 appears to help resolve this debate. Based on our interpretation that VIMS-blue materials are the primary sand source, and observations of upwind margins of Aztlan closely resembling upwind margins of

VIMS-blue surfaces, we concluded that much of the sand within Aztlan has not migrated more than 300 kms.

Although Aztlan may be a younger sand sea compared to others across Titan (based on its small size and lack of most abundant icy organic sand deposits), the shapes of sand sea margins across their downwind extents generally often appear feathery and the distribution of dark gray ISS regions suggest that typically the furthest downwind reaches of the sand seas have not been significantly obstructed. If sand had migrated distances of more than ~300 km., then we would likely see ISS-dark regions just north and just south of the current extent of the sand seas because of global opposing wind directions oriented towards the equator at these mid-latitudes. Additionally, if sand had migrated larger distances sand sheets should be visible across low lying

7. Mid-Latitude Icy Organic Gravel Sheets, Dune Fields and Sand Sheets

We observed several mid-latitude, isolated, lobate features previously identified as macula (Fig. 1). These features (lower left of images within Fig. 26) appear VIMS-brown (except in the case of Elpis Macula which is partially VIMS-purple), ISS-dark, and SAR-dark. Observed macula are also located upwind of more diffuse VIMS-brown deposits. We interpreted these diffuse VIMS-brown surfaces to be sand sheets, based on their elongate shapes that parallel the dominant wind directions (Malaska et al., 2016), generally brown color in VIMS, and relatively darker values in ISS and SAR.

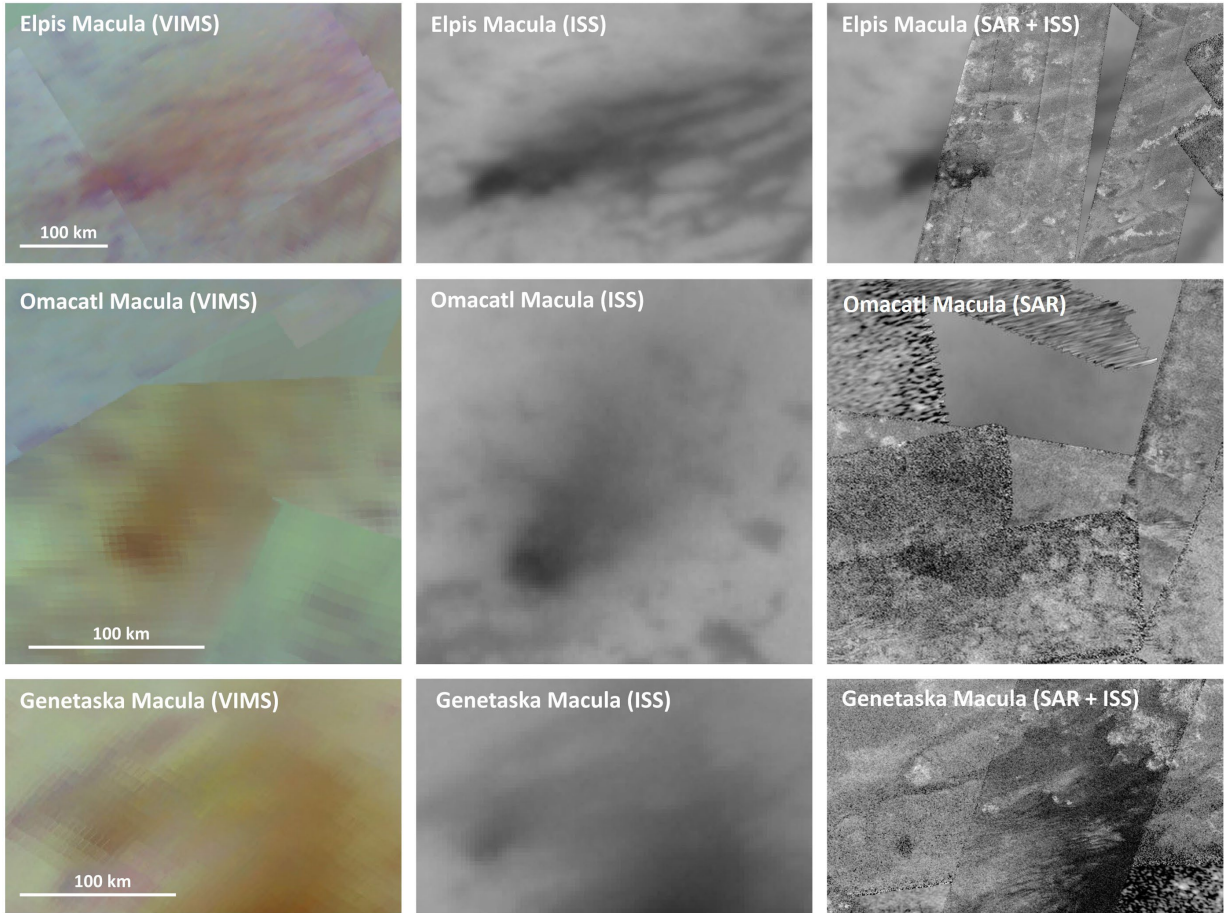


Figure 26. Lobate sand sheets associated with maculas. Elpis Macula (top), Omacatl Macula (middle), and Genetaska Macula (bottom) with diffuse downwind sand deposits in VIMS, ISS, and SAR (left to right). All are VIMS brown, ISS dark, and portions are SAR dark. See Fig. 28 for reference.

Fluctus are defined as being overall SAR-bright and lobate features that emanate from SAR-bright fans which terminate SAR-bright channels. Originally these features were assumed to be associated with cryovolcanism (summarized by Lopes et al., 2013); however, closer inspection revealed that many are likely the result of fluvial activity and associated fans are probably alluvial fans (Jaumann et al., 2009). More recent research concluded that fluctus may be shaped by aeolian processes as many are oriented parallel with dominant wind directions (Malaska et al., 2016).

We observed that fluctus appear as SAR-bright (plausibly gravel) VIMS-blue surfaces adjacent to and downwind of alluvial fans at midlatitudes. Both the interpreted gravel sheets and

associated alluvial fans appear to curve towards dominant wind directions (Malaska et al., 2016). Observed fluctus appear to be wind-transported, icy organic gravel sheets. Calculated saltation threshold velocities by Lorenz, (2014) and Comola et al. (2021) further support this interpretation as they calculated threshold velocities for gravel sized clasts made of approximated densities for sediment on Titan to be less than 0.3 m/s. This threshold velocity is below normal calculated wind speeds of 0.5 m/s (Lorenz, 2021) and measured wind speeds by Huygens at the surface, which were ~ 1 m/s (Bird et al., 2006). Gravel sheets are observed in several wind-dominated regions on Earth, such as the Puna of Argentina (Bridges et al., 2015, De Silva et al., 2015).

Although sand dunes are generally restricted to the equatorial latitudes (Brossier et al., 2018; Radebaugh et al., 2010), there may be some dune fields at even greater latitudes than the isolated sand sheets in Fig. 26. Radebaugh et al. (2011), Rodriguez et al. (2014), and Lopes et al. (2019) interpreted dunes from SAR imagery across Winia Fluctus, an icy organic gravel sheet at 53° , 42° , far north of Fensal (Fig. 27a).

Similar gravel sheets and dune fields were observed across virgae (Fig. 27b), which are identified as various forms of relatively more angular sheets of ISS-dark material. Many virgae have already been previously mapped as containing sand sheets and dunes (Brossier et al., 2018; Lopes et al., 2020). Based on correlations across ISS, VIMS, and SAR imagery, it is possible that the primary differences between virgae and fluctus are topographic obstacles creating more linear margins for virgae, such as those found by Malaska et al. (2016) adjacent to Perkunas Virgae. We also found slightly greater coverage of sand across virgae. Outer regions of virgae, particularly across upwind margins, tend to be SAR-bright (Fig. 27b) and VIMS-blue or purple (Fig. 1). Both fluctus (other than the likely cryovolcanic feature Mohini Fluctus near Doom Mons) and virgae

are oriented parallel with dominant wind directions, are ISS-dark, and tend to be VIMS-blue. A few fluctus are difficult to correlate from SAR to ISS and VIMS due to poor resolutions.

Moderate latitude dune fields across fluctus and virgae tend to be isolated, small, and appear to be overwhelmed visually in low resolution VIMS imagery by surrounding and interdunal VIMS-blue surfaces. Due to their subtle nature and small surface areas, they were not included in the global-scale map (Fig. 11).

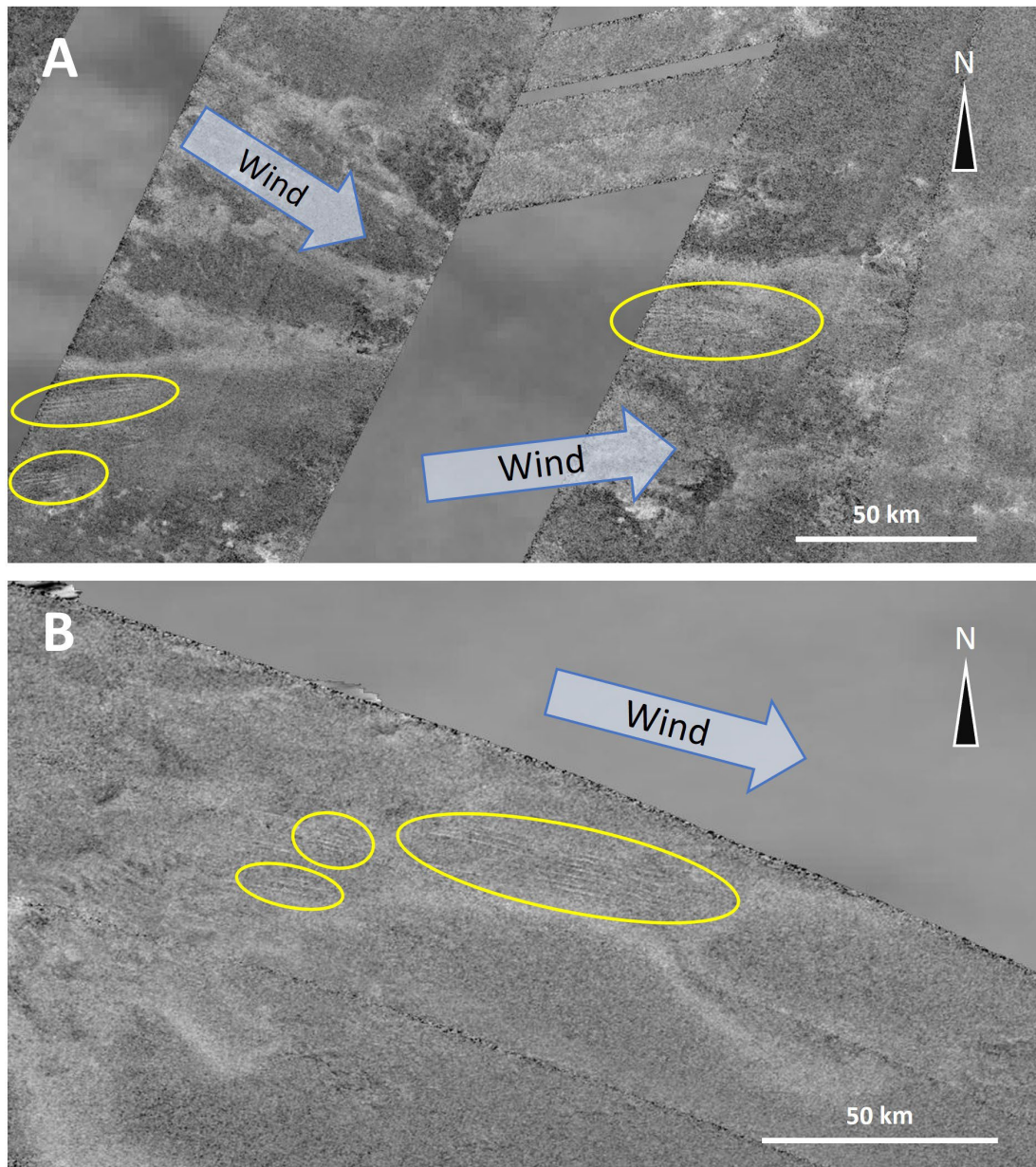


Figure 27. SAR imagery of linear, possibly stabilized dunes at or near mid-latitudes. Yellow ovals denote locations of observable linear dunes. a) Perkunas Virgae, a region south of southeastern Shangri-La at -28° , 159° , that was previously mapped as having sand dunes (Brossier et al., 2018). b) Winia Fluctus, far north of Fensal at 53° , 42° , is a SAR-bright lobate feature with features previously interpreted to be linear dunes (Rodriguez et al., 2014; Lopes et al., 2019). Narrow, SAR-bright features are consistent with radar reflections seen on dunes at equatorial latitudes (Neish et al., 2010). Dominant wind directions in both images are from the WNW (Malaska et al., 2016). See Fig. 13 for locations.

Although SAR imagery is limited, we made correlations with VIMS and higher resolution ISS imagery in order to identify several mid-latitude sand and gravel sheets (Fig. 27).

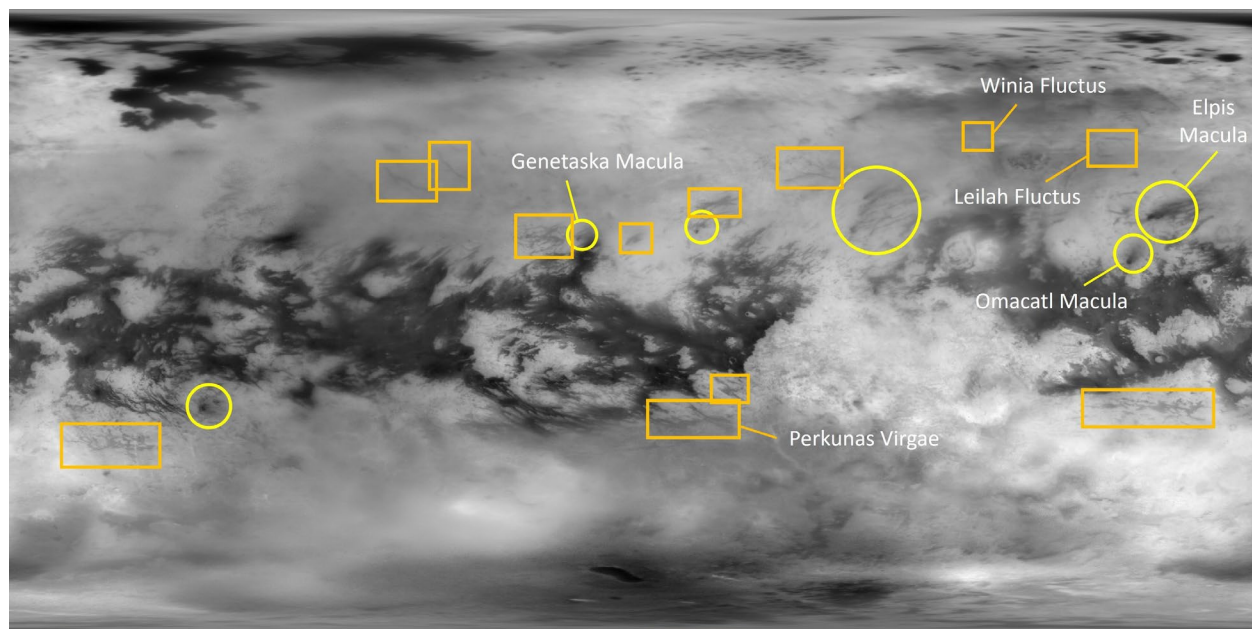


Figure 28. Global ISS imagery as a locator map outlining interpreted VIMS-blue gravel sheets (orange rectangles) and lobate VIMS-brown sand sheets (yellow circles). Areas of interest focused on in this work are labelled. Compare with Fig. 1.

It is also worth noting that yardang fields have also been identified within mid-latitudes (Paillou et al. 2016; Northrup, 2018). The most probable candidates are all unassociated with fluctus and virgae, and appear ISS-bright, VIMS-bright, and SAR-bright. Likely yardang field candidates tend to lie within relatively circular SAR-bright features and some have been associated with isolated rises of exposed bedrock (Northrup, 2018). Although yardangs can have similar linear shapes to linear dunes, we argue that they can be differentiated by the regions they occupy and SAR values that traverse crests. Paillou et al. (2016) found that linear dunes' triangular shape in cross section spaced apart by relatively horizontal interdunes cause backscatter that would result in the pattern of SAR-dark, bright, and gray observed in dunes across Titan. This same pattern is

present in a more muted form across the interiors of some fluctus including Winia Fluctus (Fig. 27b).

8. Sand Producing Environments

8.1 Wind-swept, Reshaped Alluvial Fans

One possible dominant environment responsible for sand production on Titan is wind swept alluvial fans. The distribution of sand seas across broad relatively high elevation regions (Fig. 12) and observations of drainage termini across equatorial and temperate latitudes (Figs. 10, 23, 27, 30) support this hypothesis. Greater rates of precipitation exist across more temperate latitudes than across the equator (Birch et al., 2016). Consequentially, the transportation of sediment is likely more influenced by fluvial interactions at higher latitudes. Hesse (2019) found that across wetter environments alluvial fans tend to exist unburied, while across drier environments wind selectively transports sand from the alluvial fans and accumulates it in dunes and sand sheets across adjacent downwind alluvial fans (Fig. 29).

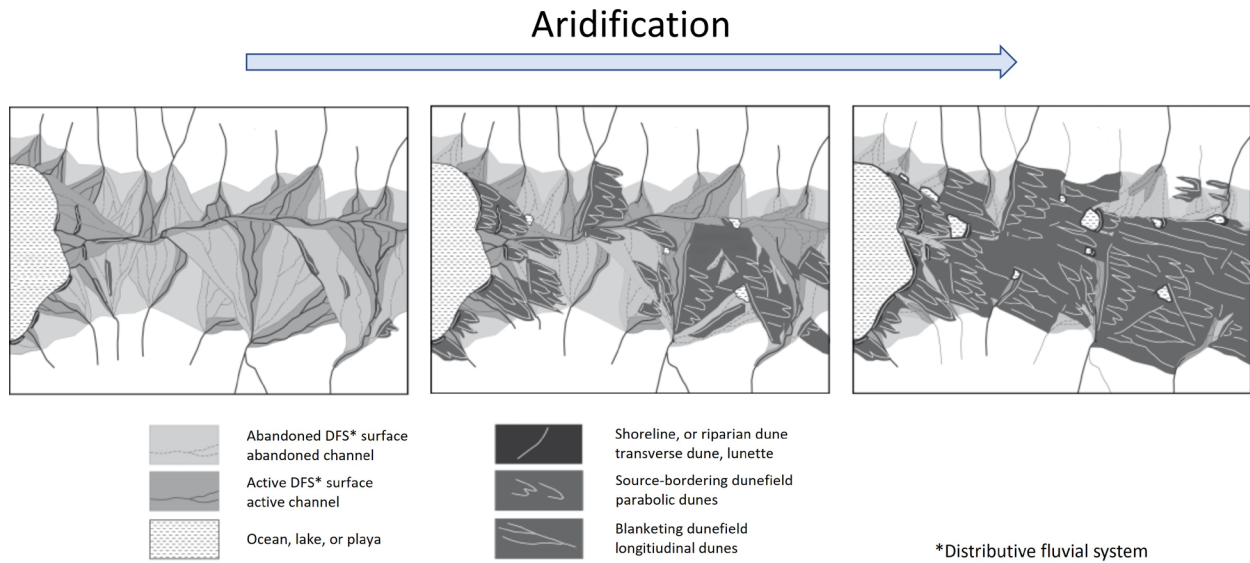


Figure 29. Illustration adapted from Hesse (2019), which was adapted from Weismann et al. (2010) showing affects of aridification on a system of alluvial fans. Over time, wind dominates the transportation of sediment, sorting out sand from the alluvial fans and burying them.

In addition to Winia Fluctus, we also interpreted linear dunes across the center of Leilah Fluctus (Fig. 30). Comparing these observations with Fig. 29, we concluded that within Hesse's diagram these fluctus represent a relatively wet, fluvially-dominated environment.

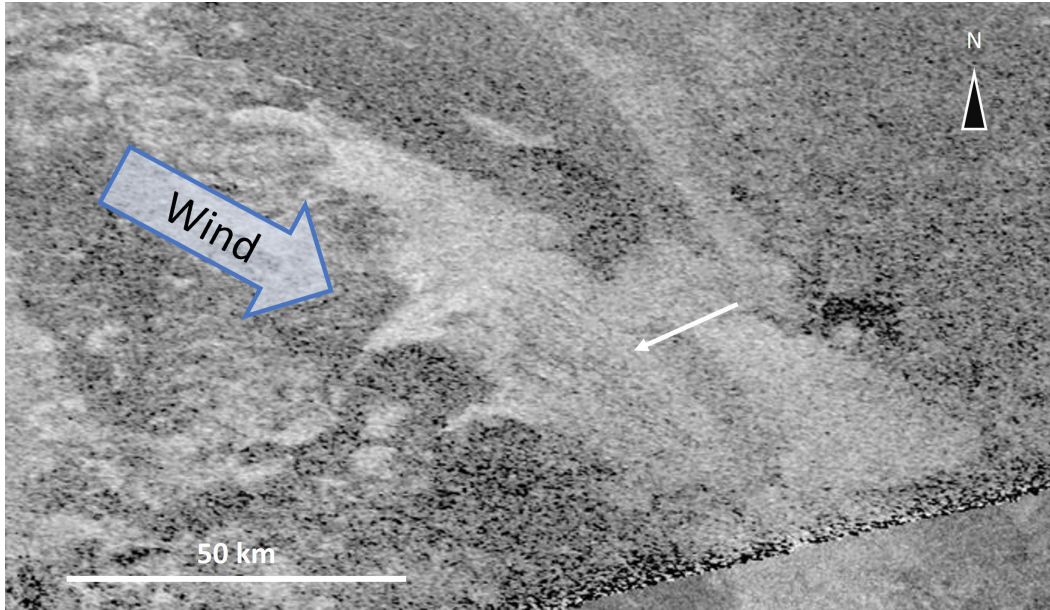
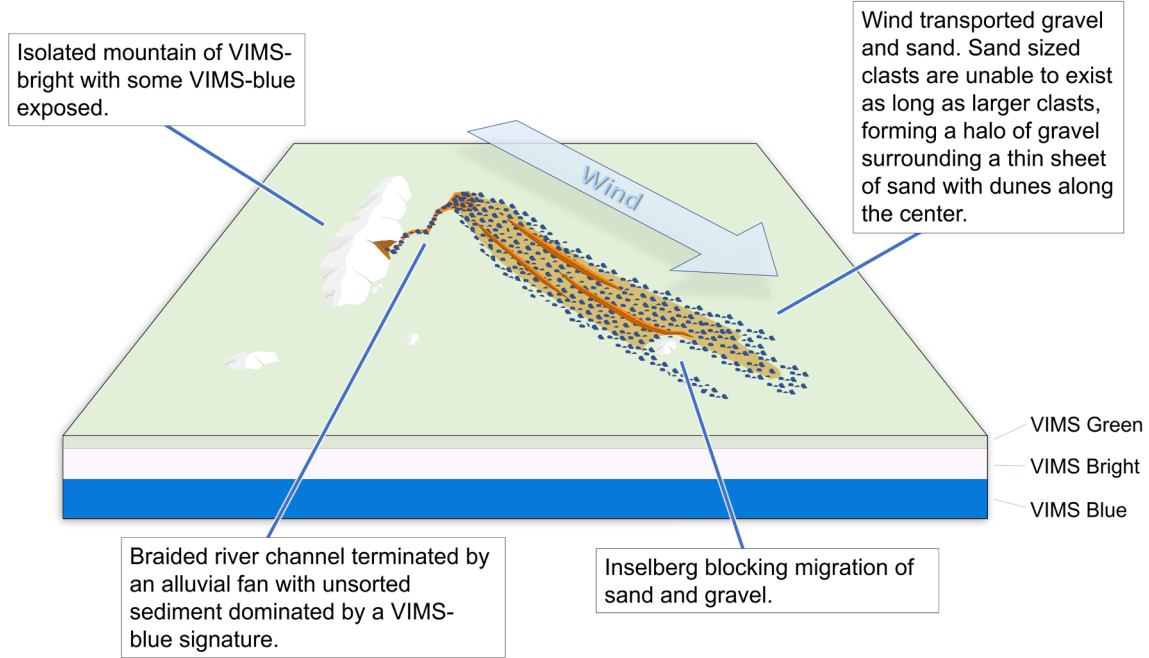


Figure 30. Leilah Fluctus, a SAR-bright surface immediately downwind of and possibly sourced from wind-swept alluvial fans at 51.2° N, 100.7° E, roughly 475 km north of Fensal. Dominant wind direction is ESE. White arrow is directed towards an interpreted dune field with linear dunes.

To further illustrate our interpretation of fluctus, we created the block diagram Fig. 31 with both VIMS and DISR (near visible light) color schemes.

A



B

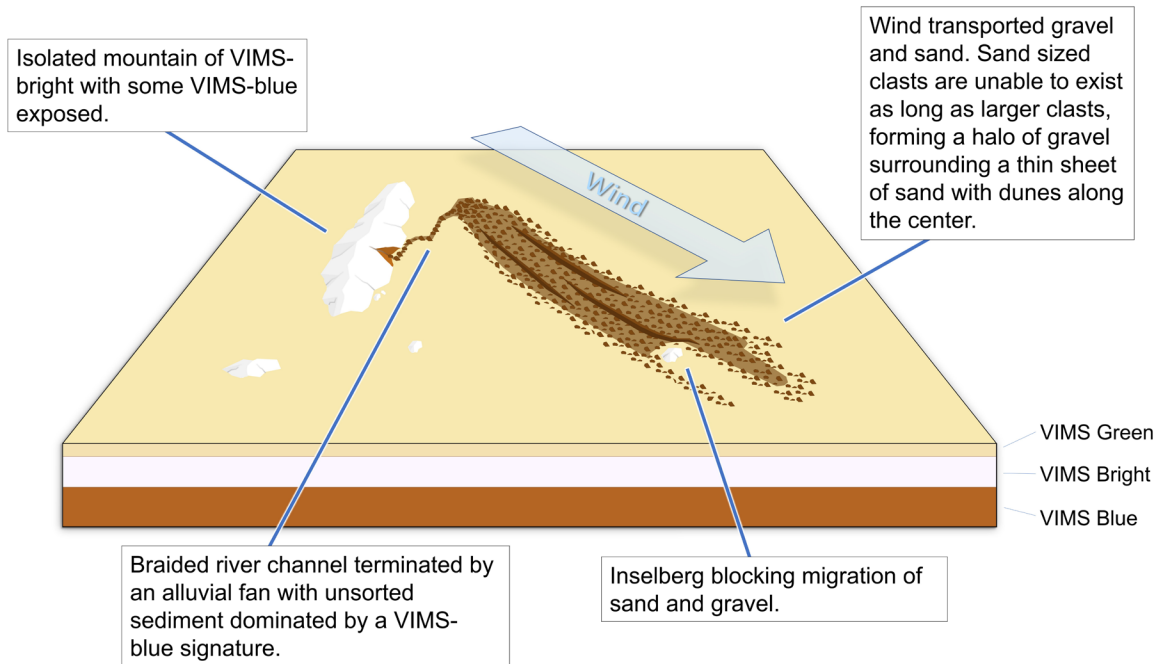
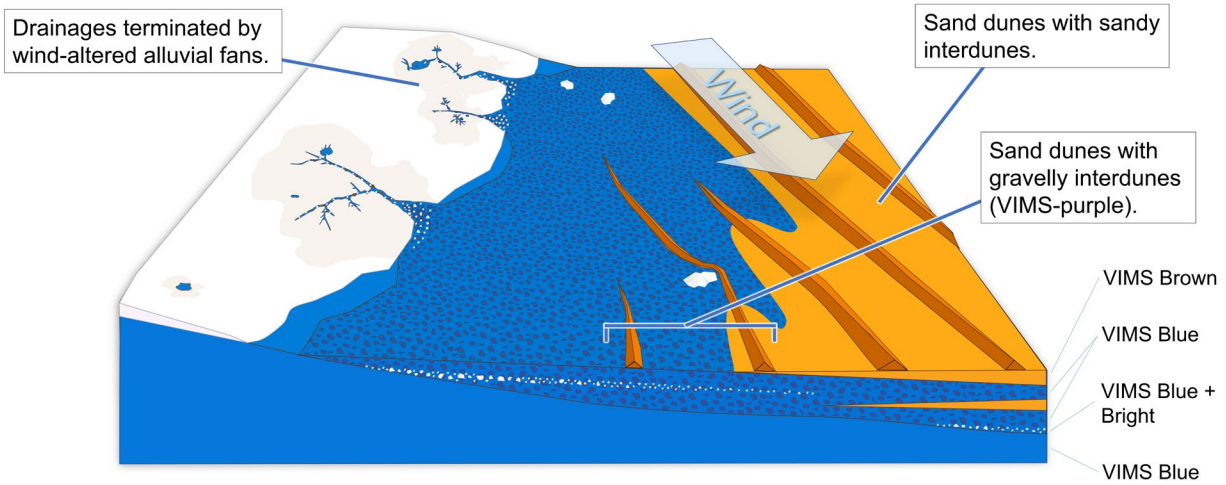


Figure 31. Block diagram of sand produced from isolated wind-swept alluvial fan at a temperate latitude based on observations of Leilah Fluctus (Fig. 30). a) VIMS color scheme and b) Huygens descent imagery (near true color) color schemes.

It has been previously observed that alluvial fans are mostly distributed across the mid-latitudes where coincidentally there are greater rates of precipitation than at the equator (Birch et al., 2016). Drainage termini at equatorial latitudes appear to be largely influenced by other forces other than fluvial activity as there are several fluvial channels, but few observed alluvial fans there. We propose that alluvial fans across equatorial latitudes have been altered by burial from wind transported sediment, and by sand and pebble-sized clasts from the alluvial fans being transported downwind. For example, we interpret the lack of significant VIMS-blue surfaces adjacent to Belet as being a result of VIMS-blue alluvial fans being buried by VIMS-brown sand. We suggest that VIMS-blue and VIMS-bright sediments are deposited at the terminus of drainages where alluvial fans form during flash flood events, or periodic wet climates. VIMS-bright sediments quickly disintegrate (Jaumann et al., 2008), and sand sized VIMS-brown clasts (which previously existed as VIMS-blue gravels and cobbles [see Section 3]) are transported by wind and accumulate in adjacent dune fields and sand seas (Fig. 32).

A



B

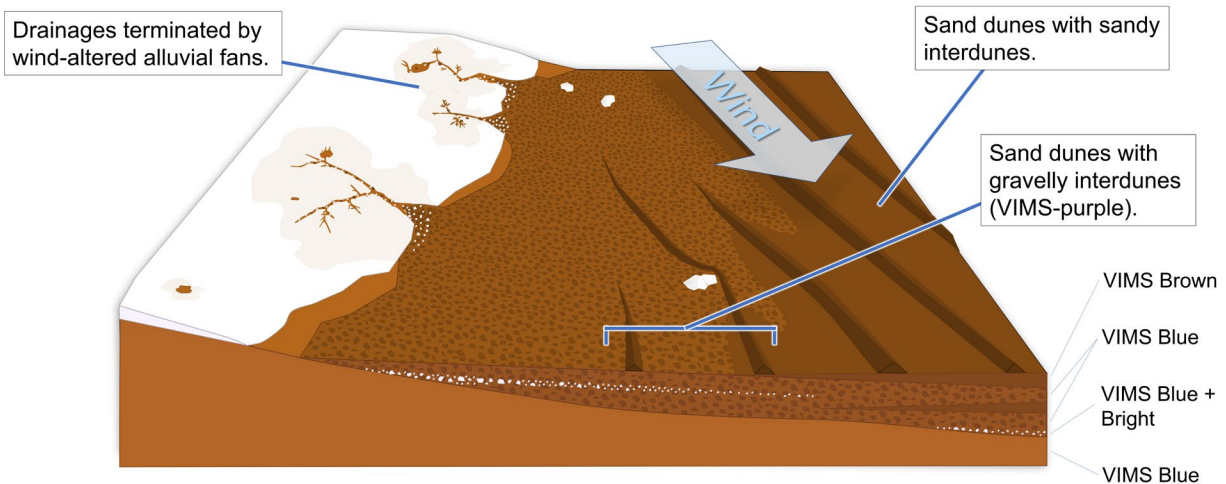


Figure 32. Illustrations depicting the primary interpreted method of sand production on Titan. a) VIMS color scheme and b) Huygens descent imagery (near to true visible color) color schemes. Occasional storms fill drainages and liquid methane rivers fluvially erode VIMS-blue and overlying VIMS-white materials into sediments, which are deposited at the terminus of drainages. Wind transports gravels and sand downwind of the drainages and organizes the sediments into VIMS-blue gravel sheets and VIMS-brown sand seas. VIMS-bright materials quickly disintegrate and dissolve. During wetter climates alluvial fans prograde, while during dry climates sand deposits transgress across the basin. These cycles are preserved in patterned deposits beneath the sand sea.

We compare this generalized interpreted method of sand production and transport on Titan to the Nafud desert in northern Saudi Arabia (Fig. 33). Lower Paleozoic quartz arenites from the Tabuk Formation to the west of the Nafud Sand Sea are the primary source rocks, and appear to be comparable to VIMS-blue exposures within highlands on Titan. Basalt flows overlay the Tabuk Formation and supply an insignificant amount of sediment to the Nafud Sand Sea, perhaps similar to VIMS-bright materials (Garzanti et al., 2013). Although there is fluvial erosion on the upper layer of basalt in the Nafud Desert, most of the basalt breaks down to clays and ions through chemical weathering, reducing the presence of sand-sized basalt clasts. Braided river deposits at the base of drainages that lead toward the sand sea appear to have pebble to cobble sized clasts of basalt mixed with sand derived from the Tabuk Formation (Fig. 33a), and the downwind sand sea has little basalt sourced sediment (Garzanti et al., 2013). The landscape morphologies, materials involved, and distributions of materials all have characteristics similar to those observed at the Huygens landing site (Fig. 33b; Garzanti et al., 2013; Jaumann et al., 2008). Both regions have highlands mantled with partially soluble materials, and the primary source rocks for the sands appear to be the underlying materials. Within the Nafud Sand Sea there are negligible amounts of basalt-sourced materials (Garzanti et al., 2013). Similarly, the spectral data of the sandy surfaces on Titan is more similar to VIMS-blue than VIMS-bright surfaces, indicating the sands reflect their source and not other adjacent materials. To further compare the Nafud Desert to the Huygens landing site, we inverted the colors of Fig. 33a and covered it with a partially transparent orange-brown layer in GIMP (see Fig. 33c).

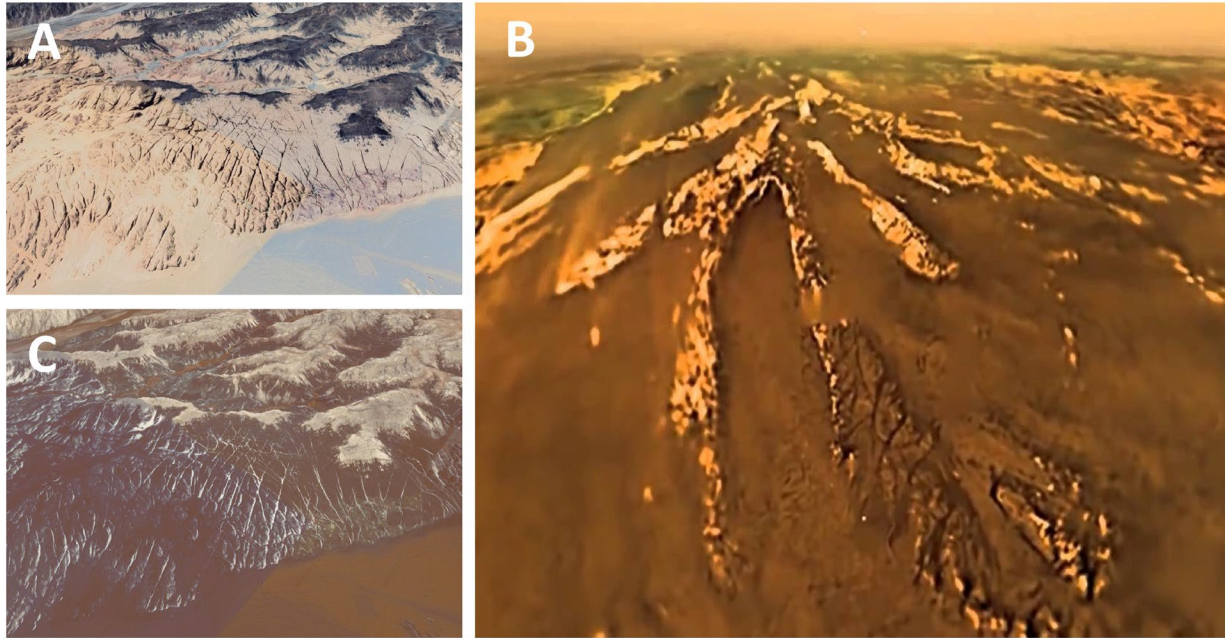


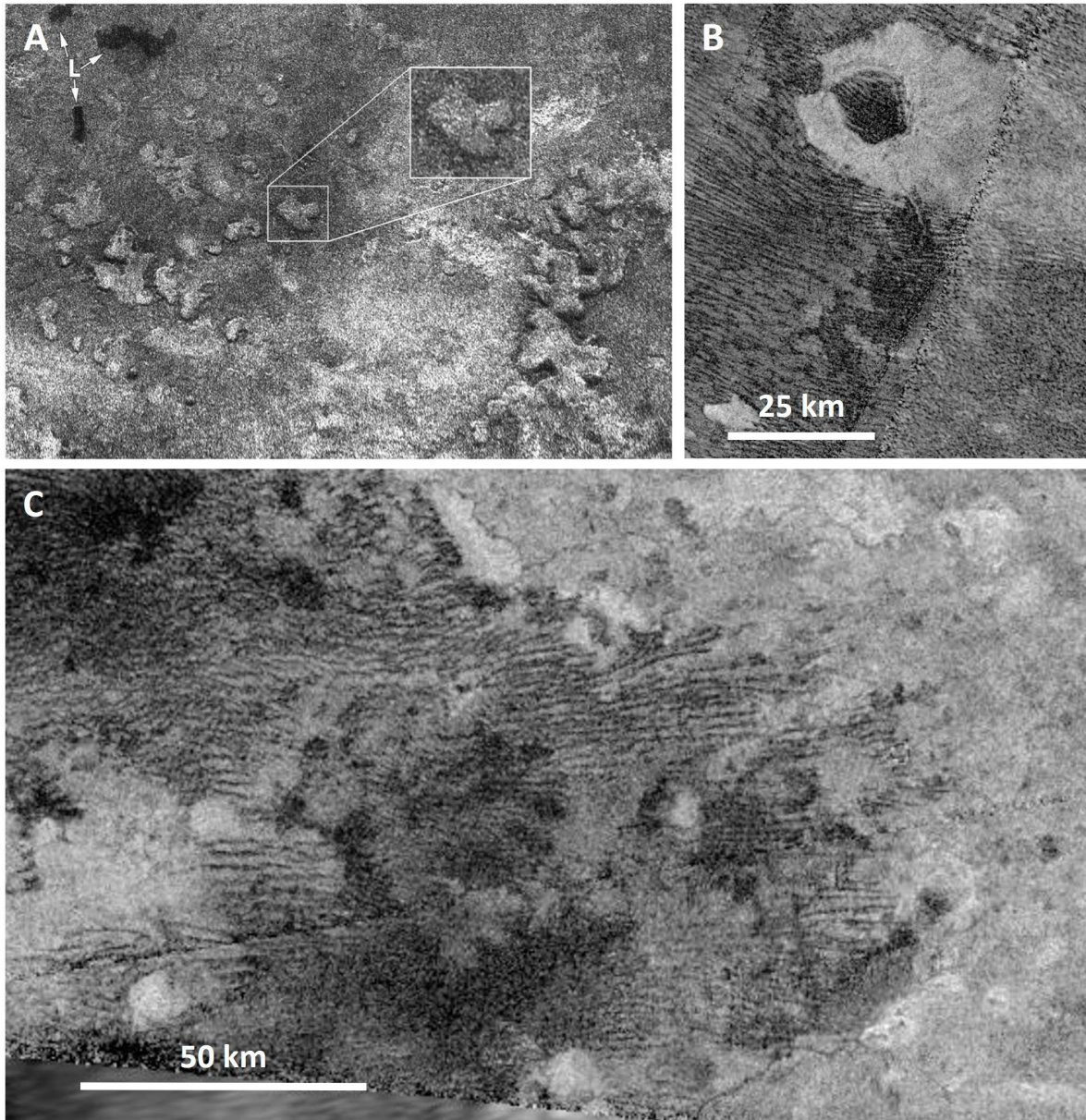
Figure 33. a) Western Nafud desert upwind of Nafud Sand Sea showing jointing within the light tan Tabuk sandstone, and overlying dark basalt flows. b) Huygen descent imagery showing similar jointing to a) within a dark brown material correlated with VIMS-blue. c) Same as a), but with values inverted and covered with a partly transparent orange-brown layer in GIMP for further comparison with b).

8.2 Lakebeds

Computer models (Lora et al., 2014; Mitchell and Lora, 2016) and reasoning based on orbital characteristics and distributions of various lacustrine features (Hörst, 2017) suggest that Titan undergoes regular large scale climate fluctuations. Cooler temperatures promote condensation of methane, while warmer temperatures promote the evaporation of methane. Lorenz et al. (2013) suggested that as Titan warms, liquid bodies of methane evaporate and are abandoned.

Close examination of SAR imagery has revealed possible SAR-dark lakebeds beneath sand seas (Fig. 34). One of these interpreted lakebeds is surrounded by channels and drainages that appear to empty into them (Fig. 34b). All of these interpreted lakebeds have similar overall shapes to previously identified lakebeds and active lakes (Fig. 34a), and have generally higher concentrations of dunes than the surrounding regions of the sand seas they occupy. These SAR-dark features

are correlated to VIMS-brown and are assumed to be covered with sand. Other SAR-bright lakebeds previously identified by Barnes et al. (2011) appear VIMS-bright and have been interpreted to be covered by evaporite deposits. These evaporite covered lakebeds appear across polar latitudes and within Xanadu far from any visible deposits of sand. We suggest that interpreted lakebeds within sand seas may or may not have also been originally covered with evaporites, but are now buried by VIMS-brown sand. It is of more importance that the interpretation of these features allowed us to investigate the origins of macula and associated sand sheets which make up some of the most distal regions of sand seas.



Figures 34. SAR imagery of a) previously identified active lakes (L) and paleolakes (bright lobate patches covering much of image, outlined by distinct bright and dark margins) in polar regions (Moore and Howard, 2010). b) Eastern Shangri-La with a SAR-bright channel leading to an interpreted SAR-dark paleolake, and c) eastern Belet with several probable SAR-dark paleolakes. Notice consistent morphology, but different scattering properties of the surfaces of these interpreted paleolakes. It is likely that the bright polar paleolakes are covered with rough textured evaporite deposits, while dark equatorial paleolakes are behaving as sediment sinks and are accumulating sand.

As with alluvial fans, it appears that the currently dry equatorial latitudes may also be more strongly influenced by wind than the accumulation of sediment from past lacustrine activity. Dark

lobate features in SAR are typically located within regions mapped as having abundant sand deposits (Figs. 2, 11, 34), suggesting lakebeds are behaving as localized basins that trap sediment. However, there is not a clear correlation of lakebeds and downwind abundant sand deposits within sand seas suggesting that much of the sand within sand seas is not sourced from lakebeds.

At more moderate latitudes are macula (previously described in Section 7), which appear similar to the interpreted lakebeds previously mentioned within sand seas in SAR. We similarly interpret these as lakebeds. Macula, however, are strongly associated with isolated downwind VIMS-brown sand sheets (Fig. 35). Elpis and Genetaska Macula specifically have previously been mapped as having dunes (Brossier et al., 2018).

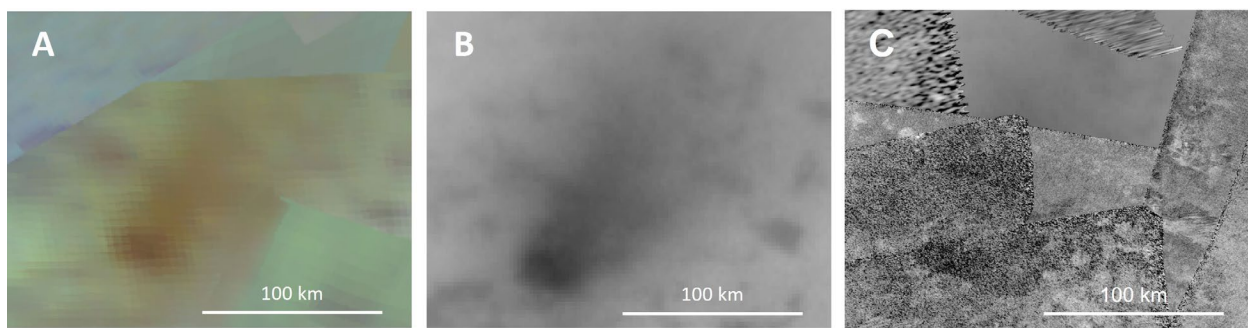
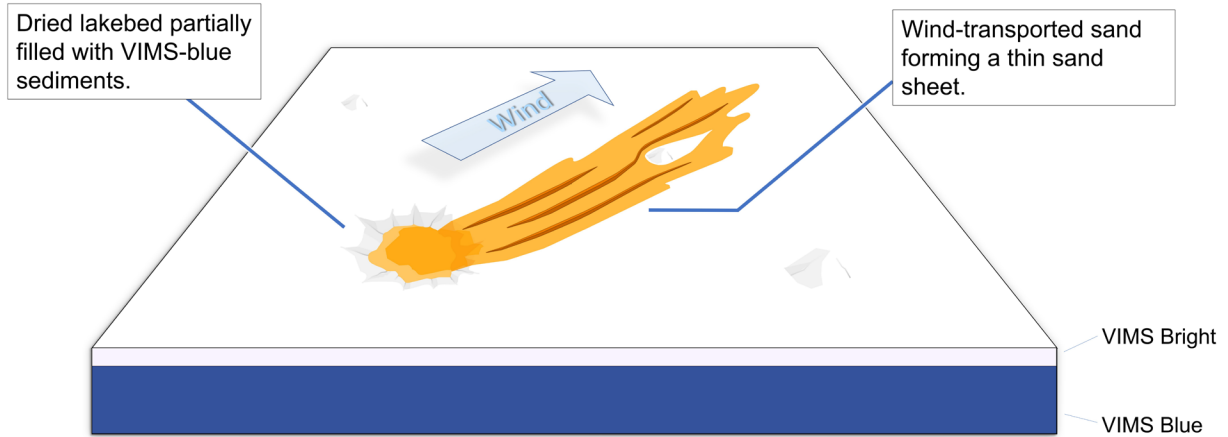


Figure 35. Omacatl Macula, a probable dried lakebed containing VIMS-brown sediment surrounded by VIMS-bright deposits acting as a sand source for an isolated sand sheet. a) ISS, b) VIMS, and c) SAR.

We interpret VIMS-brown lakebeds, such as those that likely occupy macula, to be sand sinks. Some of these appear to be losing sand from wind and are behaving as sand sources for isolated sand sheets and dune fields (Fig. 36).

A



B

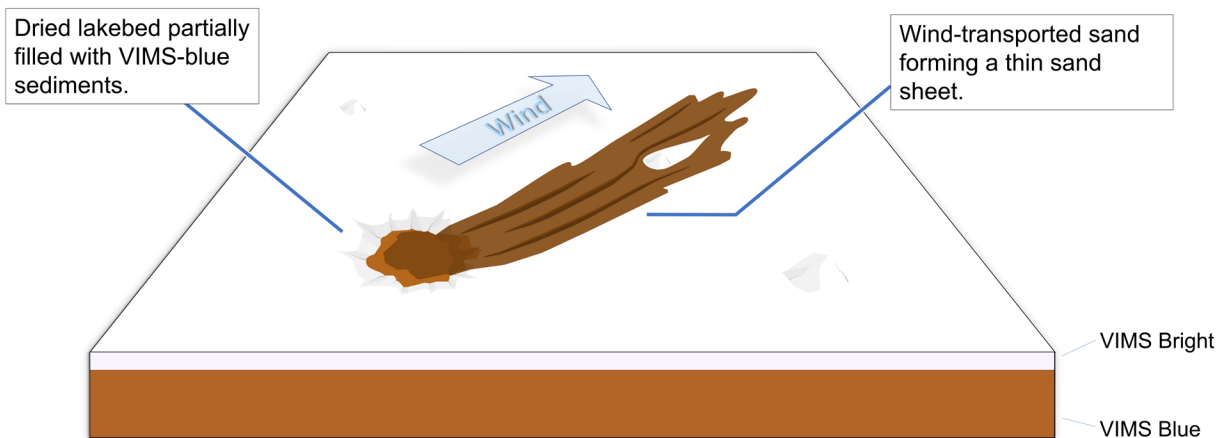


Figure 36. A model of a dried lakebed containing VIMS-brown sediment surrounded by VIMS-bright deposits acting as a sand source for an isolated sand sheet. Based on observations of macula in SAR and VIMS (Fig. 35), and mapped interpretations by Brossier et al. (2018). VIMS color scheme a), and color scheme based on Huygens descent imagery b).

Numerous paleolakes have also been identified throughout the western Nafud Desert adjacent to and upwind of the sand sea amongst wadis (ephemeral river channels). This region has been identified as a deflation zone, such that sand first deposited within these paleolakes is now within the Nafud Sand Sea (Rosenberg et al., 2013). Some paleolakes were also identified beneath

the sand sea (Parton et al., 2018; Breeze et al., 2017; Rosenberg et al., 2013). It is possible that paleolakes underneath sand seas on Titan, such as those interpreted from Figure 34, acted as sand sources and are now accumulating sediment from other upwind paleolakes and other various sand sources.

8.3 Impact Craters

We interpreted 2 examples (downwind regions of Sinlap and Menrva) of precipitated VIMS-blue sediment sheets from impacts acting as sand sources for downwind dunes. Interpretations were based on comparisons with ISS, VIMS, and SAR imagery. Due to the apparent relatively minor amounts of sand produced by these sheets compared to the previously outlined methods of sand production, and the difficulty of creating an accurate block diagram without revealing concepts explained in better detail in Section 8, we encourage the reader to consider viewing the appendix for more information regarding impact craters as sand sources.

9. Titan's Stratigraphy and A Proposed Geologic History

9.1 Stratigraphy Exposed in Impact Craters

Several impact craters, including Sinlap, Selk, and Paxsi (Fig. 37) have VIMS-blue materials within crater floors and across ejecta when present. This pattern was also observed in previous work (Neish et al., 2015; Hofgartner et al., 2016; Brossier et al., 2018). Additionally, more weathered impact craters tend to have larger exposures of VIMS-bright within crater floors and are lacking ejecta (Hofgartner et al., 2016). We observed VIMS-bright central rebound features surrounded by VIMS-blue surfaces. Correlations between VIMS and ISS imagery of Sinlap and Selk suggest VIMS-bright and VIMS-blue materials are within their ejecta (Fig. 37; Brossier et al., 2018). It is

important to note that the outermost VIMS-blue surfaces from the crater rims of Sinlap and Selk have been interpreted to be the result of vaporization, condensation, and precipitation of impact-vaporized water (Le Mouelic et al., 2006; Brossier et al., 2018), and were likely deposited after the ejecta.

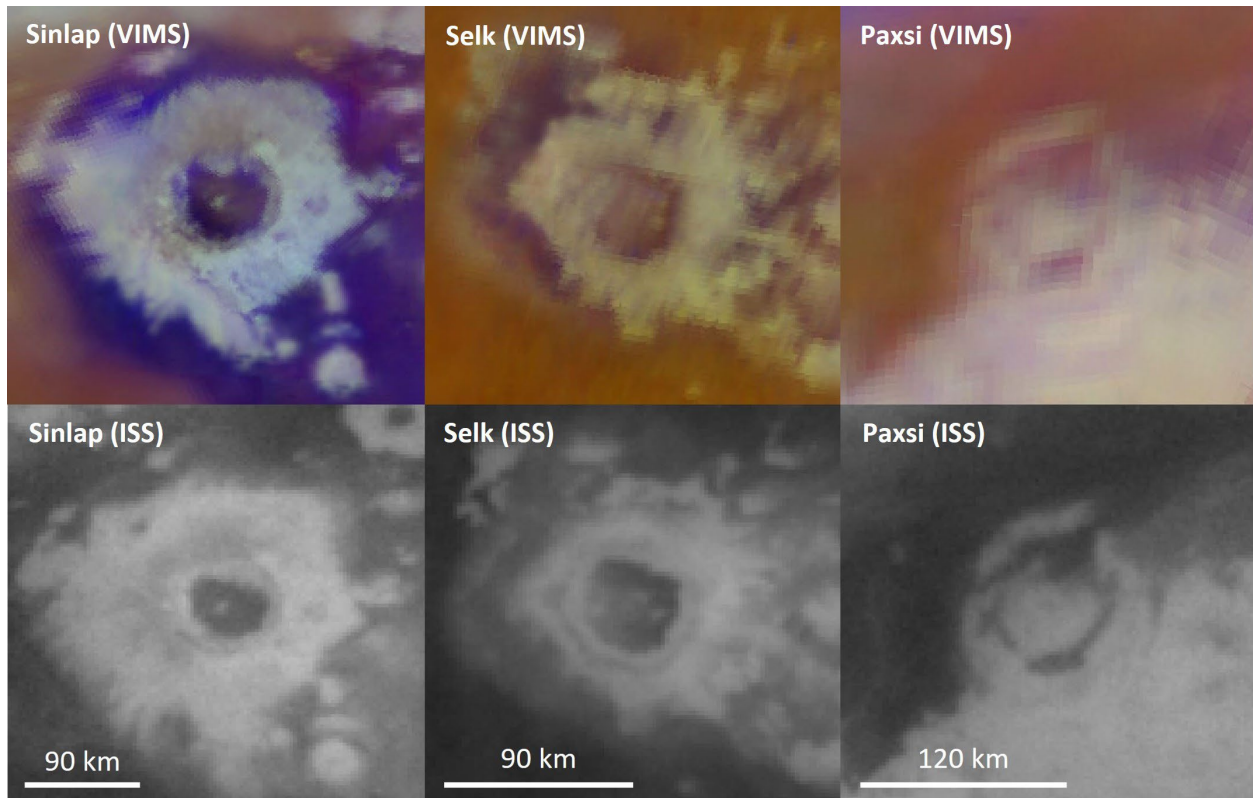


Figure 37. Sinlap, Selk, and Paxsi impact craters ordered according to increasing level of degradation (left to right), with rim diameters of 88 km, 84 km, and 115 km respectively (diameters measured by Hedgepeth et al., 2018). Top row is VIMS, bottom row is ISS. Notice that even after significant erosion there are still both VIMS-blue and VIMS-bright materials present.

Sinlap, Selk and Paxsi all have VIMS-bright central peaks surrounded by VIMS-blue materials within their crater rims. As VIMS-bright has been interpreted to have little, or no water ice (Jaumann et al. 2009; McCord et al., 2006; Soderblom et al., 2007), and even eroded craters such as Paxsi exhibit alternating patterns of VIMS-blue and VIMS-bright, we conclude the observed

patterns are not entirely the result of fractional melting and are likely caused by the presence of preexisting, alternating layers of VIMS-blue and VIMS-bright in the subsurface.

The Upheaval Dome feature in Canyonlands National Park, Utah has been argued to be a confirmed eroded meteor impact crater due to the presence of shocked quartz and micro fluid structures within quartz crystals (Buchner and Kenkmann, 2008). This probable impact is an ideal terrestrial analog for weathered impact craters on Titan as it has been well surveyed and has a central uplift feature. By comparing the cross section created by Kenkmann, et al., 2005 (Fig. 38) with VIMS imagery, we created an interpreted model of Sinlap crater (Fig. 39).

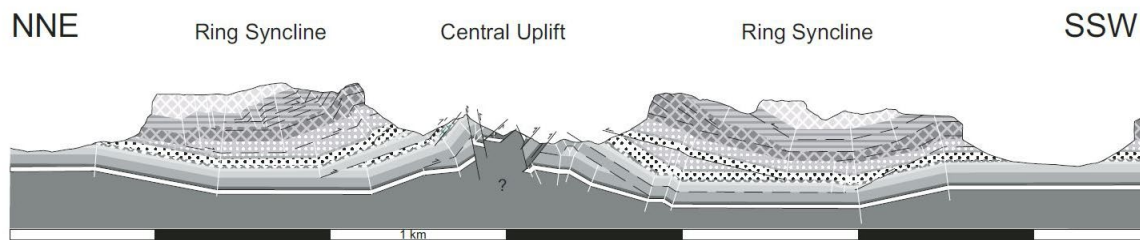


Figure 38. Cross sections of Upheaval Dome, a confirmed weathered impact crater with central uplift. Adapted from Kenkmann, et al., 2005. Compare with Figures 37 and 39.

Previous work concluded that the heat of large impacts such as Sinlap would have vaporized underlying water ice, creating an ephemeral cloud. Because vaporized materials would have had to condense, precipitate, then deposit on the surface, it has been thought that solid ejecta would have deposited first, and then a thin blanket of condensed VIMS-blue materials (Le Mouélic et al., 2006). This interpretation is supported by the lack of correlations between the condensed blanket of VIMS-blue materials surrounding Sinlap in VIMS and SAR imagery as SAR likely penetrates into the shallow subsurface (Brossier et al., 2018; Soderblom et al., 2007). It is thought that ephemeral channels of precipitated methane over time erode this blanket of VIMS-blue material and reveal the dominantly VIMS-bright ejecta.

VIMS-blue surfaces are also exposed within channels that incised the dominantly VIMS-bright ejecta surrounding Sinlap (Figs. 37, 39). We interpreted these VIMS-blue surfaces to be exposures of an underlying layer of VIMS-blue ejecta (separate from the previously mentioned sheet of precipitated VIMS-blue materials) laying underneath VIMS-bright ejecta. Additionally, a faintly VIMS-blue surface is exposed across the upwind, NW slopes of the otherwise dominantly VIMS-bright ejecta cone. We interpret these VIMS-blue surfaces to be the result of wind transporting the uppermost layers of VIMS-bright ejecta.

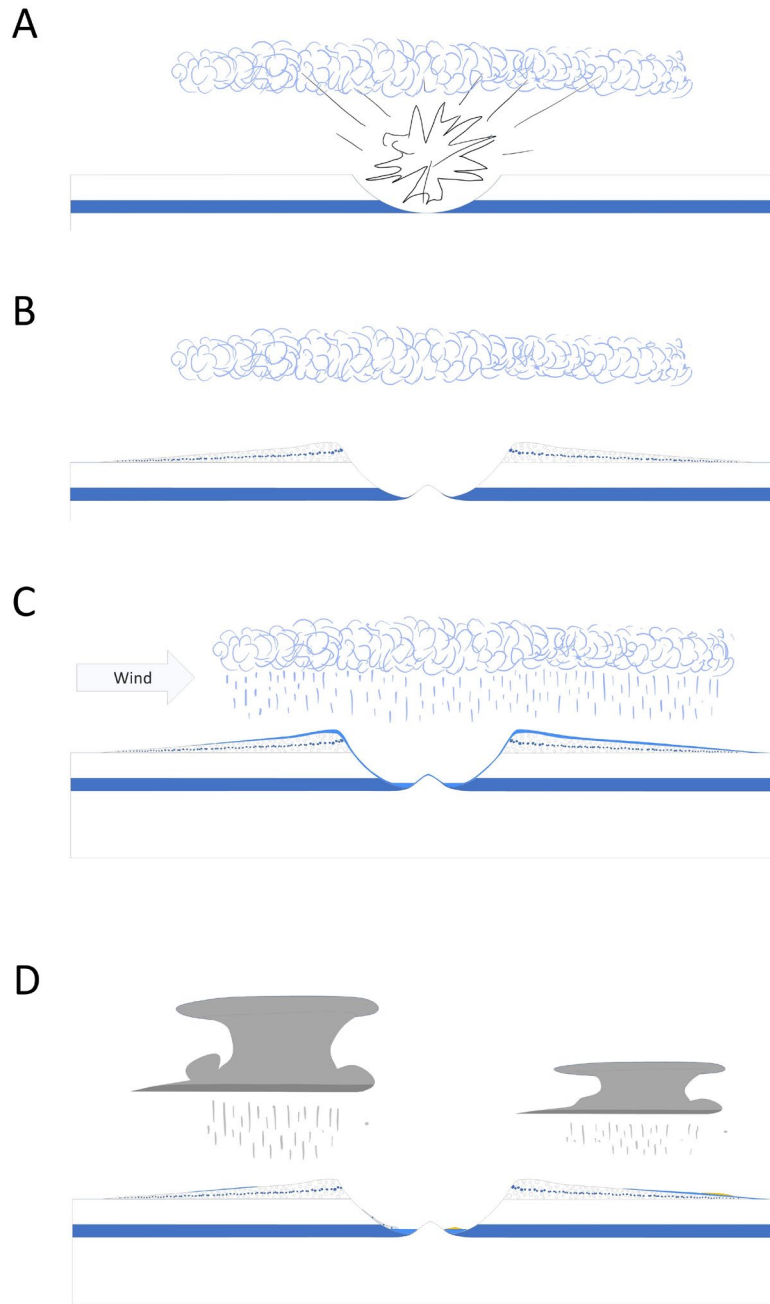


Figure 39. Diagram outlining proposed geologic history of Sinlap crater. a) Moment of impact. Solid ejecta is thrown into the atmosphere. b) Elastic rebound creates a central peak within impact crater. Solid ejecta falls to the surface covering eastern Fensal and is organized with an inverted stratigraphy of the subsurface. Vaporized materials, including water ice, condense as a large cloud. c) The water ice bearing cloud is transported by wind, further condenses and precipitates VIMS-blue materials onto ejecta and crater floor as a thin blanket. d) Precipitated methane erodes away much of the thin layer of VIMS-blue across the upper slopes of ejecta and central peak, and reveals the underlying VIMS-bright ejecta and bedrock respectively. Fluvial channels expose VIMS-blue ejecta. Wind removes some VIMS-bright clasts on the upwind flanks of the exposed ejecta and exposes some underlying VIMS-blue ejecta. Sand from Fensal migrates over some upwind margins of ejecta and landslides occur within the crater.

9.2 Possible Multiple Impact Origin of Xanadu

Brown et al. (2011) and Soderblom et al. (2009) together found evidence for two large eroded impact basins that occupy most of Xanadu. They found annular drainage patterns within both interpreted craters and spectral evidence for evaporites across the floors of basins that occupy the southern regions of the proposed impact craters.

Mapped VIMS-blue surfaces within eastern Xanadu (Fig. 40) are distributed in two concentric circles that resemble a weathered multi-ringed impact basin similar to Odysseus Crater on Tethys. This interpreted impact basin is 1,000 km. wide.

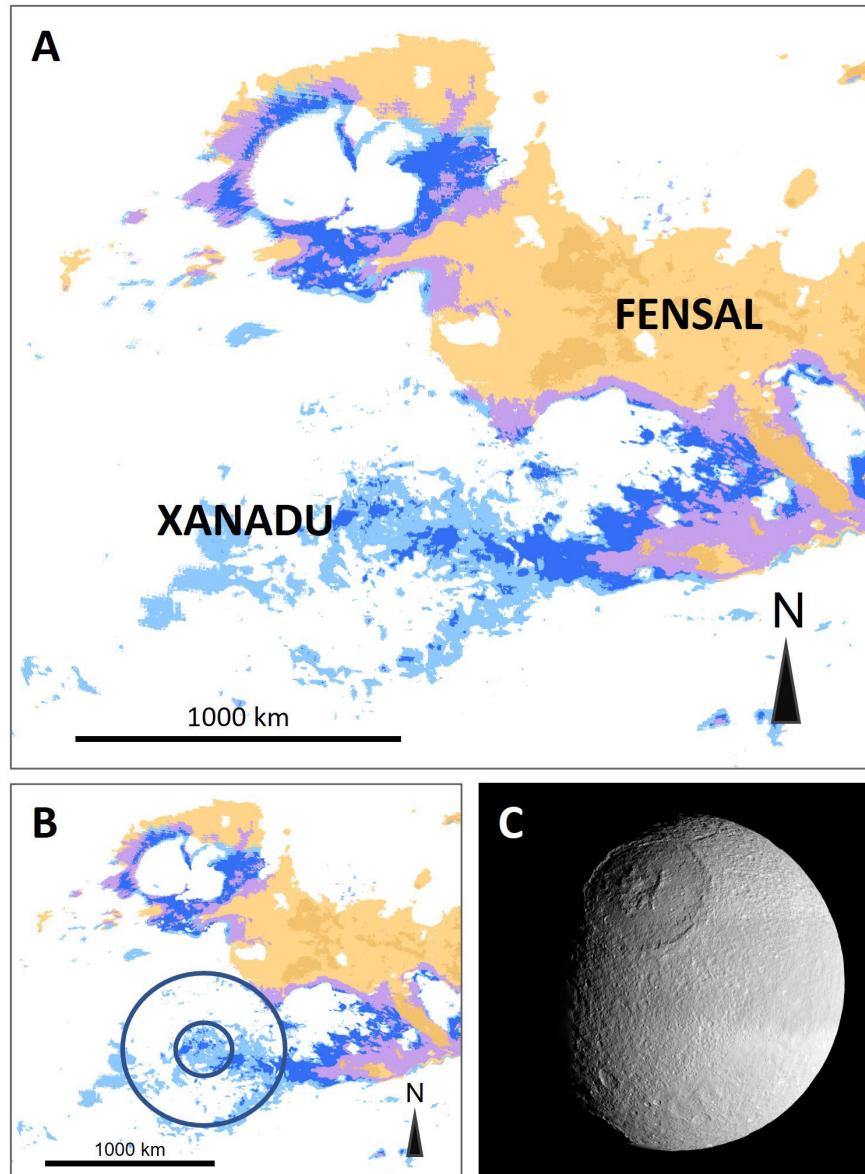


Figure 40. a) A close up of Fig. 11 showing eastern Xanadu. b) Fig. a) with annotated multi-ringed impact basin. c) Tethys with 450 km wide Odysseus Crater occupying the upper left of image. NASA/JPL/Space Science Institute.

A value threshold was applied to VIMS imagery and revealed an approximately 1,500 km. wide circular feature occupying western Xanadu. An annular drainage pattern was also found in VIMS by applying a color inversion to exaggerate the originally VIMS-blue values (Fig. 41).

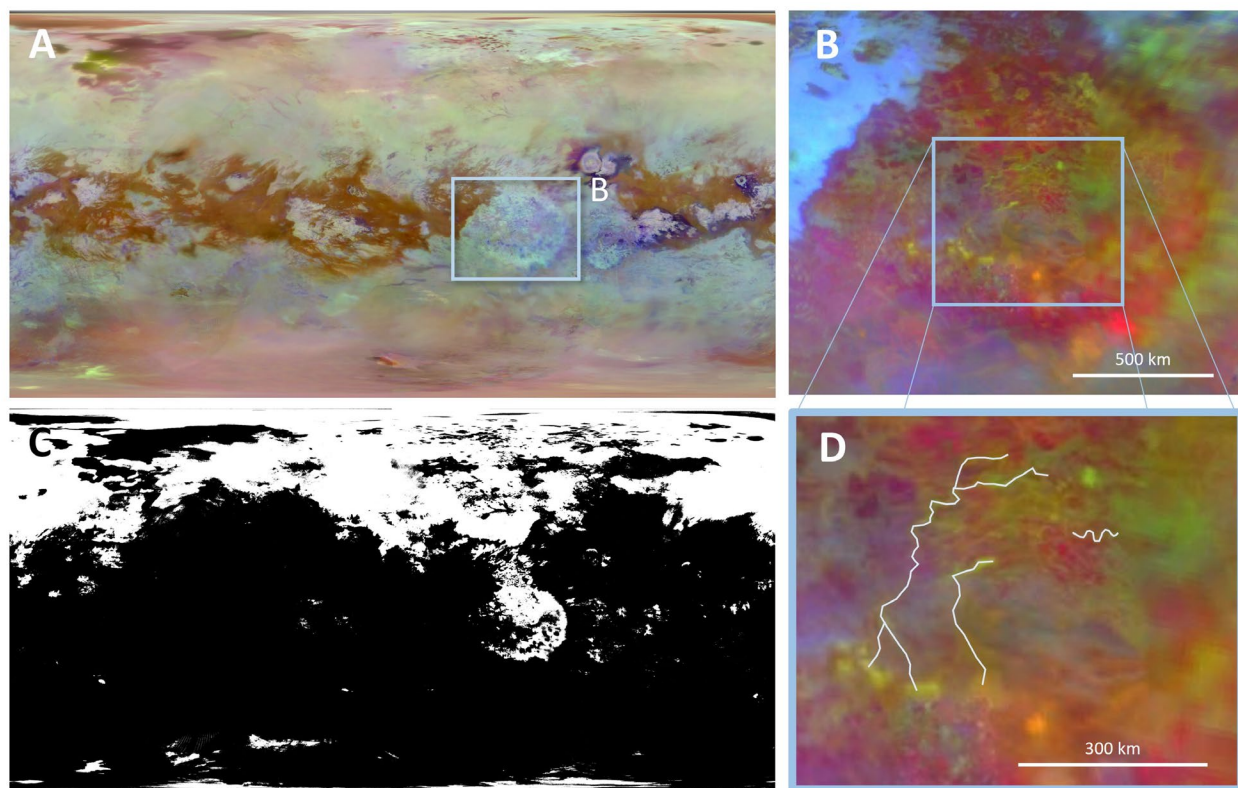


Figure 41. a) Original VIMS imagery. Box outlines location of b), western Xanadu in VIMS with value inversion applied in GIMP to exaggerate fluvial channels obscured in SAR. c) VIMS imagery with a value threshold of 181 – 255 applied in GIMP, revealing a large circular feature within western Xanadu. d) A cropped image of b) with interpreted fluvial channels.

These new observations support the interpretations of Brown et al. (2011) and Soderblom et al. (2009), and we conclude that two large weathered impact craters occupy much of Xanadu.

9.3 A Proposed Geologic History of Titan

We propose the following geologic history: An early ocean of water mixed with tholins from the atmosphere and froze. VIMS-bright tholins subsequently accumulated on the surface by airfall and lithified. Large impacts excavated and deposited crustal material containing water ice and tholins as ejecta across much of the surface as suggested by Crosta et al. (2021). Later cryovolcanism may have also deposited VIMS-blue layers, similar to the hypothesized model by Soderblom et al. (2007). VIMS-bright tholins continued to be deposited, creating observed

alternating layers of VIMS-blue and VIMS-bright within impact craters. Currently, methane precipitates and creates channels. Eroded surface materials are transported to alluvial fans. Wind removes VIMS-brown sand eroded from larger VIMS-blue clasts and deposits it in downwind sand seas.

10. Conclusions

Regions of most abundant sand are generally along the eastern margins of sand seas and within the broad topographic basin of Belet. Mapped ISS-dark regions support previous findings that sand on Titan appears to be obstructed by topographic obstacles and opposing wind currents generated by the large, cold, reflective depression Xanadu. Fluvial obstructions appear to be temporary and localized.

VIMS-blue exposures are present as small isolated patches across Xanadu and much of the upwind margins of sand seas. VIMS-purple surfaces, which we interpreted to be icy organic sand partially covering icy organic gravel and bedrock, were also found within sand seas. A tectonic rift may be responsible for the linear VIMS-blue feature adjacent to Aztlan.

VIMS-blue materials, which are likely a mixture of water ice and tholins, may be the primary source for VIMS-brown sand on Titan. The inferred higher porosity, methane solubility, and low strength of VIMS-bright compared to VIMS-blue materials make the former an unlikely sand source. Spectral signatures also suggest that VIMS-blue and VIMS-brown surfaces are more similar compositionally to each other than VIMS-bright surfaces (Jaumann et al., 2009; Le Mouélic, 2019). Because of their material properties and distribution along western sand sea margins, we suggest that VIMS-brown sand is predominantly sourced from VIMS-blue materials.

Rivers of methane erode layers of VIMS-blue and white materials into sediments and transport them to alluvial fans. Because of the low density of the sediments, the high density of the atmosphere, and low surface gravity on Titan, wind is able to transport much of the sediment from alluvial fans. Across the dry equatorial latitudes, alluvial fans are nearly non-existent because aeolian processes dominate over fluvial, causing alluvial fans to be reorganized into gravelly VIMS-blue surfaces, and sand seas. VIMS-brown sand likely exists in the form of dune fields and sand sheets within *virgae* and *fluctus* at mid-latitudes, but due to the low resolution of VIMS imagery, the small sizes of the dunes, and relatively wide surfaces of VIMS-blue gravels, these sandy features are hidden in VIMS imagery by the dominantly VIMS-blue surfaces. Some sand may also be sourced from VIMS-brown lakebeds and precipitated VIMS-blue sheets from impacts. VIMS-brown sand on Titan may have only migrated ~300 km. Impact craters have revealed multiple alternating layers of VIMS-blue and bright that cover the surface of Titan.

Additional work may be done using spectral analysis on laboratory generated materials similar to those on Titan. Further comparisons could be made between sand sea margins on Titan and Earth. Further evaluations, perhaps computer modeling, should be done on Xanadu to determine if the tectonic features there could be formed from a rebounding of shattered bedrock or upwelling from the heat of the impact. Additional research needs to be done on the Nafud Sand Sea, the underlying paleolakes, the source rock and overlying basalt, and the surfaces between the source rock and the sand seas in order to further test the interpretations made during our research. Currently no work has been done on this region specifically for the purpose of comparing environments with those on Titan.

The surface history of Titan at the equatorial regions is complex, but can be revealed through Earth-analogue studies and analysis of material properties. With the advent of Dragonfly, a distinct understanding of materials and landscapes will clarify this history

REFERENCES

- (2006). Arabian sand seas. In: Arabian Deserts. Springer, Dordrecht. ch. 7, p. 125-166.
- Abdallah, M. and Kumar, A., (2011) An overview of Origin, Morphology and Distribution of Desert Forms, Sabkhas and Playas of the Rub' al Khali Desert of the Southern Arabian Peninsula. *Earth Science India*. vol. 4, p. 105-135.
- Amin, A. and Seif, E.-S. S. A., (2019) Environmental Hazards of Sand Dunes, South Jeddah, Saudi Arabia: An Assessment and Mitigation Geotechnical Study. *Earth Systems and Environment*. 3(5).
- Arnold, K. D., (2014) Sand Sea Extents and Sediment Volumes on Titan from Dune Parameters. *BYU Thesis*. p. 1-56.
- Barnes, J. W., et al., (2008) Spectroscopy, morphometry, and photoclinometry of Titan's dunefields from Cassini/VIMS. *Icarus*. v. 195, p. 400-414.
- Barnes, J. W., et al., (2011) Organic sedimentary deposits in Titan's dry lakebeds: Probable evaporite. *Icarus*. vol. 216, p. 136-140.
- Barnes, J. W., et al., (2015) Production and global transport of Titan's sand particles. *Planetary Science*. vol. 4, p. 1-19.
- Birch, S.P.D. et al., (2016) Alluvial Fan Morphology, distribution and formation on Titan. *Icarus*. vol. 270, p. 238-247.
- Bird, M. K. et al., (2006) The Vertical Profile of Winds on Titan. *Nature*, v. 438, p. 800-802.
- Breeze, P. S., et al., (2017) Prehistory and palaeoenvironments of the western Nefud Desert, Saudi Arabia. *Archaeological Research in Asia*, v. 10, p. 1-16.
- Bridges, N. T., et al., (2015) Formation of gravel-mantled megaripples on Earth and Mars: Insights from the Argentinean Puna and wind tunnel experiments. *Aeolian Research*, v. 17, p. 49-60.
- Brossier, J, et al., (2018) Geological Evolution of Titan's Equatorial Regions: Possible Nature and Origin of the Dune Material. *The Journal of Geophysical Research: Planets*, v. 123(5), p. 1089-1112.
- Brown, R H., et al., (2011) On Titan's Xanadu Region. *Icarus*, v. 214, p. 556-560.
- Bubenzer O., et al., (2020) Sand Seas and Dune Fields of Egypt. *Geosciences*. v. 10(3):101.

- Buchner, E., and Kenkmann, T., (2008) Upheaval Dome, Utah, USA: Impact origin confirmed *Geology*, v. 36; no. 3; p. 227–230.
- Burr, D. M., et al., (2009), Fluvial Network Analysis on Titan: Evidence for Subsurface Structures and West-to-East Wind Flow, Southwestern Xanadu, *Geophysical Research Letters*, v. 36, p. L22203.
- Carrasco, N., *et al.*, (2009) Chemical characterization of titan’s tholins: Solubility, morphology and molecular structure revisited. *J. Phys. Chem. A*, vol. 113, no. 42, p. 11195–11203.
- Charnay, B., et al., (2015) Methane storms as a driver of Titan’s dune orientation. *Nature Geoscience*. v. 8, p. 362–366.
- Chojnacki, M., et al., (2019) Boundary condition controls on the high-sand-flux regions of Mars. *Geology*. v. 47, pg. 427–430.
- Coll, P., *et al.*, (1999) Experimental laboratory simulation of Titan’s atmosphere: Aerosols and Gas Phase. *Planetary Space Science*, v. 47, no. 10–11, p. 1331–1340.
- Collins, G. C., et al., (2009) Tectonics of the Outer Planet Satellites. *Planetary Tectonics*, Cambridge University Press. ch. 7, p. 1-77.
- Comola, F., et al. (2021 [still in review]) Intermittent saltation drives Mars-like aeolian activity on Titan. *EarthArXiv*.
- Cornet, T., et al., (2015), Dissolution on Titan and on Earth: Toward The Age of Titan’s Karstic Landscapes, *Journal of Geophysical Research: Planets*. v. 120, p. 1044–1074.
- Courrech du Pont, S. et al., (2014) Two modes for dune orientation. *Geology*, v. 42(9), p. 743-746.
- Crosta, A. P., et al., (2021) Modeling the formation of Menrva impact crater on Titan: Implications for habitability. *Icarus*, v. 370, p. 114679.
- De Silva, S. L., et al., (2015) Gravel-mantled megariipples of the Argentinean Puna: A model for their origin and growth with implications for Mars. *Geological Society of America Bulletin*, v. 125, no. 11-12, p. 1912-1929.
- Elachi, C., et al., (2005). Cassini Radar Views the Surface of Titan. *Science*. v. 308, p. 970–974.
- Garzanti, E., et al., (2013) Provenance and recycling of Arabian desert sand. *Earth-Science Reviews*, v. 120, p. 1–19.
- Griffith, C. A., et al., (2019) A corridor of exposed ice-rich bedrock across Titan’s tropical region. *Nature*, v. 3, p. 642-648.

- Hedgepeth, J. E., et al., (2018) Impact Craters on Titan: Finalizing Titan's Crater Population. The University of Western Ontario Electronic Thesis and Dissertation Repository. 5618.
- Hesse, P., (2019) Sand Seas. In *Aeolian Geomorphology* (edited by Livingstone, I. and Warren, A.) ch. 8. p. 179-208.
- Hofgartner, J. D., et al., (2016) Erosion of Titan's Craters from Cassini RADAR and VIMS Imagery. *LPSC*, 47th, 2591.
- Hörst, S. M., (2017), Titan's Atmosphere and Climate. *Journal of Geophysical Research: Planets*, v. 122, p. 432–482,
- Janssen, M. A., et al. (2016) Titan's surface at 2.18-cm wavelength imaged by the Cassini RADAR radiometer: Results and interpretations through the first ten years of observation. *Icarus*. p. 443-459.
- Jaumann, R., et al., (2008) Fluvial erosion and post-erosional processes on Titan. *Icarus*, vol. 197, p. 526–538.
- Jaumann, R., et al., (2009) Erosion and Stratigraphic Relations on Titan. *LPSC*, p. 1599.
- Keller, H. U., et al., (2008) The properties of Titan's surface at the Huygens landing site from DISR observations. *Planetary and Space Science*. v. 56, p. 728–752.
- Kenkmann, T., et al., (2005) Structure and formation of a central uplift: A case study at the Upheaval Dome impact crater, Utah, *Geological Society of America*, Special Paper 384, p. 85–115.
- Lancaster, N., (1985) Winds and Sand Movements in The Namib Sand Sea. *Earth Surface Processes and Landforms*. v. 10, p. 607-619.
- Lancaster, N., (1995) Geomorphology of Desert Dunes. *Routledge*. p. 209-216.
- Lapôtre, M. G. A., et al., (2022). The Role of Seasonal Sediment Transport and Sintering in Shaping Titan's Landscapes: A Hypothesis. *Geophysical Research Letters*, v. 49, p. e2021GL097605.
- Larson, E. J. L., (2019) Topographic Effects on Titan's Dune-Forming Winds. *Atmosphere*, v. 10, p. 600.
- Le Gall, A., et al., (2010) Radar-bright channels on Titan. *Icarus*, v. 207, p. 948-958.
- Le Mouélic, S., et al., (2006) Investigation of the Sinlap Crater on Titan Using VIMS and RADAR Data. *Journal of Geophysical Research*, v. 113, E04003.

- Le Mouélic, S., et al., (2019) The Cassini VIMS archive of Titan: From browse products to global infrared color maps. *Icarus*, v. 319, p. 121-132.
- Liang, A., et al., (2020) Provenance and transport process for interdune sands in the Kumtagh Sand Sea, Northwest China, *Geomorphology*. v. 367, p. 107310.
- Lopes, R. M. C., et al., (2010) Distribution and interplay of geologic processes on Titan from Cassini radar data. *Icarus*, v. 205, p. 540-558.
- Lopes, R. M. C., et al., (2013) Cryovolcanism on Titan: New Results From Cassini RADAR and VIMS. *Journal of Geophysical Research*, v. 118, p. 416-435.
- Lopes, R. M. C., et al., (2016) Nature, distribution, and origin of Titan's Undifferentiated Plains. *Icarus*. v. 270, p. 162–182.
- Lopes, R.M.C., et al., (2019) Titan as Revealed by the Cassini Radar. *Space Science Review*. v. 215, art. 33.
- Lopes, R. M. C., et al., (2020) A global geomorphologic map of Saturn's moon Titan. *Nature Astronomy*. v. 4, p. 228–233.
- Lora, J. M., et al., (2014) Simulations of Titan's Paleoclimate. *Icarus*. v. 243, p. 264– 273.
- Lorenz, R., (2006) The Sand Seas of Titan: Cassini RADAR Observations of Longitudinal Dunes. *Science*. vol. 312, p. 724-727.
- Lorenz, R. and Radebaugh, J., (2009) Global Pattern of Titan's Dunes: Radar Survey From The Cassini Prime Mission. *Geophysical Research Letters*, v. 63, p. L03202.
- Lorenz, R. D, et al., (2012) Dunes on planet Tatooine: Observation of barchan migration at the Star Wars film set in Tunisia. *Geomorphology*, v. 201, p. 264–271.
- Lorenz, R. D., et al., (2013) A global topographic map of Titan. *Icarus*. p. 367-377.
- Lorenz, R. D., (2014) Physics of saltation and sand transport on Titan: A brief review. *Icarus*, v. 230, p. 162–167.
- Lorenz, R. D., et al. (2021) An engineering model of Titan surface winds for Dragonfly landed operations. *Advances in Space Research*, v. 67, p. 2219-2230.
- Lucas, A., et al., (2014) Growth mechanisms and dune orientation on Titan. *Geophysical Research Letters*, v. 41(17), p. 6093–6100.
- Malaska, M. J., et al., (2016) Material transport map of Titan: The fate of dunes. *Icarus*, p. 183-196.

- Malaska, M. J., et al., (2020) Labyrinth terrain on Titan. *Icarus*, vol. 344, p. 113764.
- Manga, M., and Wang, C. Y., (2007) Pressurized oceans and the eruption of liquid water on Europa and Enceladus, *Geophysical Research Letters*, v. 34, p. L07202.
- Martinez, Alex & Byrnes, Alan P.. (2002). Modeling Dielectric-Constant Values of Geologic Materials: An Aid to Ground-Penetrating Radar Data Collection and Interpretation. *Current Research in Earth Sciences*, v. 247(1).
- Matteoni, P. et al., (2020) Geomorphological analysis of the southwestern margin of Xanadu, Titan: Insights on tectonics. *Journal of Geophysical Research: Planets*, v. 125, p. e2020JE006407.
- McCord, T. B., et al., (2006) Composition of Titan's surface from Cassini VIMS. *Planetary and Space Science*, v. 54, p. 1524-1539.
- Mckay, C. P., et al., (1996) Elemental composition, solubility, and optical properties of Titan's organic haze. *Planetary and Space Science*, v. 44, p 741-747.
- Mitchell, J. L. and Lora, J. M., (2016) The Climate of Titan. *Annual Review of Earth and Planetary Sciences*, v. 44, p. 353–80.
- Moore, J. M., Howard, A. D. (2010) Are the basins of Titan's Hotei Regio and Tui Regio sites of former low latitude seas?. *Geophysical Research Letters*, v. 37, p. L22205.
- Muhs D. R., et al., (2017) A complex origin for the Kelso Dunes, Mojave National Preserve, A complex origin for the Kelso Dunes, Mojave National Preserve, California, USA: A case study using a simple geochemical method with global applications. *Geomorphology*, v. 276, p. 222–243.
- Neish, C. D. (2010) Radarclinometry of the sand seas of Africa's Namibia and Saturn's moon Titan, *Icarus*, v. 208, p. 385-394.
- Neish, C. D., et al. (2015), Spectral Properties of Titan's Impact Craters Imply Chemical Weathering of Its Surface, *Geophysical Research Letters*, v. 42, p. 3746–3754.
- Northrup, D. S. (2018) A Geomorphological Study of Yardangs in China, the Altiplano/Puna of Argentina, and Iran as Analogs for Yardangs on Titan. *BYU Thesis*. p. 1-85.
- Paillou, P. et al., (2016) Radar scattering of linear dunes and mega-yardangs: Application to Titan, *Icarus*, v. 270, p. 211-221.
- Parton, A., et al., (2018) Middle-late Quaternary palaeoclimate variability from lake and wetland deposits in the Nefud Desert, Northern Arabia. *Quaternary Science Reviews*, v. 202, p. 78-97.

- Porco, C. C., et al., (2005) Imaging of Titan from the Cassini spacecraft. *Nature*. v. 434, p. 159–168.
- Radebaugh, J., et al., (2007) Mountains on Titan observed by Cassini Radar. *Icarus*, v. 192, p. 77-91.
- Radebaugh, J., et al., (2010) Linear dunes on Titan and earth: Initial remote sensing comparisons. *Geomorphology*. p. 122-132.
- Radebaugh, J., et al., (2011) Regional geomorphology and history of Titan's Xanadu province. *Icarus*. vol. 211, p. 672-685.
- Radebaugh, J., (2013) Dunes on Saturn's moon Titan as revealed by the Cassini Mission. *Aeolian Research*. vol. 11, p. 23-41.
- Rodriguez, S., et al., (2014) Global mapping and characterization of Titan's dune fields with Cassini: Correlation between RADAR and VIMS observations. *Icarus*, p. 168-179.
- Rosenberg, T. M., et al., (2013) Middle and Late Pleistocene humid periods recorded in palaeolake deposits of the Nafud desert, Saudi Arabia. *Quaternary Science Reviews*, v. 70, p. 109-123.
- Rudolph, M. L., et al., (2022) Cooling Crusts Create Concomitant Cryovolcanic Cracks, *Geophysical Research Letters*. v. 49, p. e2021GL094421.
- Ruggieri, A., (2018) Volcanism and Cryovolcanism in the Solar System: from Mercury to Charon. *University of Padova Thesis*, p. 1-68.
- Soderblom, L. A., et al., (2007) Correlations between Cassini VIMS spectra and RADAR SAR images: Implications for Titan's surface composition and the character of the Huygens Probe Landing Site. *Planetary and Space Science*, v. 55, p. 2025–2036
- Soderblom, L. A., et al., (2009) The geology of Hotei Regio, Titan: Correlation of Cassini VIMS and RADAR. *Icarus*, v. 204, p. 610–618.
- Solomonidou, A. et al., (2014) Surface albedo spectral properties of geologically interesting areas on Titan *Journal of Geophysical Research: Planets*. vol. 119, pg. 1729-1747.
- Solomonidou, A. et al., (2018) The Spectral Nature of Titan's Major Geomorphological Units: Constraints on Surface Composition. *Journal of Geophysical Research: Planets*, v. 123, p. 489–507.
- Steinbrügge, G., et al., (2020) Brine Migration and Impact-Induced Cryovolcanism on Europa. *Geophysical Research Letters*, v. 47, p. 21.

- Tamrakar, N. K., and Shrestha, M. B., (2008) Relationship Between Fluvial Clastic Sediment and Source Rock Abundance in Rapti River Basin of Central Nepal Himalayas. *Boletín de Geología*, vol. 30, N° 1.
- Tobie, G. et al., (2006) Episodic Outgassing As The Origin of Atmospheric Methane on Titan. *Nature* v. 440, p. 61–64.
- Tokano, T., (2008) Dune-forming winds on Titan and the influence of topography. *Icarus*, v. 194, p. 243–262.
- Turtle, E. P., et al., (2020) Dragonfly: In Situ Exploration of Titan’s Organic Chemistry and Habitability. *LPSC*.
- Weissman, G.S., et al., (2010) Fluvial Form in Modern Continental Sedimentary Basins: Distributive Fluvial Systems. *Geology*. v. 38, p. 39–42.
- Wilson, I. G., (1971) Desert sandflow basins and a model for the development of ergs. *Geographical Journal*. vol. 137, pg. 180-199.
- Yu, X. et al., (2018) Where Does Titan Sand Come From: Insight From Mechanical Properties of Titan Sand Candidates. *Journal of Geophysical Research: Planets*, v. 123, p. 2310–2321.

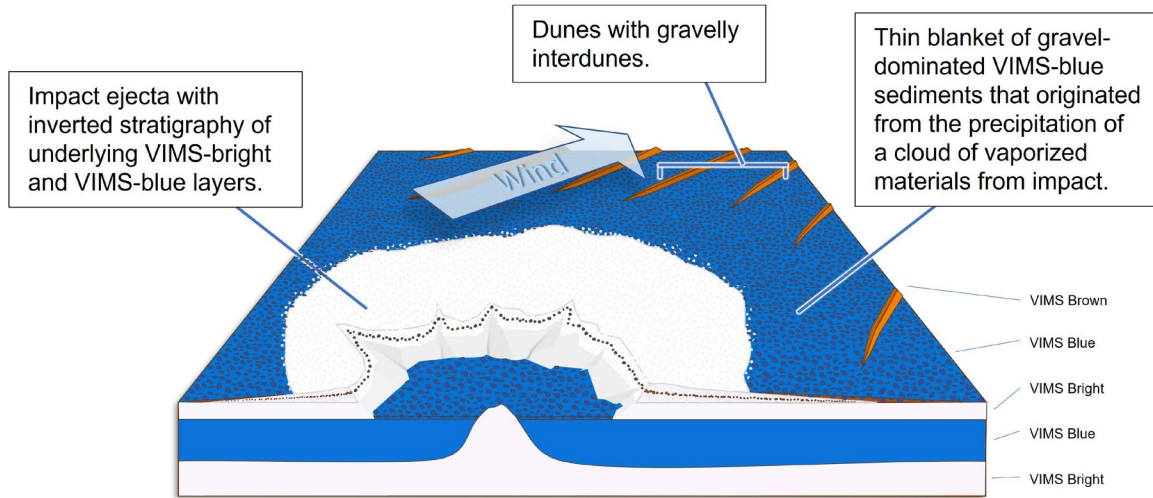
APPENDIX

Based on our conclusions in Sections 7.3 and 8, we interpret thin blankets of condensed VIMS-blue materials from impacts to be a sand source.

Impact craters large enough to excavate underlying VIMS-blue materials appear to produce some VIMS-brown sand, or sediment that after being further processed become VIMS-brown sand, as suggested by the NW boundaries of Fensal reflecting the distribution of VIMS-blue ejecta SE of Menrva (Fig. 11). Some sand also appears to be sourced from eastern VIMS-blue ejecta of Sinlap.

Using Sinlap as a model, we created the block diagrams in Fig. 42.

A



B

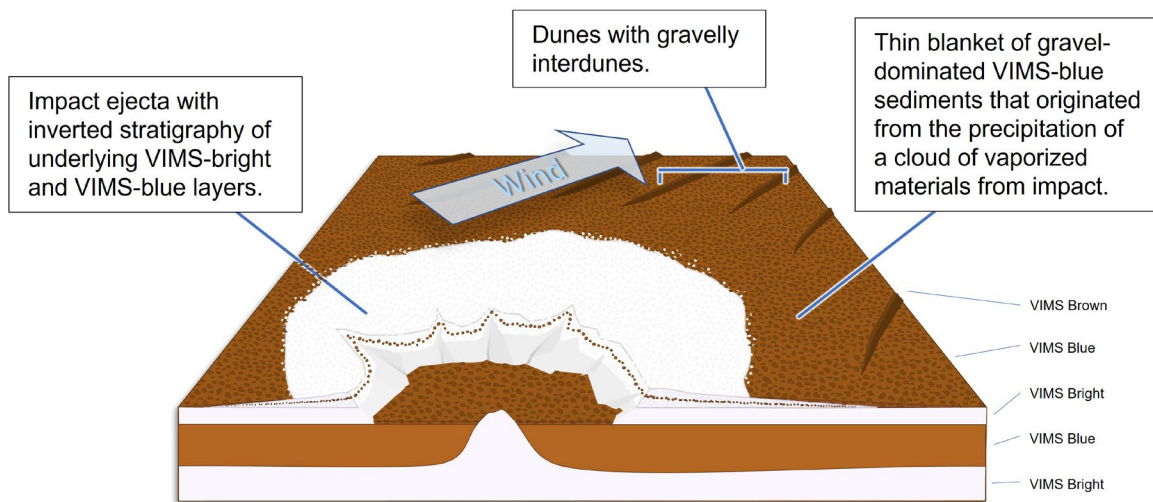


Figure 42. Sand production from VIMS-blue impact crater ejecta. a) VIMS color scheme and b) color scheme based on Huygens descent imagery b). Diagrams are based on observations of Sinlap crater in VIMS, ISS and SAR imagery, and a topographic profile. We suggest that large impactors struck the surface of Titan after some VIMS-bright had been deposited, created interpreted impact basins within Xanadu (see Section 8.2), and spread VIMS-blue materials across much of the surface. More VIMS-bright then was deposited and created alternating layers of VIMS-bright and blue at depth. See Section 8 for more on interpreted stratigraphy.